EFFECTS OF NONSPHERICAL TETRAALKYLAMMONIUM CATIONS ON THE STRUCTURE AND MAGNETIC PROPERTIES OF NON-PRUSSIAN BLUE STRUCTURED MANGANESE(II) PRUSSIAN BLUE ANALOGUES

by

Casey Gene Hawkins

A thesis submitted to the faculty of
The University of Utah
in partial fulfillment of the requirements for the degree of

Master of Science

Department of Chemistry

University of Utah

May 2013

The University of Utah Graduate School

STATEMENT OF THESIS APPROVAL

The thesis of Casey Gene Hawkins
has been approved by the following supervisory committee members:

Joel S. Miller	, Chair	30 Jan 2013 Date Approved
Thomas G. Richmond	, Member	30 Jan 2013 Date Approved
Michael D. Morse	, Member	30 Jan 2013 Date Approved

and by Henry S. White , Chair of

the Department of Chemistry

and by Donna M. White, Interim Dean of The Graduate School.

ABSTRACT

Prussian blue (PB) and its analogues (PBAs) hold a unique place in the world of molecule-based magnets (MBM) as they have been the most studied and are the best understood. Even though extensively studied, PB and PBAs continue to offer new and interesting insights into the world of MBM and the phenomenon called magnetism. The work described here provides the first steps in looking at the effects that nonspherical cations can have on the structure and magnetic properties of PBAs. The magnetic properties of several novel PBAs are presented. In this work, the products formed by reacting a non-spherical tetraalkylammonium cation, e.g., $[NMe_3Et]^+$, $[NMe_2Et_2]^+$, and $[NMeEt_3]^+$, with $Mn^{II}(OAc)_2$ acetate are presented. Seven pure compounds have been isolated at the time of this writing.

The reaction of $[NMe_3Et]CN$ with $Mn^{II}(OAc)_2$ in water yielded a lime-green compound of $[NMe_3Et]_3Mn_5(CN)_{13}$ composition that is a three-dimensional PBA incorporating a pentacyanomaganate ion. Reaction of $[NMe_3Et]CN$ with $Mn^{II}(OAc)_2$ in methanol yielded the product of nominal $[NMe_3Et]_5Mn_9(CN)_{23}$ composition which exhibits an unprecedented gold color. A second reaction in methanol yielded a product with a molecular formula of nominal $[NMe_3Et]_2Mn_3(CN)_8$ composition. This compound exhibits a spin-frustrated or spin-glass behavior.

The reaction of $[NMe_2Et_2]CN$ with $Mn^{II}(OAc)_2$ in water yielded a material of $[NMe_2Et_2]_3Mn_8(CN)_{19}$ composition. Running the reaction in methanol yielded $[NMe_2Et_2]Mn_3(CN)_7$. Analysis of the magnetic data indicates that this compound has all three Mn^{II} sites in the high-spin configuration.

The reaction of $[NMeEt_3]CN$ with $Mn^{II}(OAc)_2$ in methanol yields another all high-spin compound with $[NMeEt_3]_2Mn_2(CN)_6$ composition. This reaction, when carried out in an aqueous solution, yielded the product $[NMeEt_3]_3Mn_8(CN)_{19}$.

This dissertation is dedicated to my wife, Jennifer Hawkins, and my daughter, Emma Hawkins. Their patience is endless.

TABLE OF CONTENTS

LIST OF TABLES

LIST OF SCHEMES

LIST OF FIGURES

LIST OF SYMBOLS AND ABBREVIATIONS

E_T	thermal energy
E_H	magnetic coupling energy
T	temperature
T_c	critical ordering temperature
T_C	Curie temperature
T_N	Néel temperature
M	magnetization
H	applied magnetic field
χ	molar magnetic susceptibility
C	Curie constant
N_A	Avogadro's number
g	Landé factor
S	spin
k_B	Boltzmann's constant
θ	Weiss constant
μ_{eff}	effective moment
μ_B	Bohr magneton
J	exchange coupling
M_s	saturation magnetization
H_{cr}	coercive field
M_{rem}	remnant magnetization
Oe	Oersted

M_{ZFC}	zero field cooled magnetization
M_{FC}	field cooled magnetization
T_b	bifurcation temperature
ac	alternating current
dc	direct current
χ'	in-phase ac susceptibility
χ''	out-of-phase ac susceptibility
ω	frequency
ϕ	Spin glass figure of merit
Hz	Hertz
MBM	molecule-based magnet
TCNE	tetracyanoethylene
PB	Prussian blue
fcc	faced-centered cubic
PBA	Prussian blue analogue
Solv	solvent
ls	low-spin
hs	high-spin
FO	ferromagnetic coupling
AF	antiferromagnetic coupling
CN^-	cyanide ion
NEt_4^+	tetraethylammonium cation
OAc^-	acetate anion
MeOH	methanol
Et_2O	diethyl ether
IR	infrared
ν	infrared absorption

TGA	thermogravimetric analyses
MS	mass spectroscopy
MPMS	magnetic properties measurement system
SQUID	superconducting quantum interference device
PPMS	physical properties measurement system
s	strong intensity (infrared spectroscopy)
m	medium intensity (infrared spectroscopy)
w	weak intensity (infrared spectroscopy)
TIP	temperature independent paramagnetism
XRD	X-ray diffraction
PXRD	powder X-ray diffraction

ACKNOWLEDGMENTS

In the course of becoming educated, there are those few, rare individuals who have had an impact in such a way that the affected individual will never view the world in the same way. I have had the great privilege to have several of these people in my life. At a young age, my parents, Marvin and Jamie Hawkins, opened the world of science and nature to me by raising me on a farm. It was the encouragement and support of these two pillars in my life that has allowed me to be where I am today.

I must acknowledge the influence of Patricia Moore. While she may never fully understand the influence she has had in my life, it was this wonderful lady that pushed me beyond the comforts of my own perceived boundaries. Without the loving guidance of one who has been there, I never would have been willing to challenge the unknown and fight to wrestle it into submission.

I am indebted to the wonderful individuals that are a part of the Air Force Academy's chemistry department. While I have been influenced by many individuals, the following are only a few: Dr. Donald Bird taught me that there is more to learning than grades, Dr. Ronald Furstenau taught me the value of leisure learning and the value of books, Dr. Kimberly Gardner instilled in me the love of inorganic chemistry, and Dr. Norman Heimer never failed to shed light on

the depth of my ignorance every time I spoke with him. It was my association with these wonderful individuals that has allowed me to obtain this degree.

I must thank Dr. Joel Miller for allowing me to join his renowned research group. I am grateful for the opportunity to learn from his vast stores of knowledge. The short time I have had in Dr. Joel Miller's research group has given me a greater understanding of the world of chemistry and research.

I would be remiss if I did not thank my beautiful wife, Jenni Hawkins. Without her constant love and encouragement, I would not have been at the University of Utah nor would I have achieved the level of academic success that I currently enjoy. I will forever be indebted to this wonderful woman.

Disclaimer Clause: The views expressed in this article are those of the author and do not reflect the official policy or position of the United States Air Force, Department of Defense, or the U. S.

CHAPTER 1

MAGNETISM, MOLECULE-BASED MAGNETS, AND PRUSSIAN BLUE ANALOGUES

Introduction to Magnetism

Since the initial discovery of lodestone by the ancients, magnets have come to pervade society, becoming integral to many important areas of scientific research and commercial applications. Magnets have been incorporated into biomedical implants, magnetic resonance imaging (MRI) equipment, speakers and acoustical equipment, telecommunications, motors and generators, magnetic shielding, and information storage.[1] With current advances in magnetic materials, their use in materials such as switches and sensors are being investigated.[2] The unique properties of magnetism, coupled with the central role of magnets in current society, have resulted in many scientific investigations and reviews.[3]

Magnetism is a phenomenon that describes a material's bulk response to an applied magnetic field[4] and originates from the spin that is inherent to the material's electrons. A key aspect of magnetism arises from how the spins on adjacent atoms or molecules interact, or couple, with one another. When electrons are spin-paired, they contribute a diamagnetic response to the overall

magnetic response of the material. This diamagnetic contribution arises from the field-induced electron circulations of paired electrons and generates a weak induced magnetic field that slightly opposes the applied magnetic field.[4] Spin-paired electrons are a part of every molecule and the diamagnetic response must be accounted for when conducting a magnetic analysis on any compound. The presence of an unpaired electron, or spin, on an atom or molecule that does not strongly interact with another spin gives rise to paramagnetism; a system that is attracted into an applied magnetic field. Unpaired spins are located in the valence shell of atoms. Usually, this is the d-orbitals for transition metals and p-orbitals for organics,[3,5] and f-orbitals for rare earth materials.[6] Since an atom or molecule can have a single or multiple spins, it is easier to refer to the total amount of spin on an atom or molecule as the total-spin moment.

When an atom or molecule has a net magnetic moment, there are various ways that the moment can interact with the moments on atoms and/or molecules in close proximity. The pair-wise interaction between two moments is referred to as coupling. There are two coupling motifs: 1) ferromagnetic coupling, where the interacting moments line up parallel and in the same direction, and 2) antiferromagnetic coupling, where the interacting moments line up parallel and in opposite directions. It should be noted that these short-range interactions between two moments are not the same as magnetic ordering. When the short-range interactions extend throughout the bulk material, the phenomenon of magnetic ordering can result. However, when the moments do not interact strongly throughout the bulk material, the moments can lie in random

orientations, resulting in a paramagnet with antiferromagnetic or ferromagnetic coupling.

When short-range interactions lead to long-range coupling, magnetic ordering can occur. Ferromagnets are formed when moments on adjacent atoms are aligned parallel to each other. Antiferromagnets result from adjacent moments aligning parallel, but in opposite directions to each other. A special case of an antiferromagnet is a ferrimagnet. In a ferrimagnet, the moments are aligned parallel and in opposite directions, but the moments do not have the same magnitude (Figure 1.1). As a result, there is a net bulk moment in the material. While the coupling is antiferromagnetic, a ferrimagnet more closely resembles a ferromagnet. While these three types of magnetic ordering are the most common, they are only three of more than 20 types of possible magnetic ordering motifs.[3g]

Magnetic materials exhibit ordering over an inherent temperature range; above a certain temperature, magnetic ordering no longer exists and the material displays paramagnetic behavior. The type of magnetism, as well as the temperature at which the material changes from a magnetically ordered compound to a paramagnetic compound, is dictated by the competition of two energies. The competing energies are the thermal energy (E_T) and the magnetic energy (E_H). Paramagnetic behavior is dominant when E_T is greater than E_H. When E_H is greater than E_T, magnetic ordering occurs in the material. The point at which E_H and E_T are equal is called the ordering or critical temperature, T_c.

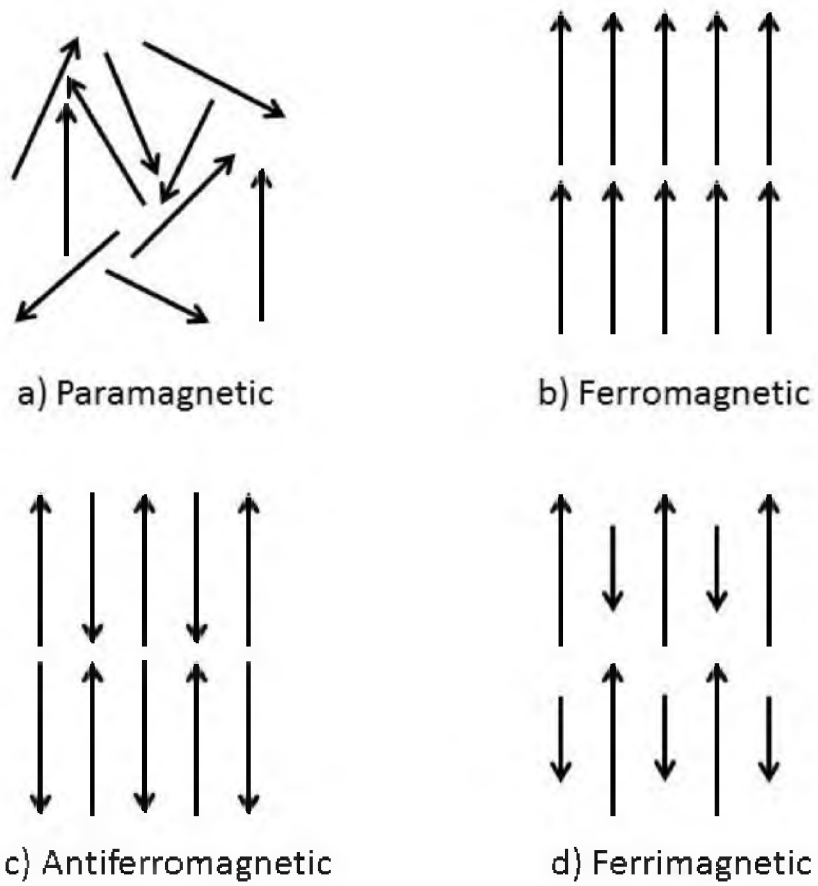

Figure 1.1 2-D illustrations of common magnetic coupling schemes.

The T_c is also referred to as the Curie temperature (Tc) for ferromagnets and the Nèel temperature (T_N) for antiferro- and ferrimagnets.

A material's magnetic behavior is measured by the bulk response to a magnetic field and can be described by the following equation:

$$M = \chi H, \tag{1.1}$$

where M (emu•Oe/mol) is the magnetization, χ (emu/mol) is the susceptibility, and H (Oe) is the applied magnetic field. The observed molar susceptibility, χ_o, is the sum of both the diamagnetic susceptibility (χ_d) and the paramagnetic susceptibility (χ_p).

$$\chi_o = \chi_d + \chi_p. \tag{1.2}$$

The diamagnetic susceptibility is independent of temperature and is inherent to the material. The paramagnetic susceptibility is temperature dependent and increases as temperature decreases. The susceptibility of purely paramagnetic materials can be modeled using the Curie Law:

$$\chi = \frac{C}{T}, \tag{1.3}$$

where C (emu•K/mol) is the Curie constant and T (K) is the absolute temperature. The Curie constant is defined by equation 1.4 where N_A is

Avogadro's number, g is the Landè factor, μ_B is the Bohr magneton, S is the spin quantum number, and k_B is Boltzman's constant.

$$C = \frac{N_A g^2 \mu_B{}^2 S(S+1)}{3k_B} . \quad (1.4)$$

When a material has moments that interact throughout the bulk via ferro- or antiferromagnetic coupling, the material does not behave as a paramagnetic material and the temperature dependence of χ cannot be modeled using the Curie Law (Equation 1.3). With the introduction of the Weiss constant, θ (K), the temperature dependence of χ can be modeled using the following Curie-Weiss equation:

$$\chi = \frac{C}{(T-\theta)} . \quad (1.5)$$

The Weiss constant is determined experimentally by plotting the inverse of χ as a function of temperature, T, and extrapolating the most linear portion back to the intercept of the x-axis. The Weiss constant represents short-range interactions. When there is no short-range interaction between moments, as is the case for a paramagnnet, the linear extrapolation will pass through the origin and θ = 0. If short-range ferromagnetic coupling exists, the Weiss constant will be a positive value. Likewise, if short-range antiferromagnetic coupling exists, the Weiss constant will have a negative value. The magnitude of the deviation away from the origin is an indicator of the strength of coupling experienced by the coupling moments. Each system, para-, ferro-, and antiferromagnetic, has unique plots

when the inverse of χ is plotted as a function of T (Figure 1.2a). The shape of the plot is a useful tool in determining the type of magnetic system that exists within a material.

Another useful discriminator for the type of system in a material is the χT(T) plot (Figure 1.2b). When a material is in a temperature region well above T_c and the moments do not experience any coupling, the spin-only value, χT, of the material can be theoretically calculated using the following equation:

$$\chi \mathrm{T} = \frac{g^2 S(S+1)}{8} \tag{1.6}$$

Historically, the effective moment, μ_{eff}, was used to describe the magnetic interactions in a material. The μ_{eff}, reported in Bohr magnetrons (μ_b), is closely related to χT and is represented by the following equation:

$$\mu_{eff} = \sqrt{8\chi T} = g\sqrt{S(S+1)} \tag{1.7}$$

There are several different methods to determine the T_c of a material (Figure 1.3). These methods measure the response of a material in an applied field as a function of temperature. One method is to measure the magnetic response of a material in a small applied field and then vary the temperature. Usually, a sample is cooled to a low temperature under zero or near-zero applied field (ZFC measurement). A small field is then applied and the temperature is raised. The sample is then cooled under the small applied field

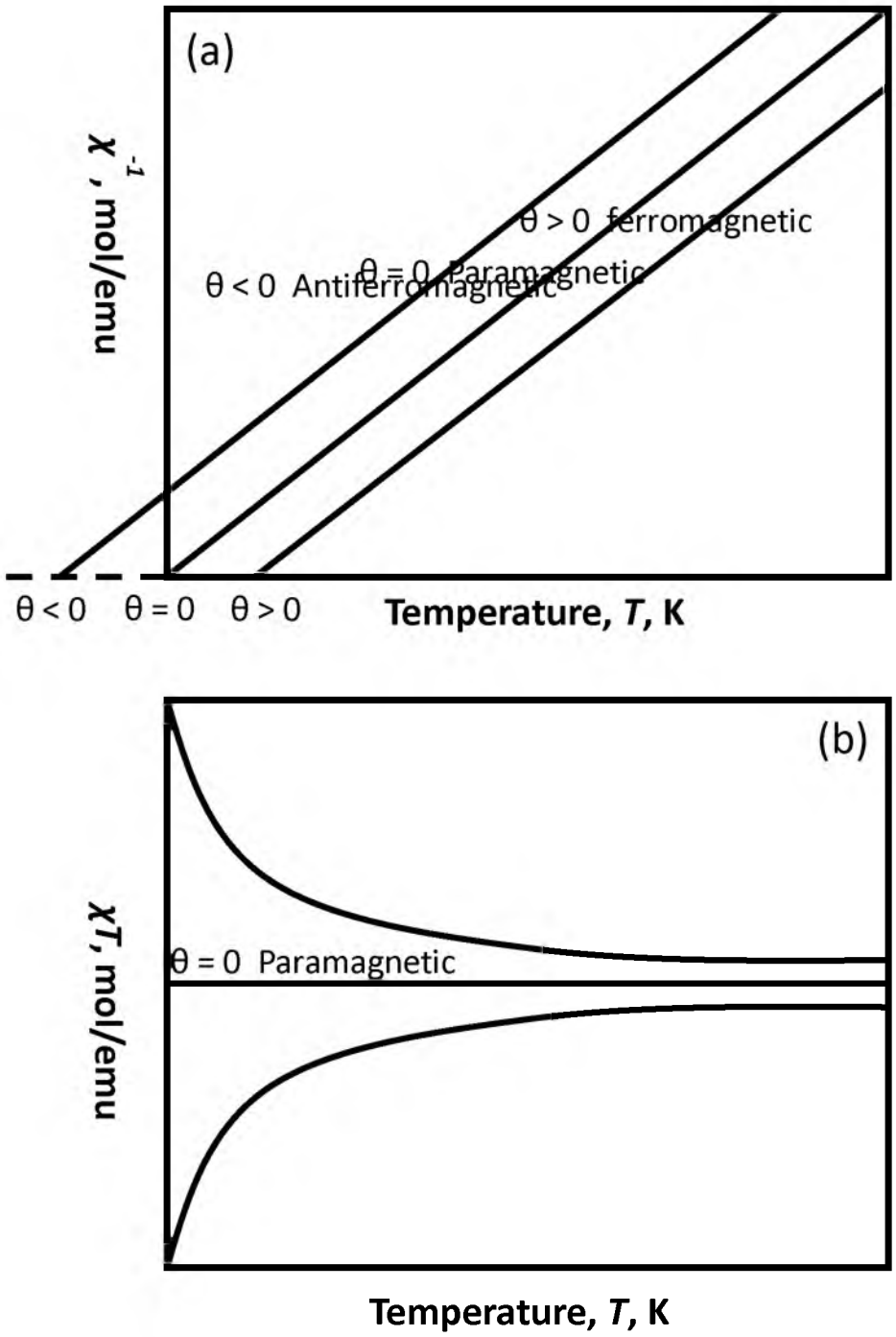

Figure 1.2 General plots of χ^{-1}(a) and χT (b) for a paramagnetic system as well as ferromagnetic and antiferromagnetic coupling.

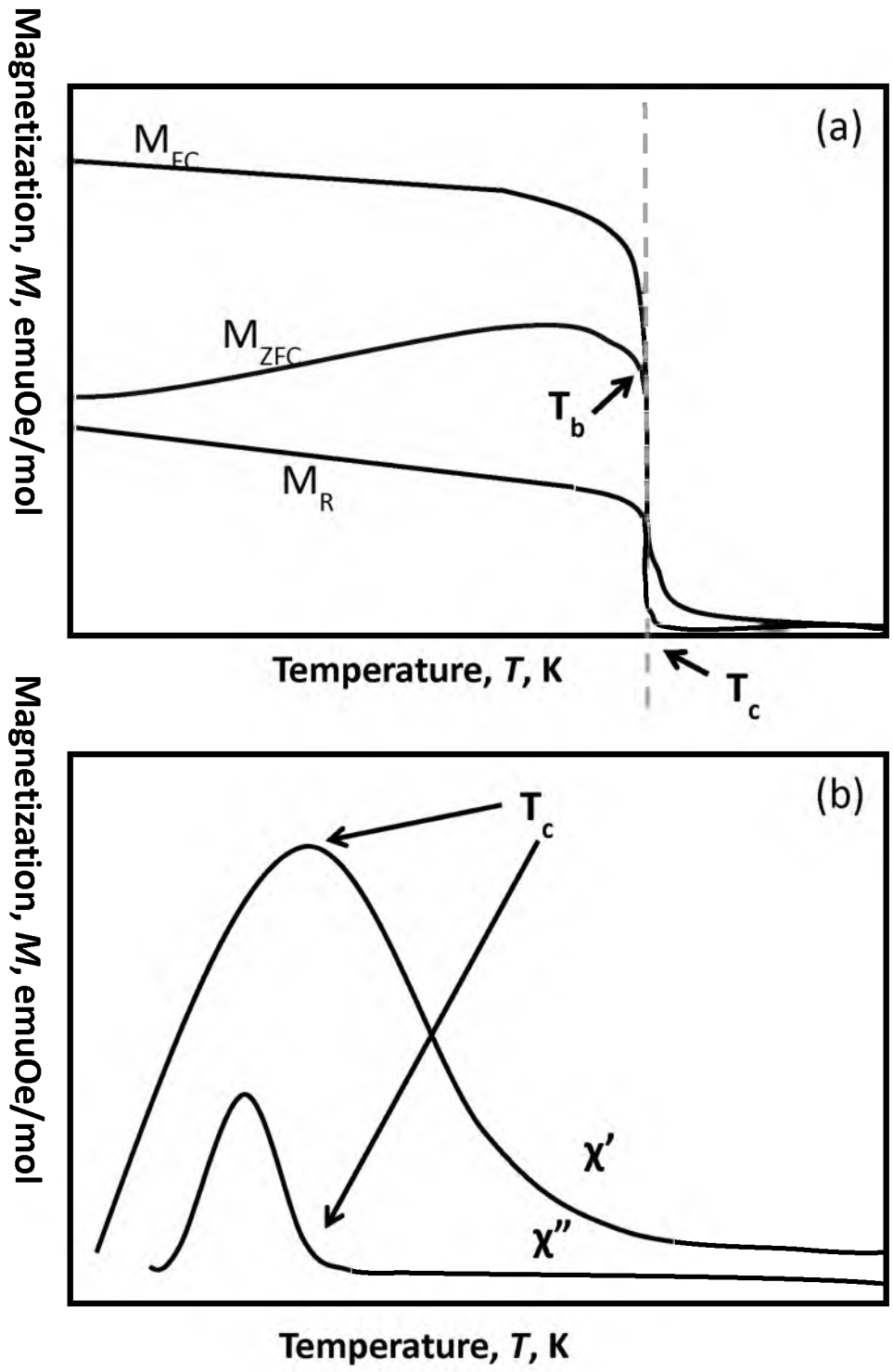

Figure 1.3 Bifurcation temperature, T_b, and critical temperature, T_c, using generic plots for field cooled (FC), zero-field cooled (ZFC), and remnant magnetization (a) and critical temperature for generic ac susceptibility plots (b).

(FC measurement) and again warmed under the small applied field. The T_c can obtained by taking the steepest slope and extrapolating it to the temperature when M = 0. Above the T_c, the ZFC and FC measurements usually have the same value. As the temperature decreases, the two measurements will diverge. This divergence temperature is referred to as the bifurcation temperature, T_b, and is sometimes reported as the T_c. A similar measurement consists of cooling the sample in a small applied field and then warming the sample under no applied field in order to measure the remnant magnetization, $M_r(T)$. The steepest data are indicative of the material going from an ordered system to a disorded system. By extrapolating the most linear portion of the steepest data points for the $M_r(T)$ to the x-axis, the T_c can be determined.

Another method of determining a material's T_c is to measure the material's susceptibility in an alternating current (ac) environment as a function of frequency. The ac measurement involves measuring the susceptibility with a zero applied field in an alternating electric field with variable frequencies. At temperatures above the T_c, the moments do not interact strongly with adjacent moments. This allows for the moments to rapidly change with the alternating electric field. As the temperature approaches the T_c, the moments begin to interact and do not follow the ac field as freely. As the interaction grows, the moments do not completely cancel out, resulting in a response in the ac susceptibility. The ac susceptibility is composed of the in-phase, $\chi'(T)$, and the out-of-phase, $\chi''(T)$, components. The maximum in the $\chi'(T)$ and the onset in the

χ"(T) can be used to determine the material's T_c (Figure 1.3). Ideally, the same value for T_c would be obtained by all of the measurement techniques. However, it is often the case that the different methods result in a T_c that varies by a few degrees.

Molecule-Based Magnetic Materials

Due to the great interest in magnetism and magnetic materials, an increased focus on the synthesis and properties of molecule-based magnets has occurred. Atom-based magnets (ABMs) have been known for perhaps the last 5000 years with the use of magnetite, an iron oxide (Fe_3O_4).[7] In time, other permanent magnets began to be synthesized. Some notable magnets are the CrO_2 magnet, first synthesized in the mid-1950s, and the $SmCo_5$-doped magnet, first synthesized in the early 1970s. Also, in the mid-1980s, another rare-earth-doped magnet, the $Nd_2Fe_{14}B$ magnet, was first synthesized. The synthesis of these magnets is energy intensive and requires high heat and pressure to shape and mold the magnets.[8] While the magnetic density is high in these magnets, the synthesis process prevents almost any fine-tuning of properties. Molecule-based magnets offer an alternative.

An alternative to ABMs are molecular-based magnets, MBMs. MBMs are magnetic materials constructed using discrete molecular building blocks. Through this approach, magnetic materials composed of zero dimensional (0D), 1D, 2D, and 3D arrays have been synthesized. This type of distinction does not exist for conventional ABMs.[9] Some notable examples of MBMs are the first 0D

ionic electron transfer salts, $[Fe(C_5Me_5)_2]^+[TCNE]^{\bullet-}$ (TCNE = tetracyanoethylene), a ferromagnet that has a T_c of 4.8 K,[10] and the first MBM that ordered at or above room temperature was $V[TCNE]_x$ ($x \approx 2$) with a T_c of 400 K.[11] The use of a discrete building block approach allows the scientist to have considerable control over the synthesis and connectivity of a magnetic material. Through this control, the scientist is able, at least in principle, to fine-tune a material's magnetic properties to achieve a desired purpose. Another attractive feature of this approach is that a MBM can typically be synthesized by relatively low-temperature solution-based methodologies.

While MBMs are an attractive alternative to conventional ABMs, they do not come without their own inherent problems. Due to the presence of organic linkers that may not carry a moment, the spin-density within a MBM is lower than ABMs. This results in a low magnetic density that precludes MBMs from being permanent magnets. Another problem is that most MBMs decompose when exposed to oxygen. In order for MBMs to effectively be incorporated in current and future technology, these are just some of the problems that must be overcome by further research and development.

Prussian Blue Analogues

Prussian blue (PB), a compound that is often given the title of the first synthetic coordination compound, was a pigment first prepared in 1704 by a Berlin draper by the name of Diesbach.[12] The study of PB has had a crucial role in the development of MBMs and the understanding of the magnetic interactions associated with MBMs. PB, with a molecular formula of

$Fe^{III}[Fe^{II}(CN)_6]_{3/4}•7/2H_2O$, is part of a class of MBMs that have the general formula of $C_xM[M'(CN)_6]_y•Z$solvent where C is a cation, often an alkali metal, while M and M' are metal ions.[13]

In 1936, the first steps in solving the structure of PB were taken by Keggin and Miles when they made a structure determination using powder diffraction data.[13a] In 1973, the proposed structure was improved when single crystal analysis was conducted by Ludi and coworkers.[13b, 14] It was determined that when y = 1 in $C_xM[M'(CN)_6]_y•Z$solvent, the material adopts a face-centered cubic (*fcc*) structure (Figure 1.4). The interstitial sites can contain cations for charge balance or solvent. Two different octahedral metal sites exist in this structure: 1) strong ligand-field sites (M'-C_6 coordination environment) and 2) weak ligand-field sites (M-N_6 coordination environment). When y < 1, the M' ions are not fully coordinated by carbon atoms and it is possible for solvent to coordinate at the open sites. It is possible to improve the crystallinity of a Prussian Blue Analogue (PBA) by the inclusion of cations. The improved crystallinity leads to stronger coupling pathways and results in stronger magnetic properties. These properties are of interest to scientists who study magnetic phenomena. The crystalline framework of PB is related to that of perovskites such as $CaTiO_3$. The difference is that the metal centers are bridged by cyano groups in PB and by oxygen in perovskites.

Synthesis of PB and PBAs is performed by mixing two filtered solutions of a metal source and a cyano source, resulting in the formation of an insoluble precipitate. For most PB and PBAs, the one solution contains

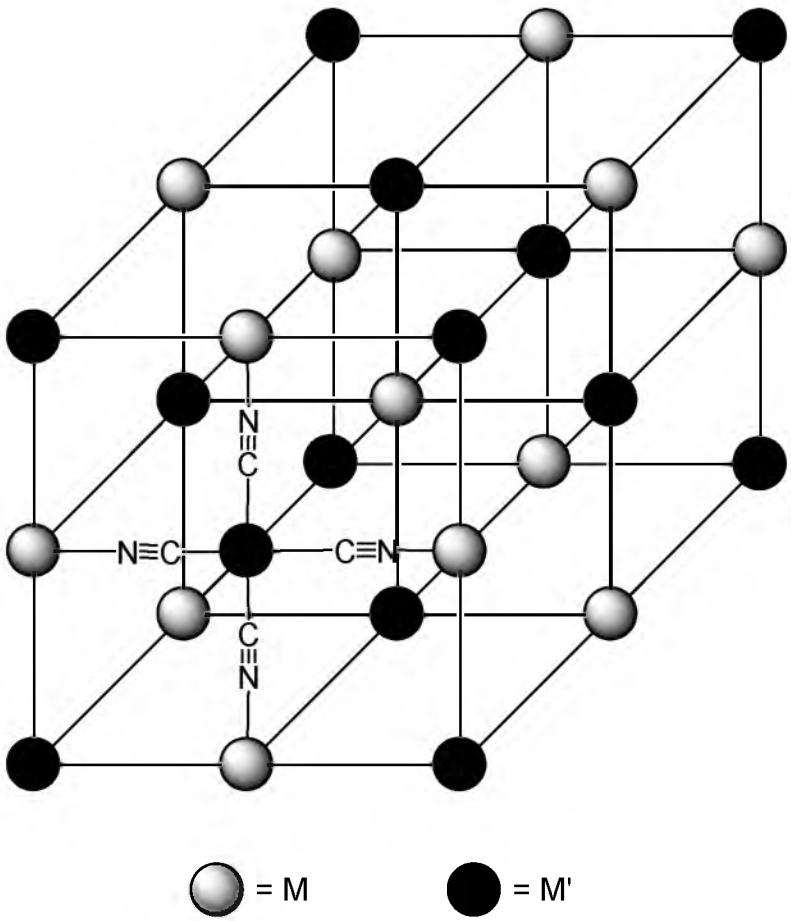

Figure 1.4 Ideal face-centered cubic (*fcc*) structure for Prussian blue and its analogues, where two distinct metal sites (M and M') are connected by a cyanide ligand.

hexacyanometalates and the other contains solvated metal cations. However, it has been shown that mixing a solution of Mn(II) salt and a solution of X(CN) salt, where X = Na^+, K^+, Rb^+, Cs^+, $[Me_4N]^+$, or $[Et_4N]^+$, can result in an insoluble precipitate that has PB or PBA structure. Despite the mild conditions and the apparently straightforward synthesis of PBAs, numerous complications can occur: 1) the product may contain a variety of species in the interstitial sites, 2) the PBA may be amorphous, poorly crystalline, or contain multiple phases, 3) the solvent content may vary from sample to sample, 4) the bridging cyanide ligands may undergo linkage isomerization,[15] and 5) intermetallic electron transfer due to redox activity may occur. These problems have led to difficulty in characterizing some PBAs. Although these problems exist, the wide variety of building blocks coupled to the ease of synthesis creates the potential for countless PBAs to be synthesized. The synthesis and characterization of a variety of PB and PBA compounds will lead to a greater understanding of the magnetic properties of these species.

Prussian blue was determined to be a ferromagnet with a T_c of 5.6 K.[16] The low ordering temperature occurs because half of the metal centers are diamagnetic low-spin (*ls*) d^6 Fe^{II}, resulting in a long through-bond distance between paramagnetic high-spin (*hs*) d^5 Fe^{III} centers of 10.28 Å (Figure 1.5). This long distance between moments results in a weak exchange coupling. A possible way to increase the ordering temperature would be to exchange the diamagnetic metal center with a paramagnetic metal center. This would result in a through-bond distance between paramagnetic sites of ~5.5 Å (Figure 1.6) and

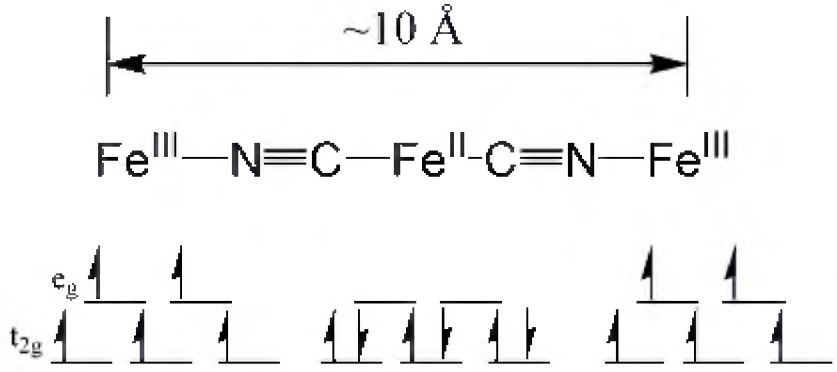

Figure 1.5 Depiction of coupling through diamagnetic *ls*-Fe^{II}. Interactions between the two Fe^{III} ions are weak due to the distance between these centers being more than ~10 Å.

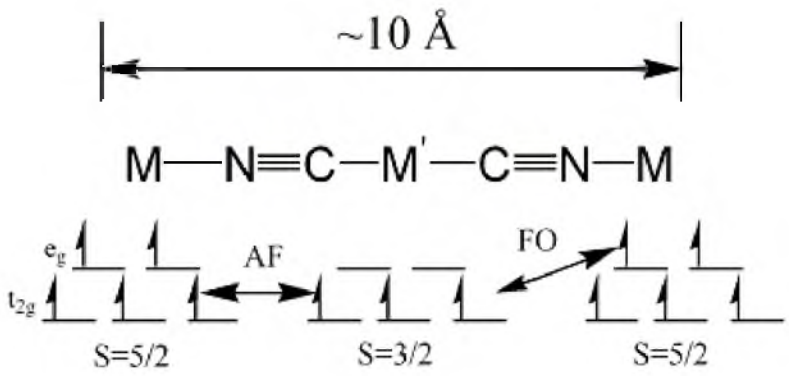

Figure 1.6 Depiction of the incorporation of a paramagnetic metal ion, M', in the structure thus reducing the overall distance between adjacent spin centers from 10 Å to ~5.5 Å. The e_g and t_{2g} orbitals are orthogonal to each other and therefore, ferromagnetic coupling (FO) is observed between these orbitals. Antiferromagnetic coupling (AF) between the nonorthogonal orbitals (t_{2g}-t_{2g}) is also displayed.

an increased T_c due to stronger exchange coupling. Employing this idea, new PBAs have been synthesized with magnetic ordering temperatures well above 5.6 K. Some compounds have only a slight improvement in the T_c, such as $Co^{II}[Cr^{III}(CN)_6]_{2/3}\bullet zH_2O$ (T_c =19 K)[17] and $V^{III}[Mn^{III}(CN)_6]$ (T_c = 28 K).[18] Some compounds, such as $CsMn^{II}[Cr^{III}(CN)_6]$ (T_c = 90 K)[19] and $Cs_2Mn^{II}[V^{II}(CN)_6]$ (T_c = 125 K)[20] have significantly higher magnetic ordering temperatures. Compounds with near or above room temperature magnetic ordering temperatures contain Cr^{III} and V^{II}. Some examples are $Cr^{III}[Cr^{III}(CN)_6]_{0.93}[Cr^{II}(CN)_6]_{0.05}$ (T_c = 260 K)[21], $V^{II}_{0.42}V^{III}_{0.58}[Cr^{III}(CN)_6]_{0.86}\bullet 2.8H_2O$ (T_c = 315 K)[22], and $KV^{II}[Cr^{III}(CN)_6]\bullet 2H_2O\bullet 0.1KO_3SCF_3$ ($T_c \approx$ 373 K).[23]

The PB and PBA compounds consist of cyanide bridges linked at either end to an octahedral metal ion. Coupling across the bridge occurs because of the overlap of the metal d-orbitals with the vacant cyanide π^*-orbitals. For octahedral metal ions, the unpaired electrons (spins) will reside in the t_{2g} and the e_g orbitals. Spins in orthogonal orbits will couple ferromagnetically while spins in nonorthogonal orbits will couple antiferromagnetically (Figure 1.6). Since the unpaired spins only reside in the t_{2g} and the e_g orbitals, only three situations can occur: 1) the spins on M' only reside in the e_g magnetic orbitals, allowing for ferromagnetic interactions to occur with the t_{2g} magnetic orbitals present on $[M(CN)_6]$; 2) the spins on M' only reside in the t_{2g} magnetic orbitals, allowing for antiferromagnetic interactions to occur; or 3) both the t_{2g} and the e_g magnetic orbitals are present on M'; allowing for both ferromagnetic and antiferromagnetic interactions to occur.[24b]

The work described within this thesis examines the effect of non-symmetrical tetraalkylammonium cations on the synthesis and magnetic properties of PBAs via the reaction of tetraalkylammonium cyanide and $Mn^{II}(OAc)_2$ in aqueous and nonaqueous solvent systems. Previous work with symmetrical $[Me_4N]^+$ and $[Et_4N]^+$ tetraalkylammonium cations has resulted in three novel non-Prussian blue structure PBAs.[24] This chapter gave a brief introduction of magnetism and the methods used to determine the magnetic properties of a material. This was followed by a brief look at magnetic materials and a short history of Prussian blue and its analogues. Chapter 2 describes the synthesis of the asymmetric $[Me_3EtN]^+$, $[Me_2Et_2N]^+$, and $[MeEt_3N]^+$ cations and their cyanide salts. Also, current work on sulfonium cations will be presented. Chapter 3 treats the reactions of $[Me_3EtN]CN$, $[Me_2Et_2N]CN$, and $[MeEt_3N]CN$ with $Mn^{II}(OAc)_2$. The synthesis and current state of analysis for the products of various ratios of nonsymmetric tetraalkylammonium cyanide salt with manganese acetate are discussed. Chapter 4 concludes the thesis with a summary of work and some ideas for future research into the effects of asymmetric cations on PBA syntheses and magnetic properties.

References

(1) (a) White, R. M. *Science* **1985**, *229*, 11. (b) Miller, J. S.; Epstein, A. J. *Chem & Industry* **1996**, *2*, 49. (c) Miller, J. S. *Dalton Trans.* **2006**, 2742.

(2) (a) Mattis, D. C. In *The Theory of Magnetism*; Sringer: New York, 1981. (b) Wood, R. In *Understanding Magnetism*; Tab Books Inc.: Blue Ridge Summit, PA, USA, 1988.

(3) (a) Kahn, O. *Struct. Bonding* **1987**, *68*, 89. (b) Miller, J. S.; Epstein, A. J.; Reiff, W. M. *Science* **1988**, *240*, 40. (c) Miller, J. S.; Epstein, A. J.; Reiff, W. M. *Chem. Rev.* **1988**, *88*, 201. (d) Caneschi, A.; Gatteschi, D.; Sessoli, R.; Rey, P. *Acc. Chem. Res.* **1989**, *22*, 392. (e) Buchachenko, A. L. *Russ. Chem. Rev.* **1990**, *59*, 529. (f) Caneschi, A.; Gatteschi, D.; Ray, P. *Prog. Inorg. Chem.* **1991**, *39*, 331. (g) Kahn, O. *Molecular Magnetism*; VCH Publishers: New York, 1993. (h) Miller, J. S.; Epstein, A. J. *Angew. Chem., Int. Ed. Engl.* **1994**, *33*, 385. (i) Kinoshita, M. *Jpn. J. Appl. Phys.* **1994**, *33*, 5718. (j) Gatteschi, D. *Adv. Mater.* **1994**, *6*, 635. (k) Miller, J. S.; Epstein, A. J. *Chem. Eng. News* **1995**, *73*, 30. (l) Miller, J. S.; Epstein, A. J. *Adv. Chem. Ser.* **1995**, *245*, 161. (m) Miller, J. S.; Epstein, A. J. *Chem. Commun.* **1998**, *13*, 1319. (n) Ovcharenko, V. I.; Sagdeev, R. Z. *Russ. Chem. Rev.* **1999**, *68*, 345.

(4) Drago, R. S. *Physical Methods for Chemists*, 2nd ed.; Surfside: Gainesville, FL, 1992; p 471.

(5) Miller, J. S.; Calabrese, J. C.; Epstein, A. J.; Bigelow, R. W.; Zhang, J. H.; Reiff, W. M. *Chem. Commun.* **1986**, 1026.

(6) (a) Sutter, J.-P.; Kahn, M. L.; Golhen, S.; Ouahab, L.; Kahn, O. *Chem. Eur. J.* **1998**, *4*, 571. (b) Kahn, M. L.; Sutter, J.-P.; Golhen, S.; Guionneau, P.; Ouahab, L.; Kahn, O.; Chasseau, D. *J. Am. Chem. Soc.* **2000**, *122*, 3413. (c) Caneschi, A.; Dei, A.; Gatteschi, D.; Sorace, L.; Vostrikova, K. *Angew. Chem. Int. Ed. Engl.* **2000**, *39*, 246. (d) Dei, A.; Gatteschi, D.; Massa, C. A.; Pardi, L. A.; Poussereau, S.; Sorace, L. *Chem. Eur. J.* **2000**, *6*, 4580. (e) Raebiger, J. W.; Miller, J. S. *Inorg. Chem.* **2002**, *41*, 3308. (f) Kahn, M. L.; Ballou, R.; Porcher, P.; Kahn, O.; Sutter, J.-P. *Chem. Eur. J.* **2002**, *8*, 525.

(7) Lee, E. W. *Magnetism: An Introductory Survey*; Dover Publications; New York, 1984.

(8) Moskowitz. L. R. *Permanenet Magnet Design and Application Handbook*, 2nd ed.; Krieger Publishing Company; Florida, 1995.

(9) (a) Miller, J. S. *Adv. Mater.* **2002**, 14, 1105. (b) Miller, J. S. *Dalton Trans.* **2006**, 2742. (c) Miller, J. S. *Chem. Soc. Rev.* **2011**, 8, 525.

(10) (a) Miller, J. S.; Epstien, A. J.; Reiff, W. M. Mol. Cryst. Liq. Cryst. **1985**, 120, 27. (b) Miller, J. S.; Calabrese, J. C.; Epstien, A, J.; Bigelow, R. W.; Zhang, J. H.; Reiff, W. M. L. Chem. Soc., Chem Commun. **1986**, 1026.

(11) Manriquez, J. M.; Yee, G. T.; McLean, R. S.; Epstien, A. J.; Miller, J. S. *Science* **1991**, 252, 1415.

(12) (a) Anonymous *Miscellanea Berolinensia ad Incrementum Scientiarum* **1710**, *1*, 377-378. (b) Ludi, A.; Güdel, H. U. *Struct. Bonding (Berlin)* **1973**, *14*, 1. (c) Dunbar, K. R.; Heintz, R. A. *Prog. Inorg. Chem.* **1997**, *45*, 283.

(13) (a) Keggin, J. F.; Miles, F. D. *Nature* (London) **1936**, 137, 577. (b) Ludi, A.; Güdel, H. U. *Struct. Bonding (Berlin)* **1973**, *14*, 1-21.

(14) (a) Ludi, A.; Güdel, H. U. *Helv. Chim. Acta* **1968**, 51, 2006. (b) Ludi, A.; Güdel, H. U. *Inorg. Chem.* **1970**, 9, 2224. (c) Güdel, H. U. *Acta Chem. Scand.* **1972**, 26, 2169. (d) Buser, J. H.; Ludi, A.; Güdel, H. U. *J.Chem. Soc., Chem. Commun.* **1973**, 1299. (e) Güdel, H. U.; Stuki, H.; Ludi, A. *Inorg. Chem. Acta* **1973**, 7, 121.

(15) (a) Shriver, D. F.; Shriver, S. A.; Anderson, S. E. *Inorg. Chem.* **1965**, *4*, 725. (b) Brown, D. B.; Shriver, D. F. *Inorg. Chem.* **1969**, *8*, 37. (c) House, J. E.; Bailar, J. C. *Inorg. Chem.* **1969**, *8*, 672. (d) Brown, D. B.; Shriver, D. F.; Schwartz, L. H. *Inorg. Chem.* **1968**, *7*, 77. (e) Caneschi, A.; Gatteschi, D.; Rey, P.; Sessoli, R. *Inorg. Chem.* **1988**, *27*, 1756. (f) Entley, W. R.; Girolami, G. S. *Inorg. Chem.* **1994**, *33*, 5165. (g) Reguera, E.; Bertrán, J. F.; Nuñez, L. *Polyhedron* **1994**, *13*, 1619.

(16) (a) Bozorth, R. M.; Williams, H. J.; Walsh, D. E. *Phys. Rev.* **1956**, *103*, 572. (b) Holden, A. N.; Matthias, B. T.; Anderson, P. W.; Lewis, H. W. *Phys. Rev.* **1956**, *102*, 1463. (c) Ito, A.; Suenaga, M.; Ôno, K. *J. Chem. Phys.* **1968**, *48*, 3597. (d) Herren, F.; Fischer, P.; Ludi, A.; Hälg, W. *Inorg. Chem.* **1980**, *19*, 956.

(17) Marvaud, V.; Decroix, C.; Scuiller, A.; Guyard-Duhayon, C.; Vaissermann, J.; Gonnet, F.; Verdaguer, M. *Chem., Eur. J.***2003**, 9, 1677.

(18) Juszczyk, S.; Johansson, C.; Hanson, M.; Ratuszna, A.; Malecki, G. *J. Phys.: Condens. Matter* **1994**, 6, 5697.

(19) Babel, D.; Kurtz, W. in *Solid State Chemistry* 1982, metselaar, R.; Heijligers, H. J. M., Schoonman, J., Eds.; Elsevier, Amsterdam, 1983, p. 593.

(20) Ferlay, S.; Mallah, T.; Ouahes, R.; Veillet, P.; Verdaguer, M. *Nature* (London) **1995**, 378, 701.

(21) (a) Buschmann, W. E.; Paulson, S. C.; Wynn, C. M.; Girtu, M.; Epstein, A. J.; White, H. S.; Miller, J. S. *Adv. Mater.* **1997**, 9, 645. (b) Buschmann, W. E.; Paulson, S. C.; Wynn, C. M.; Girtu, M.; Epstein, A. J.; White, H. S.; Miller, J. S. *Chem. Mater.***1998**, 10, 1386.

(22) Entley, W. R.; Girolami, G. S. *Inorg. Chem.***1994**, 33, 5165.

(23) (a) Holmes, S. M.; Girolami, G. S. *J. Am. Chem. Soc.***1999**, 121, 5593. (b) Holmes, S. M. Ph.D. Thesis, University of Illinois at Urbana-Champaign, **2000**.

(24) (a) Kareis, C. M.; Her, J. H.; Stephens, P. W.; Moore, J. G.; Miller, J. S. *Chem. A: Eur. J.* **2012**, 18, 9281. (b) Kareis, C. M. Ph.D. Thesis, University of Utah, **2013**.

CHAPTER 2

SYNTHESIS OF NONSPHERICAL CATION CYANIDE SALT PRECURSORS

Introduction

The synthesis of Mn(II) PBAs containing tetraalkylammonium cations differ from PB and the majority of other PBAs in the mechanism of their syntheses. Rather than using the traditional route of discrete molecular building blocks, i.e. hexacyanometalates and solvated transition metal ions, this new class of PBAs uses cyanide salts along with Mn(II) salts. It has been shown that reactions of spherical tetraalkylammonium cyanide salts of the nature $[NR_4]CN$, where R = Me or Et, with Mn(II) salts (e.g. $MnCl_2$ or $Mn(O_2CCH_3)_2$) in either aqueous or non-aqueous media has resulted in PBAs of unique and anomalous structures.[1] It is reasonable to think that using a nonspherical ammonium cation may lead to new PBA structures containing new bonding motifs.

This chapter outlines the synthesis of the nonspherical tetraalkylammonium cyanide cations $[NMe_3Et]^+$, $[NMe_2Et_2]^+$, and $[NMeEt_3]^+$. The use of these cations in the synthesis of novel PBAs will be covered in later chapters. Also, the shortcomings of published synthetic routes to $[MNe_2Et_2]CN$ are discussed along with a new synthetic route that overcomes these

shortcomings. The synthesis of nonsymmetrical sulfonium cations was investigated. The synthetic limitations as well as current work on nonspherical sulfonium cations will be presented at the end of this chapter.

Experimental

General procedures. NaCN, $OC(OCH_3)_2$ (dimethyl carbonate), $ClCOOCH_3$ (methyl chloroformate), NMe_2Et, $[NMeEt_3]Cl$, and $[NEt_2H_2]Cl$ were used as purchased. $NMeEt_2$ was distilled over NaH. Methanol (MeOH) was purified via distillation under positive N_2 pressure using a sodium dispersion as the drying agent. Diethyl ether (Et_2O) was purified via distillation under positive N_2 pressure using a sodium dispersion and benzophenone as the drying agent. All other solvents were distilled from the appropriate drying agents under a positive dry N_2 pressure.

Physical methods. Infrared spectra were recorded from 400 to 4000 cm^{-1} on a Bruker Tensor 37 spectrometer (±1 cm^{-1}) operated with an OPUS computer interface. Samples were prepared as KBr (dried) pellets or as nujol mulls. Nuclear Magnetic Resonance (NMR) analysis was performed on a UNITY 300 NMR.

Synthesis. $[NMe_3Et]Cl$ (1). Via Schlenk-line techniques, to a stirring 13 mL dichloromethane solution of N,N-dimethylethylamine (1.46 g, 19.9 mmol) in a salt water ice bath was added drop-wise a 5 mL dichloromethane solution of methylchloroformate (1.39 g, 14.7 mmol) over a 10-min period. The reaction solution was allowed to warm up to room temperature over 8 hr. A white

precipitate was formed. The reaction solution was gently heated for 1 hr. The white precipitate was isolated via filtration, then was washed with 5 x 5 mL of cold CH_2Cl_2 and dried under reduced pressure (Yield: 1.3393 g, 74%). IR (KBr): 3374, 3009, 1017, 960, 882 cm^{-1}; ^1H NMR (300 MHz, D_2O, 25 °C) δ:1.30-1.36 (tt, J_1=7.29 Hz, J_2=2.13 Hz, 2H), 3.06 (s, 9H), 3.33-3.40 (q, J=7.35 Hz, 3H).

[NMe_3Et]CN (2). Via a cannula transfer, a 10 mL methanol solution of [NMe_3Et]Cl (3.49 g, 28.3 mmol) was added to a stirring 25 mL cloudy methanol solution containing NaCN (2.4 g, 49.2 mmol). A white precipitate formed. Reaction was stirred for 18 hr. Reaction slurry was filtered through celite. Filtrate was taken to dryness, resulting in an off-white/pink solid. To the reaction flask of the solid was added 40 mL of dry MeCN and stirred for 4 hr. Reaction slurry was filtered through celite and filtrate was taken to dryness to isolate product (Yield: 1.36 g, 42%). IR (KBr) 3426, 3007, ν_{CN} 2072, 1019, 960, 880 cm^{-1}; ^1H NMR (300 MHz, D_2O, 25 °C) δ:1.29 (tt, J_1=7.29 Hz, J_2= 2.01 Hz, 2H), 3.06 (s, 9H), 3.36 (q, 3H).

[NMe_2Et_2]Cl (3a). To a PTFE liner was added diethylamine hydrochloride (1.12 g, 11.7 mmol) and dimethyl carbonate (5.35 g, 59.3 mmol) with a stir bar. The liner was flushed with N_2, capped, and placed in a steel pressure vessel. The stirring reaction solution was heated to 170 °C and left to stir for 18 hr. The steel bomb was cooled by passing a gentle stream of air over the pressure vessel. Upon cooling, ~ 40 mL of acetone was added to the reaction mixture and stirred. A white precipitate formed and was isolated via filtration. The crude product (Yield: 1.12 g, 69%) was dried under reduced pressure. This product

was recrystallized from methanol and ether. IR (KBr) 3462, 3005, 1015, 970, 921, 823 cm^{-1}; ^1H NMR (300 MHz, D_2O, 25 °C) δ:1.24-1.32 (tt, J_1=7.28 Hz, J_2= 1.91 Hz, 4H), 2.97 (s, 6H), 3.27-3.35 (q, J=7.30 Hz, 6H).

[NMe_2Et_2]Cl (3b). Via Schlenk-line techniques, to a stirring 15 mL dichloromethane solution of N,N-diethylmethylamine (2.95 g, 33.87 mmol) in a salt water ice bath was added drop-wise a 10 mL dichloromethane solution of methylchloroformate 3.18 g, 33.65 mmol) over a 15-min period. The formation of a white precipitate was observed. The reaction solution was allowed to warm up to room temperature over 18 hr. The reaction solution was colorless. The reaction solution was gently heated for 0.5 hr. The white product was isolated by drying on a roto-evaporator under reduced pressure (Yield: 4.09 g, 88%). IR (KBr) 3462, 3005, 1015, 970, 921, 823 cm^{-1}; ^1H NMR (300 MHz, D_2O, 25 °C) δ:1.26-1.33 (tt, J_1=7.32 Hz, J_2= 2.02 Hz, 4H), 2.97 (s, 6H), 3.28-3.35 (q, J=7.31 Hz, 6H).

[NMe_2Et_2]CN (4). Via a cannula transfer, a 15 mL methanol solution of [NMe_2Et_2]Cl (1.91 g, 13.88 mmol) was added to a stirring 30 mL cloudy methanol solution containing NaCN (1.15 g, 23.47 mmol). A white precipitate formed. Reaction was stirred for 18 hr. Reaction slurry was filtered through celite. Filtrate was taken to dryness, resulting in an off-white/pink solid. To the round bottomed flask (RBF) containing solid was added ~40 mL of dry MeCN and stirred for 4 hr. Reaction slurry was filtered through celite and filtrate was taken to dryness to isolate product (Yield: 1.45 g, 81%). IR (KBr) 3438, 2989, ν_{CN}

2071, 1016, 970, 922, 821 cm^{-1}; ^1H NMR (300 MHz, D_2O, 25 °C) δ:1.27-1.33 (tt, J_1=7.31 Hz, J_2= 1.69 Hz, 4H), 3.06 (s, 6H), 3.28-3.36 (q, J=7.36 Hz, 6H).

[NMeEt$_3$]CN (5). Via a cannula transfer, a 15 mL methanol solution of [NMeEt$_3$]Cl (1.13 g, 7.46 mmol) was added to a stirring 30 mL cloudy methanol solution containing NaCN (0.65 g, 13.26 mmol). A white precipitate formed. This reaction was stirred for 18 hr and was filtered through celite. The filtrate was taken to dryness, resulting in an off-white/pink solid. To the RBF containing solid was added ~40 mL of dry MeCN and stirred for 4 hr. The reaction slurry was filtered through celite and the filtrate was taken to dryness to isolate the product (Yield: 0.663 g, 62%). IR (KBr) 2986, ν_{CN} 2054, 1496, 1457, 1005, 959, 875 cm^{-1}; ^1H NMR (300 MHz, D_2O, 25 °C) δ:1.27 (tt, J_1=7.29 Hz, J_2= 1.86 Hz, 6H), 3.06 (s, 3H), 3.28 (q, J=7.30 9H).

Results and Discussion

Synthesis. The synthesis of the [NMe$_2$Et$_2$]Cl was first attempted by following already published synthetic routes.[2] After several attempts to synthesize a pure product, it was determined that both published synthetic routes did not reliably yield a pure product. One published method consisted of reacting diethylamine hydrochloride with dimethyl carbonate in a sealed vessel at elevated temperatures.[2a] This method produced a pure compound ~25% of the time. The other ~75% of the reactions resulted in an impurity that could not be removed. The second published method added 1-methyl-3-ethyl-imidizolium bromide salt as a catalyst to the first method.[2b] In this case, the impurity

appeared as a product in every reaction attempt. Based on NMR data, the author believes that the impurity is $[NMe_4]Cl$. Purification was attempted using recrystallization and alumina column separation. A system has yet to be devised that can separate the impurity from the desired product. Because of the success of synthesizing $[NMe_3Et]Cl$ from NMe_2Et and methylchloroformate, a novel synthesis of $[NMe_2Et_2]Cl$ from $NMeEt_2$ and methylchloroformate was proposed. This reaction yielded a pure product in good yield (88%). The published methods were abandoned due to poor purity of product. The synthesis method **3a** is included in this chapter because some of the compounds in Chapter 3 were synthesized using $[NMe_2Et_2]CN$ made by this route.

Infrared spectroscopy. The IR spectra of compound 1 **(**Figure 2.1a) exhibits expected ν_{CH} absorptions in the 2950-3000 cm^{-1} region. The IR spectrum of compound **2** (Figure 2.1b) exhibits the same peaks as compound **1** with the exception of the sharp ν_{CN} absorption that grew in at 2073 cm^{-1}. A similar trend is seen for compounds **3a** and **3b** (Figure 2.2a)**,** and **4** (Figure 2.2b). Figure 2.3 shows the the ν_{CN} absorption at 2051 cm^{-1}. Due to the hydrophilic nature of these salt complexes, adsorbed water is usually present in the IR spectra. Water is responsible for the broad peak in the 3200-3500 cm^{-1} region as well as the peak near 1600 cm^{-1}.

Nuclear magnetic resonance analysis. Nuclear magnetic resonance (NMR) spectroscopy was used to determine if the product obtained was the desired product and if the product was free of any impurities or side products.

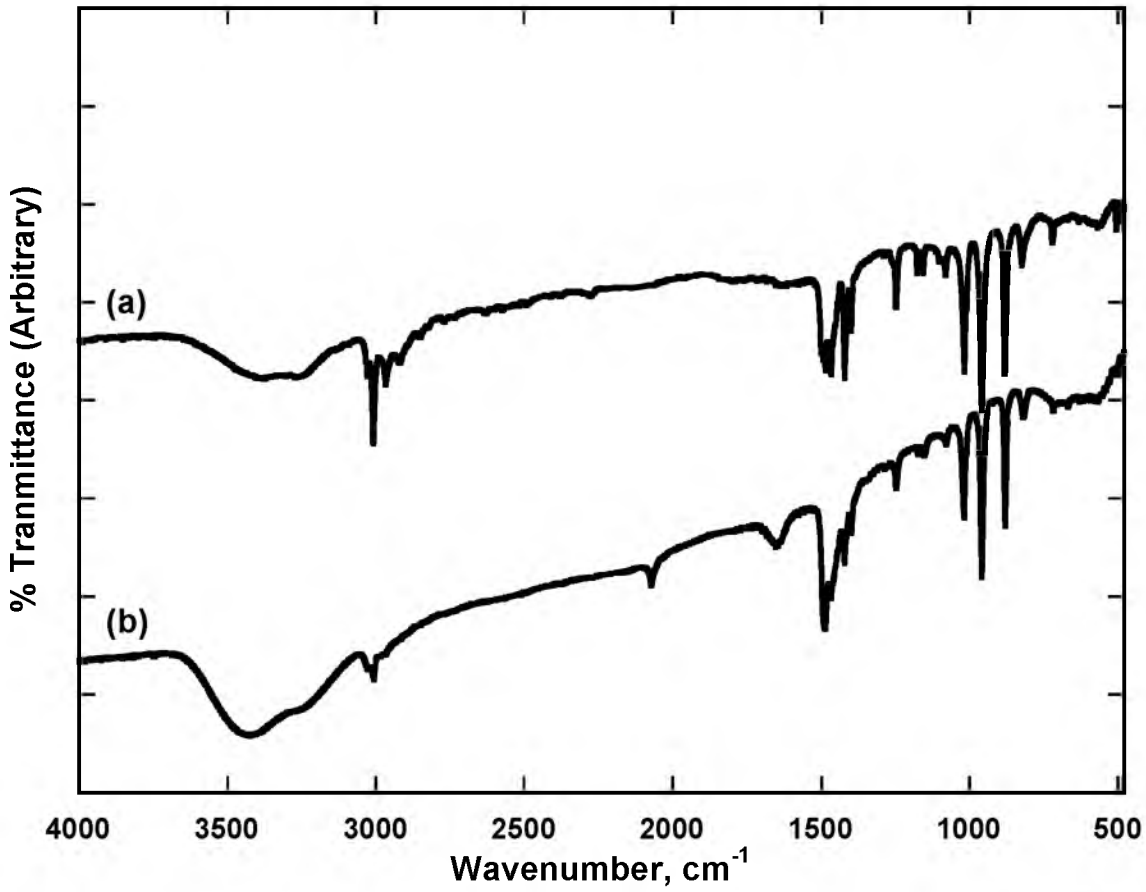

Figure 2.1 IR spectra of (a) [NMe_3Et]Cl (**1**) and (b) [NMe_3Et]CN (**2**).

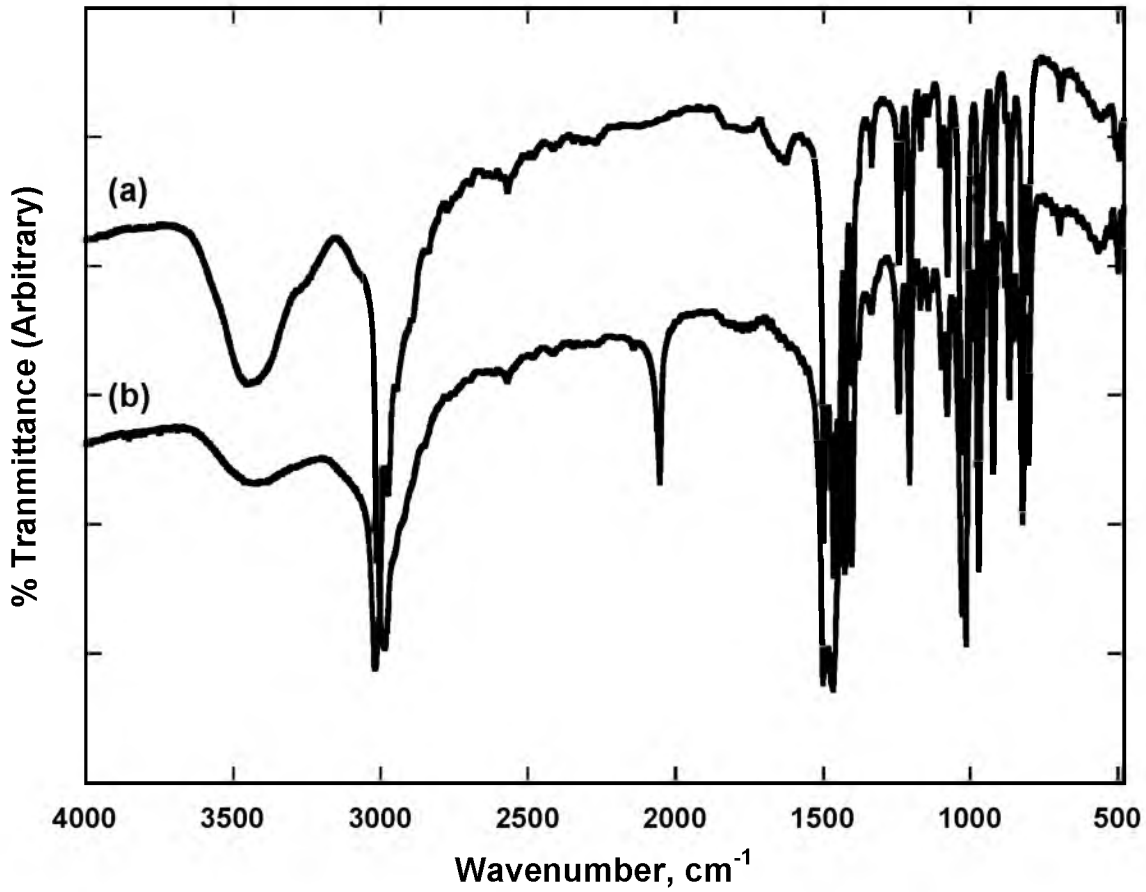

Figure 2.2 IR spectra of (a) $[NMe_2Et_2]Cl$ (**3a**) and (b) $[NMe_2Et_2]CN$ (**4**).

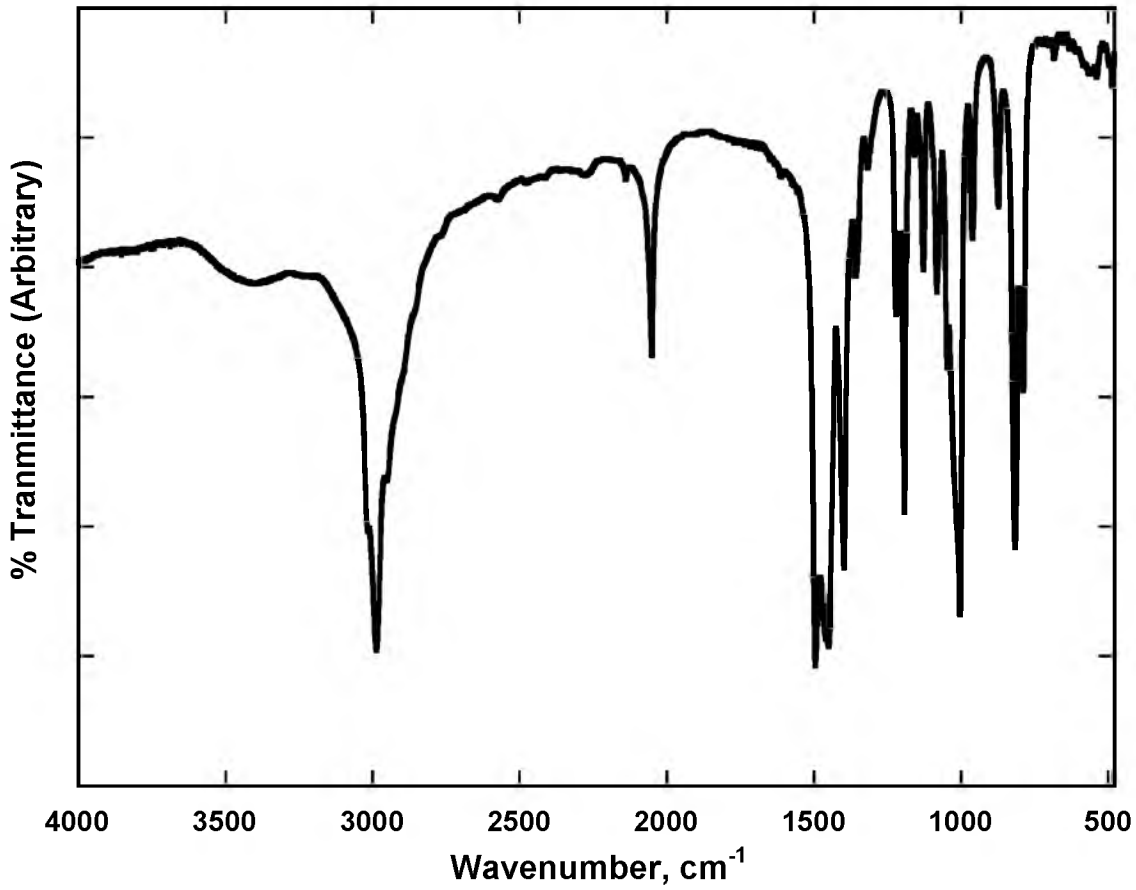

Figure 2.3 IR spectrum of [$NMeEt_2$]CN (**5**).

^{1}H NMR was used extensively in this analysis due to the quantifiable information that can be obtained regarding the number of protons. Spectra of all samples were recorded in deuterium oxide (D_2O) due to the excellent solubility of these salts in H_2O.

[NMe_3Et]Cl (1). The ^{1}H NMR spectrum, Figure 2.4, of **1** consists of a quartet centered at 3.36 ppm, a singlet at 3.06 ppm, and a triplet of triplets centered at 1.33 ppm. The quartet, singlet, and triplet of triplets integrate in a 2:9:3 ratio. The -CH_2- in the ethyl chain should be split by the 3 protons on the –CH_3. The resulting quartet and ratio are consistent with this assignment. The singlet integrating to 9 protons is consistent with 3 methyl groups bound directly to a nitrogen atom. The triplet of triplets is the terminal –CH_3 on the ethyl chain. The integration and shift are consistent with the assignment. However, the splitting pattern, triplet of triplets, is not consistent with a splitting pattern usually assigned to a terminal –CH_3 in an alkyl chain. However, this splitting is consistent throughout all of the cations synthesized in this work.

[NMe_3Et]CN (2). The ^{1}H NMR spectrum, Figure 2.5, of **2** consists of a quartet centered at 3.36 ppm, a singlet at 3.05 ppm, and a triplet of triplets centered at 1.33 ppm. The quartet, singlet, and triplet of triplets integrate in a 2:9:3 ratio. The difference between **1** and **2** is the counter ion. Since the counter ion is ionically bonded, it is not expected that the chemical shifts of the observed protons would shift significantly. The ^{1}H NMR spectrum supports that **2** is the desired compound and is free of impurities.

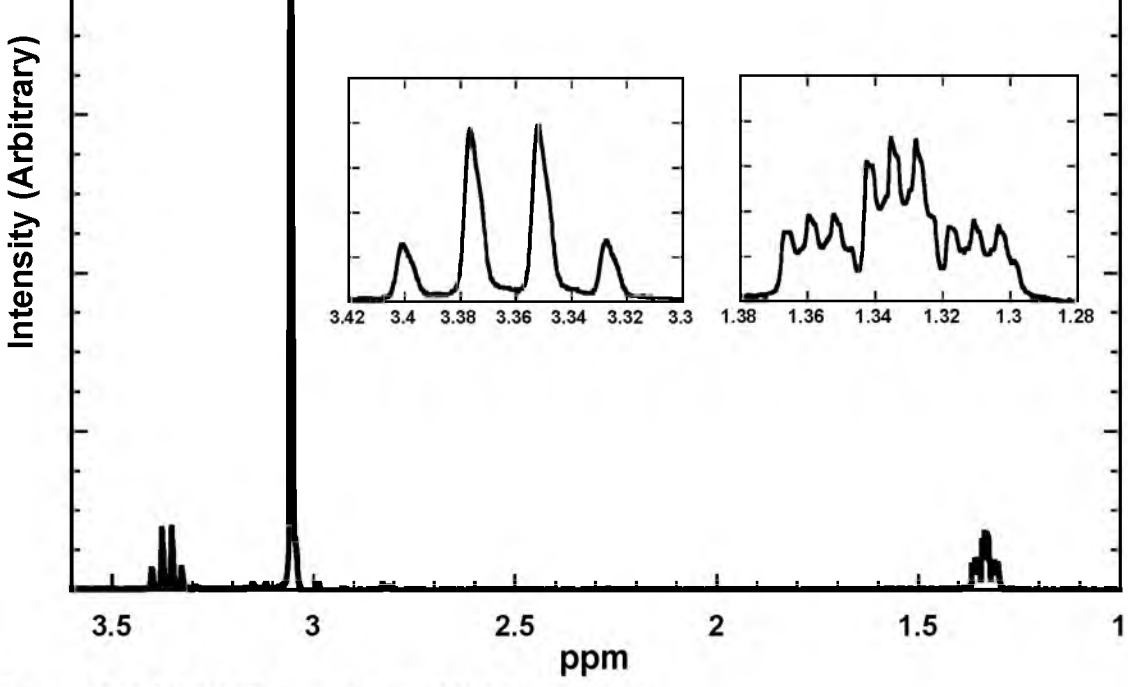

Figure 2.4 ^{1}H NMR spectrum of [NMe_3Et]Cl (**1**).

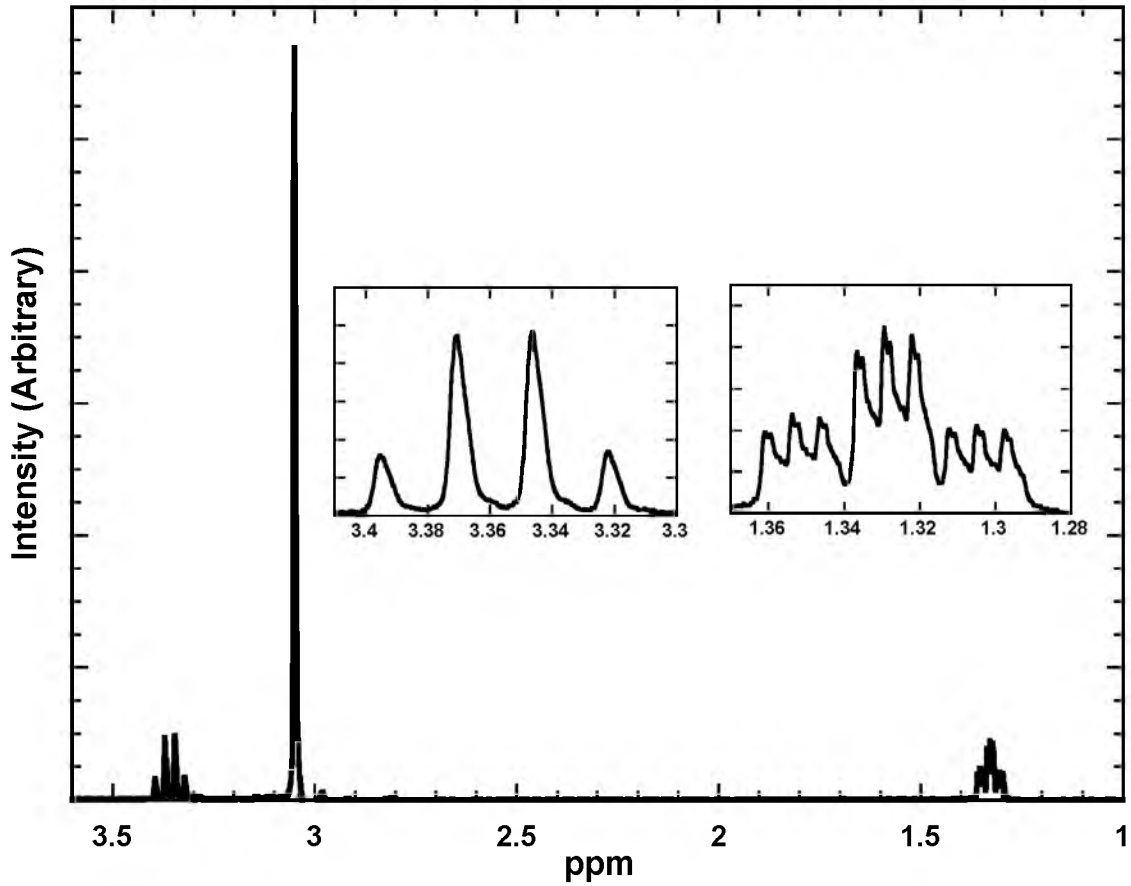

Figure 2.5 ^{1}H NMR spectrum of [NMe_3Et]CN (**2**).

[NMe_2Et_2]Cl (3a). The ^1H NMR spectrum, Figure 2.6, of **3a** consists of a quartet centered at 3.36 ppm, a singlet at 3.06 ppm, and a triplet of triplets centered at 1.33 ppm. The quartet, singlet, and triplet of triplets integrate in a 2:3:3 ratio. The singlet at 3.06 ppm is indicative of the desired methyls bonded to the nitrogen. The quartet and triplet of triplets are in accord with the presence of ethyl chains bounded directly to the nitrogen center. The ratio of peak integration is consistent with an ammonium cation composed of 2 methyl and 2 ethyl groups bound to the nitrogen. The ^1H NMR spectrum indicates a pure ammonium salt.

[NMe_2Et_2]Cl (3b). The ^1H NMR spectrum, Figure 2.7, of **3b** indicates that a pure compound can be obtained through this synthetic route as well. The product was the same compound as **3a**.

[NMe_2Et_2]CN (4). The ^1H NMR spectrum, Figure 2.8, of **4** is consistent with the ^1H NMR spectrum of **3a** and **3b**. There is no apparent change to the compound aside from the exchange of counter ions. The product from this reaction appears to be pure as far as NMR analysis can determine.

[$NMeEt_3$]CN (5). The ^1H NMR spectrum, Figure 2.9, of **5** consists of a quartet centered at 3.36 ppm, a singlet at 3.06 ppm, and a triplet of triplets centered at 1.33 ppm. The quartet, singlet, and triplet of triplets integrate in a 2:1:3 ratio. The ratio is indicative of a tetraalkylammonium cation composed of a single methyl and 3 ethyl groups bound to the central nitrogen. All shifts and peak shapes are consistent with predicted shifts and peaks of **5**. Through NMR analysis, there does not appear to be any side products present in the desired product.

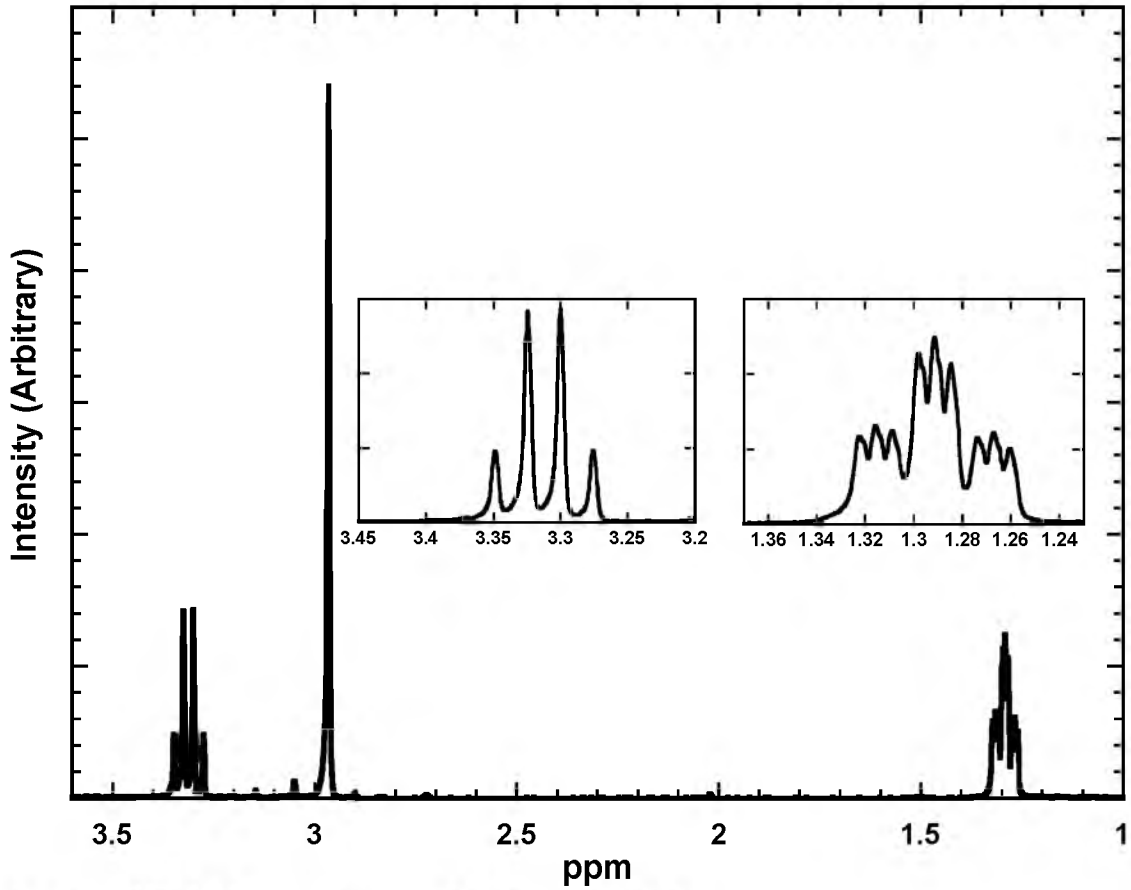

Figure 2.6 ^{1}H NMR spectrum of $[NMe_2Et_2]Cl$ (**3a**).

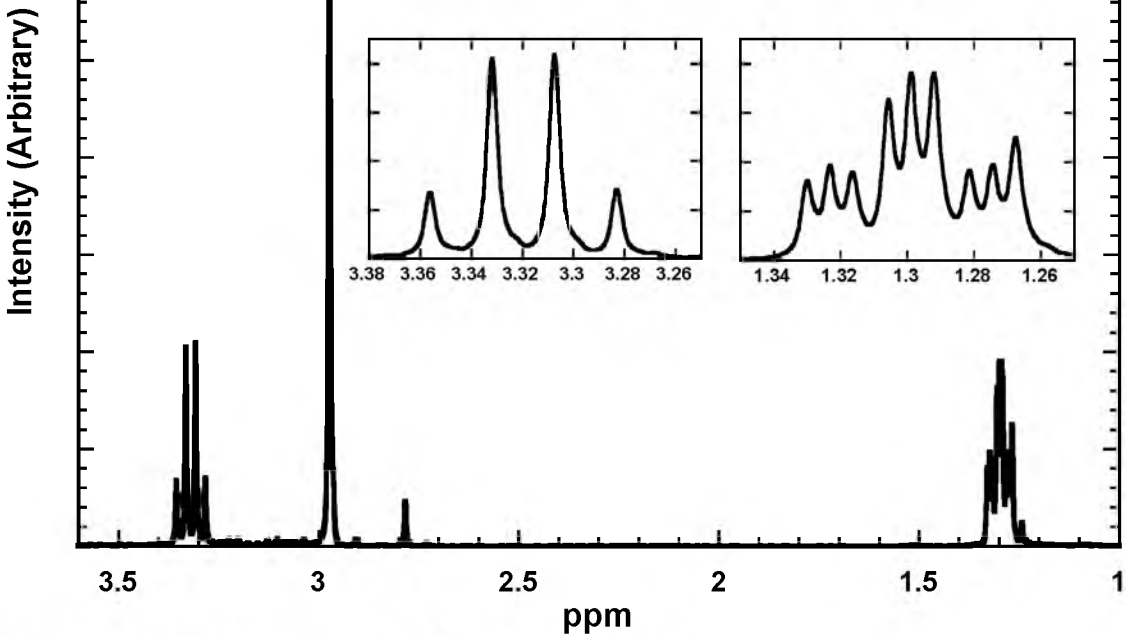

Figure 2.7 ^{1}H NMR spectrum of $[NMe_2Et_2]Cl$ (**3b**).

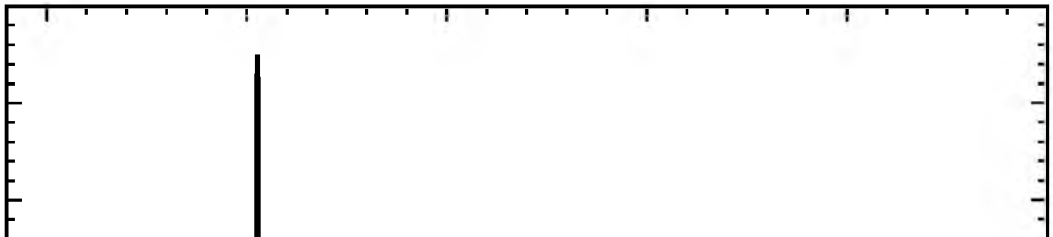

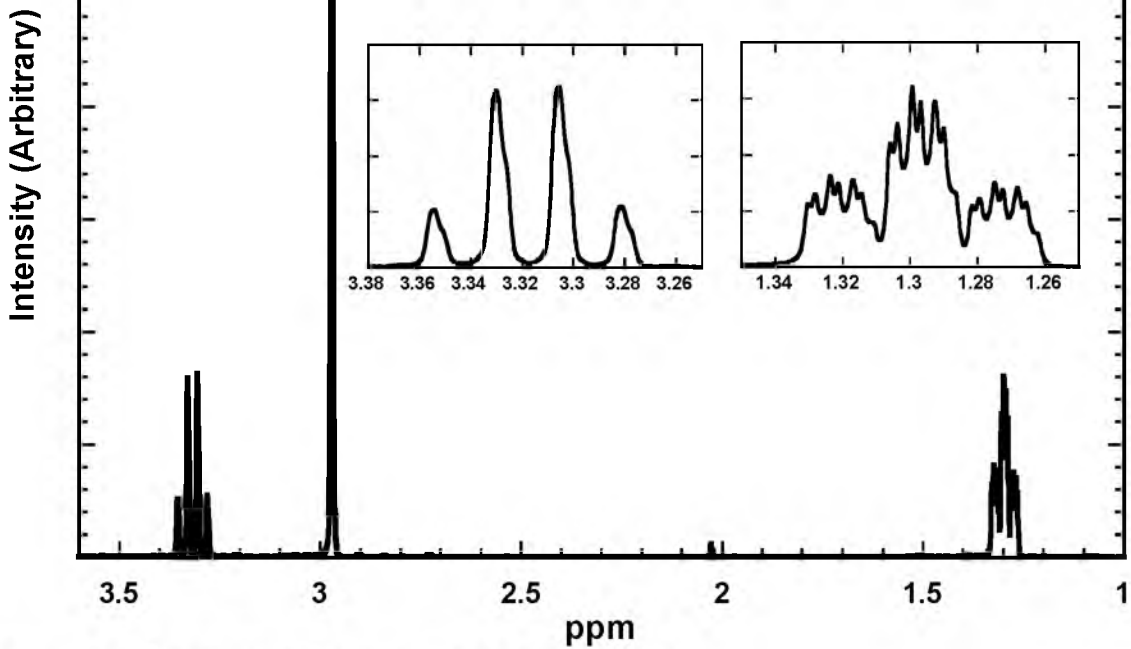

Figure 2.8 ^{1}H NMR spectrum of $[NMe_2Et_2]CN$ (**4**).

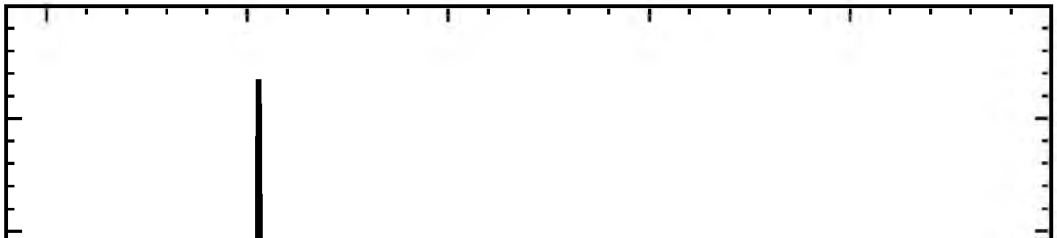

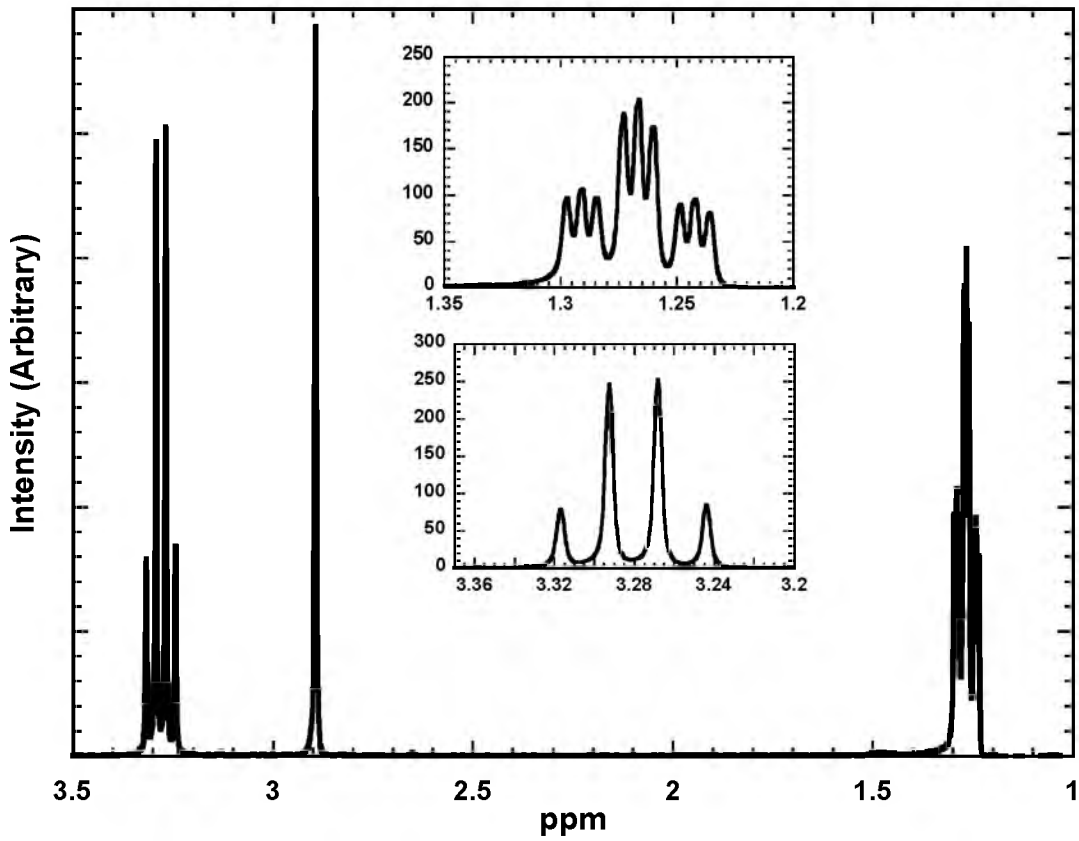

Figure 2.9 ^{1}H NMR spectrum of **[**$NMeEt_3$]CN (**5**).

Work on Nonspherical Sulfonium Cations

In the work presented in this thesis, the nonspherical cations are all of the same family, namely $[NR_xR'_{4-x}]^+$ where R = Me and R' = Et. Through the course of this research, the notion of having lone-pairs of electrons on the cation was proposed. Initially, it was proposed that trimethyl sulfonium or trimethyl sulfoxonium cations be used. In the process of trying to synthesize sulfonium cations with lone pairs, it was found that cyanide salts could not be formed with sulfonium cations with lone-pairs on the sulfur atom.

Synthesis. The typical synthesis for the cyanide salt is to take a chloride salt analogue and do an ion exchange with a cyanide salt, i.e. NaCN. However, trimethyl sulfonium and trimethyl sulfoxonium chloride salts are not readily available. An initial attempt to synthesize trimethyl sulfoxonium chloride by methylating dimethylsulfoxide with methyl chloroformate according to Scheme 2.1 did not produce the desired product **6**.

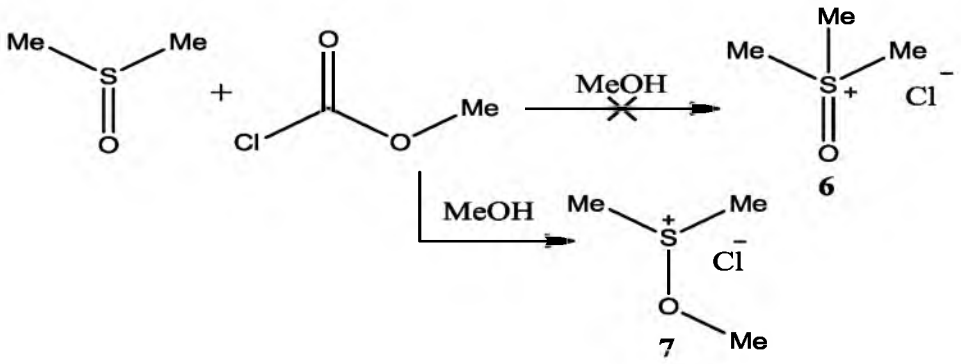

Scheme 2.**1** The formation of product 7 from the reaction of DMSO and methyl chloroformate.

Product **7** was formed when the oxygen was methylated instead of the sulfur. The crude product of Scheme 2.1 was analyzed by NMR spectroscopy. The ^{1}H NMR spectrum, Figure 2.10, has a singlet at 4.02 ppm, a singlet at 3.28 ppm, and a singlet at 2.68 ppm. The singlets at 4.02 ppm and 3.28 ppm are at predicted shifts[3] for **7** and the two singlets integrate to a 3:6 ratio. ^{13}C NMR analysis, Figure 2.11, indicates a peak at 62.58 ppm, 38.78 ppm, and 33.20 ppm.

The peaks at 62.58 ppm and 33.20 ppm are consistent with reported ^{13}C shifts of **7**.[4] The peak at 2.68 ppm in the ^{1}H NMR spectrum and 38.78 ppm in the ^{13}C NMR spectrum are consistent with the unreacted starting material DMSO.[3] While **7** was not the desired product, it was a product that could be used in the synthesis of a cation of interest. The reaction of **7** with NaCN according to Scheme 2.2 did not produce the intended product, **8**. Instead, it is believed that the reaction proceeded to produce **9**. Cyanide is a sufficiently strong base that deprotonation occurred instead of a simple ion exchange. It has been found that if there are only 3 bonds to the sulfur atom, the cyanide will deprotonate one of

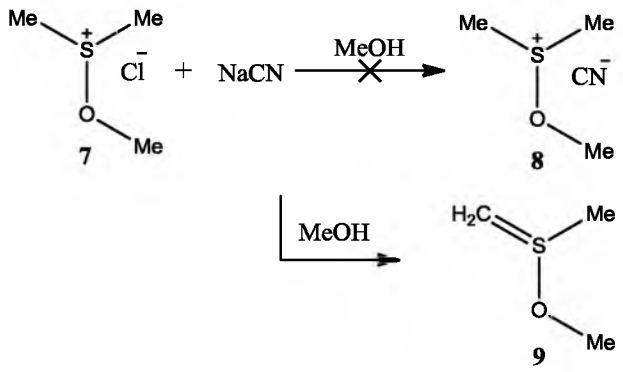

Scheme 2.2 Reaction of **7** with sodium cyanide.

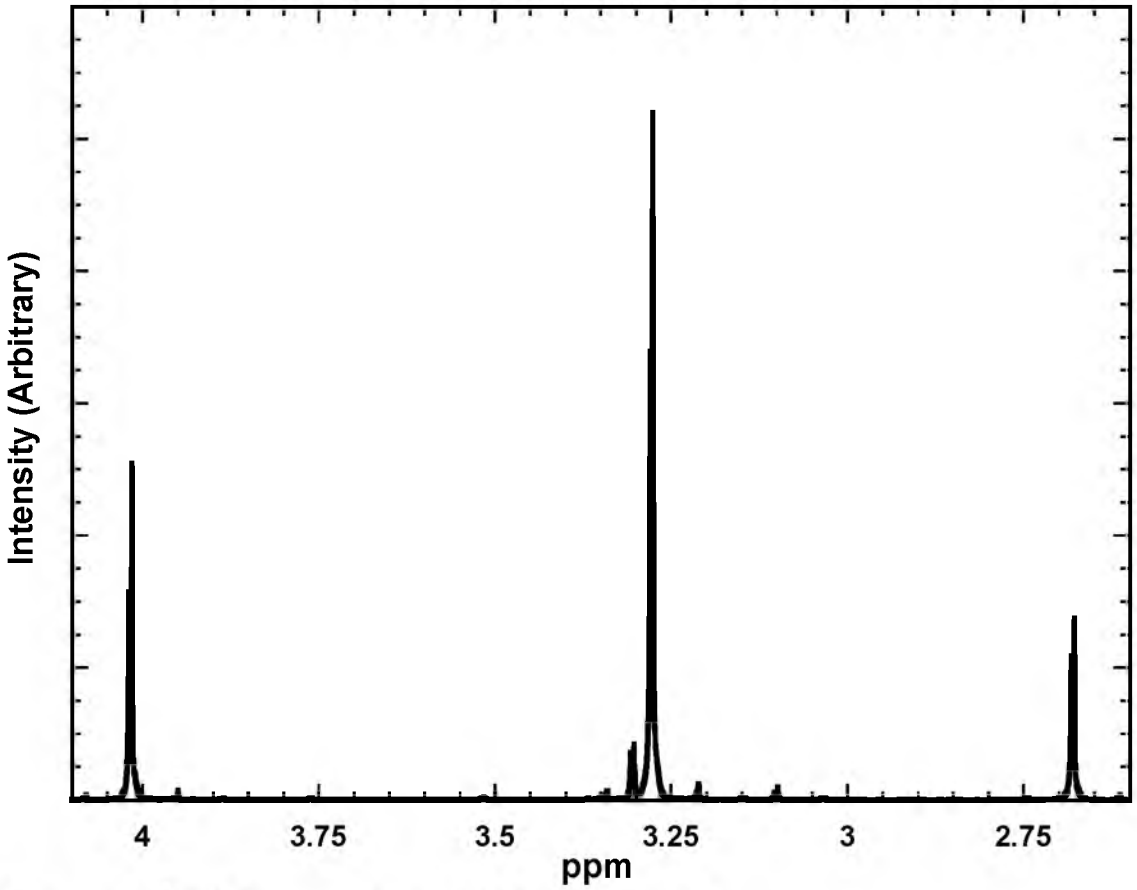

Figure 2.10 ^{1}H NMR spectrum of $[Me_2SOMe]Cl$ **(7).**

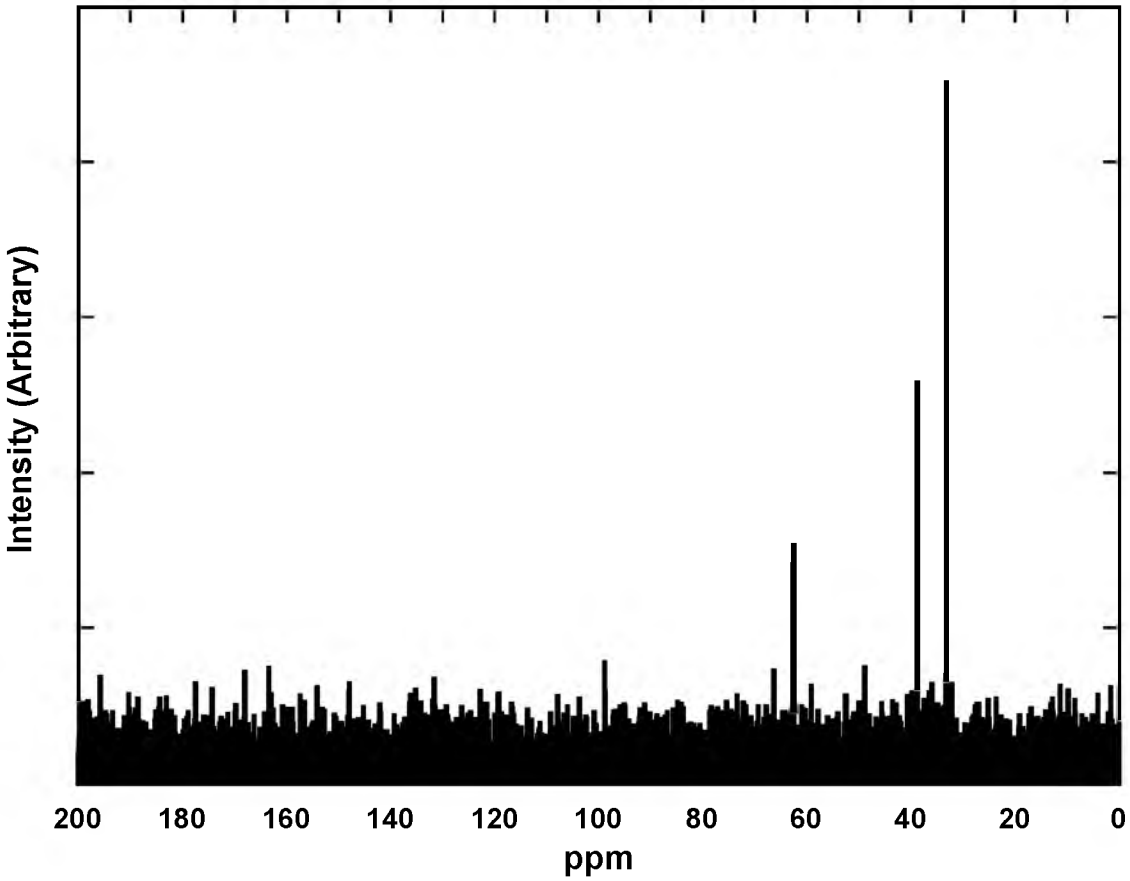

Figure 2.11 ^{13}C NMR spectrum of $[Me_2SOMe]Cl$ (**7**).

the carbons to form a neutral species that contains a double bond between the carbon and the sulfur. To form a stable sulfonium cation, one of the following two conditions must exist: 1) there are 5 bonds to the sulfur atom, i.e. trimethyl sulfoxonium chloride, or 2) there are no protons available to be deprotonated when only three bonds to the sulfur exist, i.e. trimethoxy sulfonium chloride.

These results have led to the proposal of several sulfur-containing cations that could form potentially interesting PBAs due to size and asymmetry. A reaction of 9 with methyl chloroformate, Scheme 2.3, should form a sulfonium chloride salt. Due to the sulfur having 5 bonds, it is likely that the reaction of the sulfonium chloride salt with sodium cyanide would undergo a simple cation exchange and result in 11. Another novel cation could be formed by the conversion of trimethyl sulfonium iodide into trimethyl, methane sulfonium cyanide, Scheme 2.3. A strong base, i.e. CN^- or NaH, could be used to convert trimethyl sulfonium iodide to **12**. A methylation using methylchloroformate followed by an ion exchange, Sceme 2.4, could result in trimethyl, methane sulfonium cyanide. The reaction of this cyanide salt with a manganese salt may

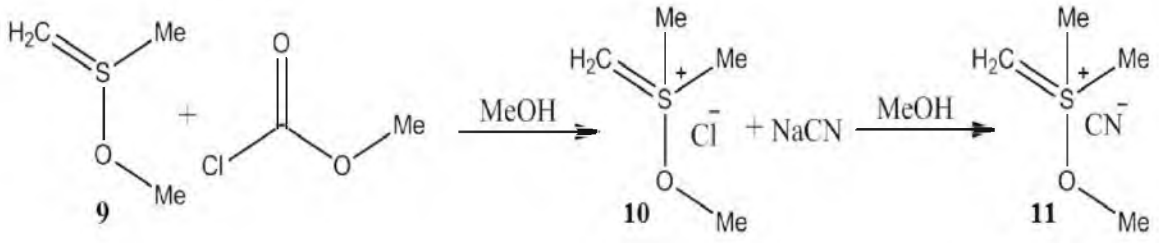

Scheme 2.3 Proposed route for synthesis of novel sulfonium cation.

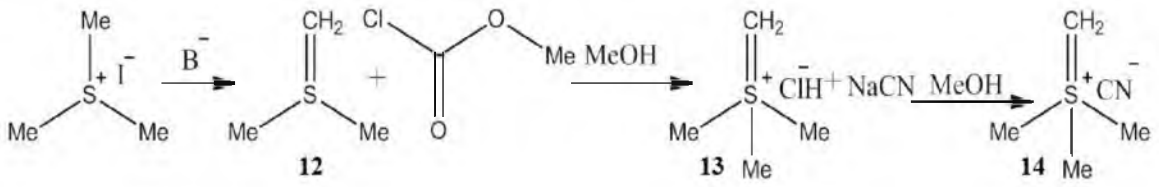

Scheme 2.4 Proposed route for synthesis of novel trimethyl, methane sulfonium cyanide salt.

result in a novel PBA structure. Intial work has begun on the synthesis of compound **12**. At the time of writing this chapter, no conclusive results have been obtained.

Conclusion

The use of nonsymmetric tetraalkylammonium cations in the synthesis of PBAs could yield novel structures and greater insight into magnetic phenomenon. Presented in this chapter is the synthesis of three nonsymmetric tetraalkylammonium cations, e.g. $[NMe_3Et]^+$, $[NMe_2Et_2]^+$, and $[NMeEt_3]^+$. The characterization of the compounds was also presented and discussed. Also addressed in this chapter was the ongoing work toward synthesizing sulfonium cations that may result in novel PBAs.

References

(1) (a) Kareis, C. M.; Her, J. H.; Stephens, P. W.; Moore, J. G.; Miller, J. S. *Chem. A: Eur. J.* **2012**, 18, 9281. (b) Kareis, C. M. Ph.D. Thesis, University of Utah, **2013**.

(2) (a) Zhao, B.; Greiner, L.; Leitner, W. *Chem. Commum.* **2011**, 47, 2973-2975. (b)Zheng, Z. Q.; Wang, J.; Wu, T. H.; Zhou, X. P. *Adv. Synth. Catal.* **2007**, 349, 1095-1101.

(3) Predicted NMR data calculated using Advanced Chemistry Development, Inc. (ACD/Labs) Software V11.01 (© 1994-2012 ACD/Labs)

(4) Olah, G. A.; *J. Am. Chem. Soc.* **1979**, 101, 18, 5317-22.

CHAPTER 3

SYNTHESIS OF NON-PRUSSIAN BLUE STRUCTURED PRUSSIAN BLUE ANALOGUES USING $[NMe_3Et]^+$, $[NMe_2Et_2]^+$, AND $[NMeEt_3]^+$ CATIONS

Introduction

The study and investigation of Prussian blue (PB) and Prussian blue analogues (PBAs) have been pivotal in the advancement of the field of molecule-based magnets (MBMs).[1] By following the traditional route to synthesizing PBAs which requires the reaction of a hexacyanometalate and solvated metal ions, PBAs of the following composition have been made: $M'^{III}_4[M^{II}(CN)_6]_3$, $C^+M'^{II}[M^{III}(CN)_6]$, $M'^{II}_3[M^{III}(CN)_6]_2$, $A^+M'^{III}[M^{II}(CN)_6]$, $A^+_2M'^{II}[M^{II}(CN)_6]$ where C is a cation and A^+ is an alkali cation.[1] These PBAs have the following features in common: 1) a face-centered cubic (*fcc*) unit cell, 2) low-spin C-bound $[M(CN)_6]^{n-}$ surrounded by high-spin M'^{II} or M'^{III} that are typically bound to six cyano-nitrogens, and 3) a composition of linear linkages along the three Cartesian axes.[1]

The use of an alternate synthetic route, direct addition of cyanide salts with Mn(II) salts, has yielded PBAs that have the classic PB characteristics as

well as PBAs that have non-Prussian blue structures. The reaction of $[NMe_4]CN$ with $Mn(O_2CCH_3)_2$ yielded a bridged layer compound with a chemical formula of $[NMe_4]_3Mn^{II}_5(CN)_{13}\bullet xSolvent$.[2] Reactions of $[NEt_4]CN$ with $Mn(O_2CCH_3)_2$ yielded the following two non-Prussian blue structured PBAs: $[NEt_4]_2Mn^{II}_3(CN)_8\bullet xH_2O$ and $[NEt_4]Mn^{II}_3(CN)_7\bullet xMeOH$.[3] The size of the cation associated with the cyanide salt appears to have an effect on the bonding motifs and structural outcome of the PBAs. By altering the structure, these cations also affect the magnetic properties of the PBAs.

While the use of spherical cations, e.g. $[NMe_4]^+$ and $[NEt_4]^+$, has been investigated, the possible effects of nonspherical cations has not. It was the author's intent to determine the effects that nonspherical cations, e.g. $[NMe_3Et]^+$, $[NMe_2Et_2]^+$, and $[NMeEt_3]^+$, would have on the structure of PBAs.

This chapter will give an overview of the PBA compounds made using nonspherical quaternary ammonium cations. The chapter is split into three sections, where each section addresses the work done with a particular cation. Each section will begin by discussing the properties of all magnetically pure compounds synthesized and will be followed by a short analysis of the magnetically mixed-phase compounds.

Experimental Section

General procedures. NaCN, $Mn(O_2CCH_3)_2$, $ClCOOCH_3$ (methyl chloroformate), and Me_2EtN were used as purchased. Water (H_2O) was purified through a Barnstead "E-pure" water purification system and deoxygenated

through distillation under N_2. Methanol (MeOH) was purified via distillation under positive N_2 pressure using a sodium dispersion as the drying agent. Diethyl ether (Et_2O) was purified via distillation under positive N_2 pressure using a sodium dispersion and benzophenone as the drying agents. All other solvents were distilled from the appropriate drying agents under a positive dry N_2 pressure. All syntheses were performed in an oxygen-free (<1.0 ppm O_2) wet box.

Physical methods. Infrared spectra were recorded from 400 to 4000 cm^{-1} on a Bruker Tensor 37 spectrometer (±1 cm^{-1}) controlled with an OPUS computer interface. Samples were prepared as KBr (dried) pellets or as Nujol® mulls. Thermogravametric analysis coupled with mass spectrometry (TGA-MS) measurements were performed using a TA Instruments Model 2050 TGA analyzer coupled to a Thermolab TL 1285 thermal analysis-mass spectrometer. These instruments were located in a Vacuum Atmospheres Drilab glove box under N_2 to protect moisture and oxygen-sensitive samples. Samples were loaded on aluminum pans and heated at a rate of 1 ºC/min.

Magnetic susceptibility measurements were made between 5 and 300 K using a Quantum Design MPMS-5 5T superconducting quantum interference device (SQUID) magnetometer with a sensitivity of 10^{-8} emu or 10^{-12} emu/Oe at 1 T and equipped with an ultra-low field (~0.005 Oe) reciprocating sample measurement system, and continuous low temperature control with enhanced thermometry features. Compounds were loaded into gelatin samples for magnetic measurements. The direct current (DC) magnetization temperature

dependence was obtained by cooling the sample in zero-field and collecting data upon warming and then cooling the sample in a field and collecting data upon warming. The remnant magnetization was measured in zero applied field while warming the sample from 5 K. Alternating current (ac) susceptibilities were measured using a Quantum Design PPMS-9 ac/dc susceptometer. The data were corrected for measured diamagnetism of the sample holder and Nujol. Core diamagnetic corrections using Pascal's corrections were used for each sample. The correction will be listed in each synthetic route.

Powder X-ray diffraction (PXRD) data for Rietveld structure analysis was collected at Beamline X16C of the national Synchrotron Light Source at Brookhaven National Labs by Dr. Peter W. Stevens. The samples were sealed under an inert atmosphere in a 1.0 mm diameter thin-wall quartz capillary to protect against moisture or O_2 contamination.

$[NMe_3Et]^+$ Class

Synthesis. $[NMe_3Et]_3Mn_5(CN)_{13}\bullet XH_2O$ (1). To a stirring 1.5 mL aqueous solution of $[NMe_3Et]CN$ (107.11 mg, 0.938 mmol) was added drop-wise a 1.5 mL aqueous solution of $Mn(O_2CCH_3)_2$ (54.46 mg, 0.315 mmol). A grey precipitate formed and then turned yellow within minutes. The reaction mixture was left to stir for 24 hr. The yellow precipitate was isolated via filtration and washed with methanol (4 x 3 mL) and ether (3 x 3 mL), and dried under vacuum at room temperature for 4 hr (yield: 39.80 mg, 71.5%). IR (KBr) ν_{OH} 3629 (w, br), ν_{CN} 2141(w), 2098 (m), 2075 (s), 2049 (s), 1017 (m), 964 (w), 881 (w) cm^{-1}. The

sample used for magnetic analysis contained 0.37 equiv of H_2O. A core diamagnetic correction of -469.3 x 10^{-6} emu/mol was used.

$[NMe_3Et]_5Mn_9(CN)_{23}$•xMeOH (2). To a stirring 4 mL aqueous solution of $Mn(O_2CCH_3)_2$ (90.58 mg, 0.524 mmol) was added drop-wise a 1 mL aqueous solution of $[NMe_3Et]CN$ (111.91 mg, 0.980 mmol). A grey precipitate formed and then turned gold in color within minutes. The reaction slurry was left to stir for 24 hr. The gold precipitate was isolated via filtration and washed with 3 x 3 mL of MeOH and 3 x 3 mL of Et_2O, and dried under vacuum at room temperature for 4 hr (yield: 53.4 mg, 79.6%). IR (KBr) 3428 (w), 2927 (w), 2810 (w), 2148 (m), 2063 (s), 1554 (s), 1050 (s) cm^{-1}. The sample used for magnetic analysis contained 1.25 equivalents of MeOH. A core diamagnetic correction of -827.6 x 10^{-6} emu/mol was used.

$[NMe_3Et]_2Mn_3(CN)_8$•xMeOH (3). To a stirring 4 mL methanol solution of $Mn(O_2CCH_3)_2$ (90.30 mg, 0.522 mmol) was added drop-wise a 4 mL methanol solution of $[NMe_3Et]CN$ (297.58 mg, 2.606 mmol). A grey precipitate formed and then turned gold within minutes. After the complete addition of the methanol solution of $[NMe_3Et]CN$, the reaction slurry began to turn green. The reaction slurry was left to stir for 24 hr. The precipitate was isolated via centrifugation. There appeared to be 2 products, a gold and a green precipitate. After washing the precipitate with 3 mL of fresh MeOH, the precipitate had a uniform green color. The precipitate was washed with an additional 2 x 3 mL of MeOH and 3 x 3 mL of Et_2O, and dried under vacuum at room temperature for 4 hr. IR (KBr) 2922 (w), 2851 (vw), 2133 (w), 2062 (s), 1565 (m), 1487 (m), 1019 (m) cm^{-1}. The

sample used for magnetic analysis contained 0.6 equivalents of MeOH. A core diamagnetic correction of -302.6 x 10^{-6} emu/mol was used.

(4). ~10 mg of **1** was placed in a vial with 3 mL of H_2O. The solid rapidly turned from lime green to light teal. The slurry was allowed to stir for 18 hr. Product was isolated via filtration, washed with 3 x 1 mL of H_2O, 3 x 1 mL of MeOH, and 3 x 1 mL of Et_2O, and then dried under reduced pressure.

(5). To a stirring 1 mL aqueous solution of $Mn(O_2CCH_3)_2$ (153.52 mg, 0.887 mmol) was added drop-wise a 1 mL aqueous solution of $[NMe_3Et]CN$ (152.23 mg, 1.333 mmol). A grey precipitate formed before complete addition. The reaction slurry was left to stir for 24 hr. Precipitate had turned from gray to light green. The light green precipitate was isolated via filtration and washed with 2 x 3 ml H_2O, 3 x 3 mL of MeOH, and 3 x 3 mL of Et_2O, and dried under vacuum at room temperature (yield: 31.79 mg).

Results and Discussion

Synthesis. The synthesis of tetraalkylammonium cation containing Mn(II) PBAs differ from PB and the majority of other PBAs in their synthesis. Rather than using discrete molecular building blocks, i.e. hexacyanometalates and solvated transition metal ions, this new class of PBAs uses cyanide salts with Mn(II) salts to form the PBAs. It has been shown that reactions of spherical tetraalkylammonium cyanide salts of the formula $[NR_4]CN$, where R = Me or Et, with Mn(II) salts (e.g. $MnCl_2$ or $Mn(O_2CCH_3)_2$) in either aqueous or nonaqueous

media has resulted in PBAs of unique and anomalous structure. It is reasonable to assume that using a nonspherical ammonium cation would lead to new PBA structures containing new bonding motifs. The synthesis resulting in **1** yielded a powder of lime-green color, the synthesis of **2** resulted in a golden powder, and **3** was a light green solid. **1** and **2** are anomalous, as previously reported PBAs in this family yield products of green and varying shades of teal color. These compounds discolor and decompose when exposed to ambient atmosphere. The air-sensitive nature of these compounds requires that all handling be done in a N_2 atmosphere.

Infrared spectroscopy. The ν_{CN} and ν_{OH}, absorptions of compounds **1**-**3** are summarized in Table 3.1. The IR spectra of lime-green (**1**) (Figure 3.1) exhibits a strong, sharp ν_{CN} absorption at 2049 cm^{-1} and a slightly less intense sharp peak at 2075 cm^{-1}. Two weak, broad peaks appear at 2095 and 2141cm^{-1}. These peak locations are in accord with a previously synthesized compound that

Table 3.1 IR, ν_{CN} and ν_{OH}, absorptions and colors of $[NMe_3Et]_3Mn_5(CN)_{13}\cdot xH_2O$ (1), $[NMe_3Et]_5Mn_9(CN)_{23}\cdot xMeOH$ (2), and $[NMe_3Et]_2Mn_3(CN)_8\cdot xMeOH$ (3).

	1	**2**	**3**
Color	Lime green	Gold	Light Green
ν_{CN} (cm^{-1})[a]	2049(s), 2075(m), 2095(w), 2141(w)	2014(sh), 2061(s), 2133(br), 2147(w)	2050(sh), 2060(s), 2134(br)
ν_{OH} (cm^{-1})[a]	3628(s)	—	—

a) Sample was analyzied as a pressed KBr pellet. Relative intensities are included as (s) strong, (m) medium, (w) weak, and (sh) shoulder.

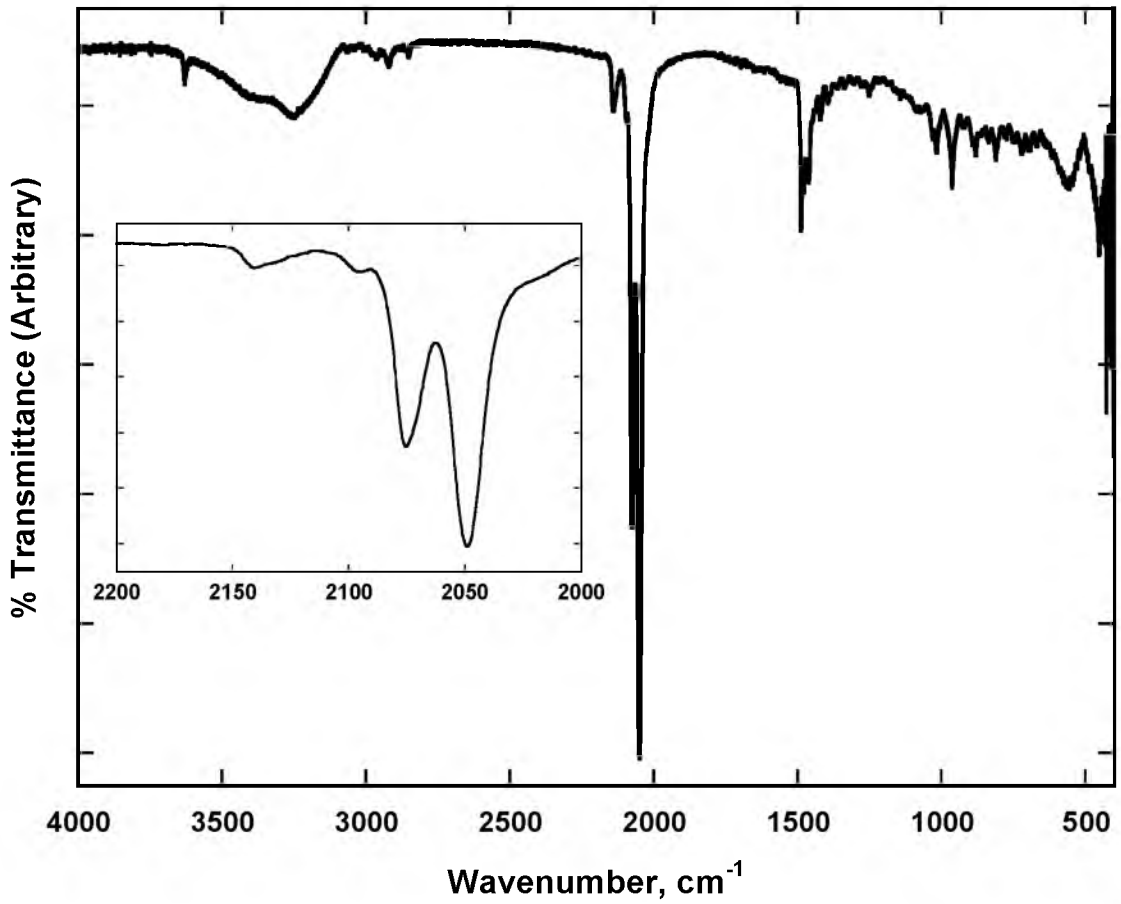

Figure 3.1 IR spectra of $[NMe_3Et]_3Mn_5(CN)_{13}\bullet XH_2O$ (**1**) in KBr.

has a sharp ν_{CN} absorption at 2050 cm^{-1} and a shoulder at 2075 cm^{-1} with weaker ν_{CN} absorptions at 2108 and 2134 cm^{-1}.[2] The strong ν_{CN} absorptions are in agreement, but the weaker ν_{CN} absorptions are shifted. The previously reported compound lacked order along the z-axis while **1** did not. The shifting of the weaker ν_{CN} absorptions may be a result of more order along the z-axis. The sharp peak at 3628 cm^{-1} and broad peak at 3256 cm^{-1} are indicative of H_2O solvation.[4] The gold precipitate **2** (Figure 3.2), exhibits a strong peak at 2061 cm^{-1}, a shoulder at 2014 cm^{-1}, a sharp, weak peak at 2147 cm^{-1}, and a weak, broad peak at 2133 cm^{-1}. The IR spectrum for **3** (Figure 3.3) has double ν_{CN} absorption peaks at 2050 and 2063 cm^{-1}. However, the 2050 cm^{-1} peak has a lower intensity and appears as a shoulder. A broad peak at 2134 cm^{-1} is also present.

Thermogravimetric analysis. The thermal properties were analyzed by thermogravimetric analyses coupled with mass spectroscopic analysis (TGA/MS) of the volatized products. Due to the difficult and time-consuming work it takes to determine the structure of the PBAs presented in this work, many of the compound's structures have not been solved. It has been shown in previous work that the thermal decomposition product of PBAs of the $[NR_LR'_{4-L}]_wMn_y(CN)_z \cdot xSolvent$ family, where R and R' = Me or Et, is $Mn(CN)_2$.[2] Also, the mass spectrometry data have shown that the major TGA loss is due to equivalent amounts of tetraalkylammonium cation and cyanide anion. By this analysis, the first mass loss, usually below 150°C, is a result of desolvation. The second mass loss is a loss of $[NR_LR'_{4-L}]CN$. The remaining mass is the thermolysis product

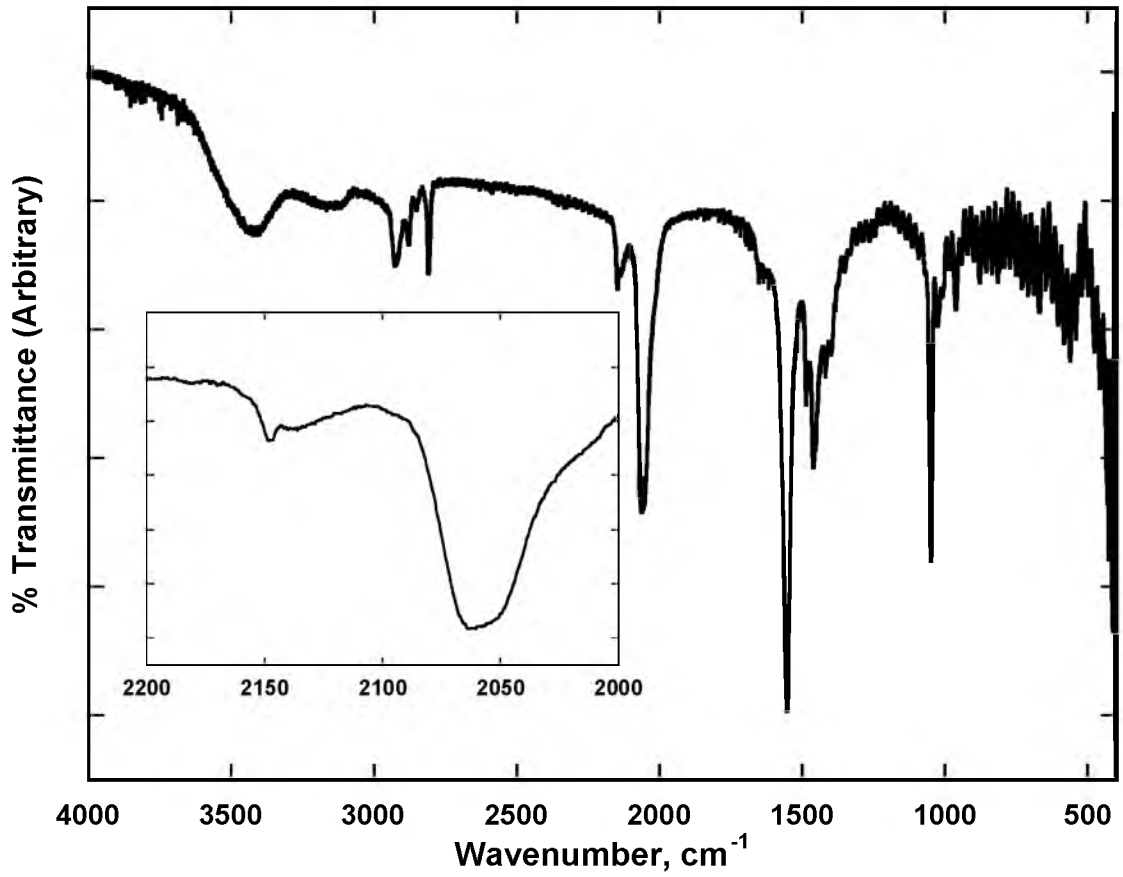

Figure 3.2 IR spectra of $[NMe_3Et]_5Mn_9(CN)_{23}$•xMeOH (**2**) in KBr.

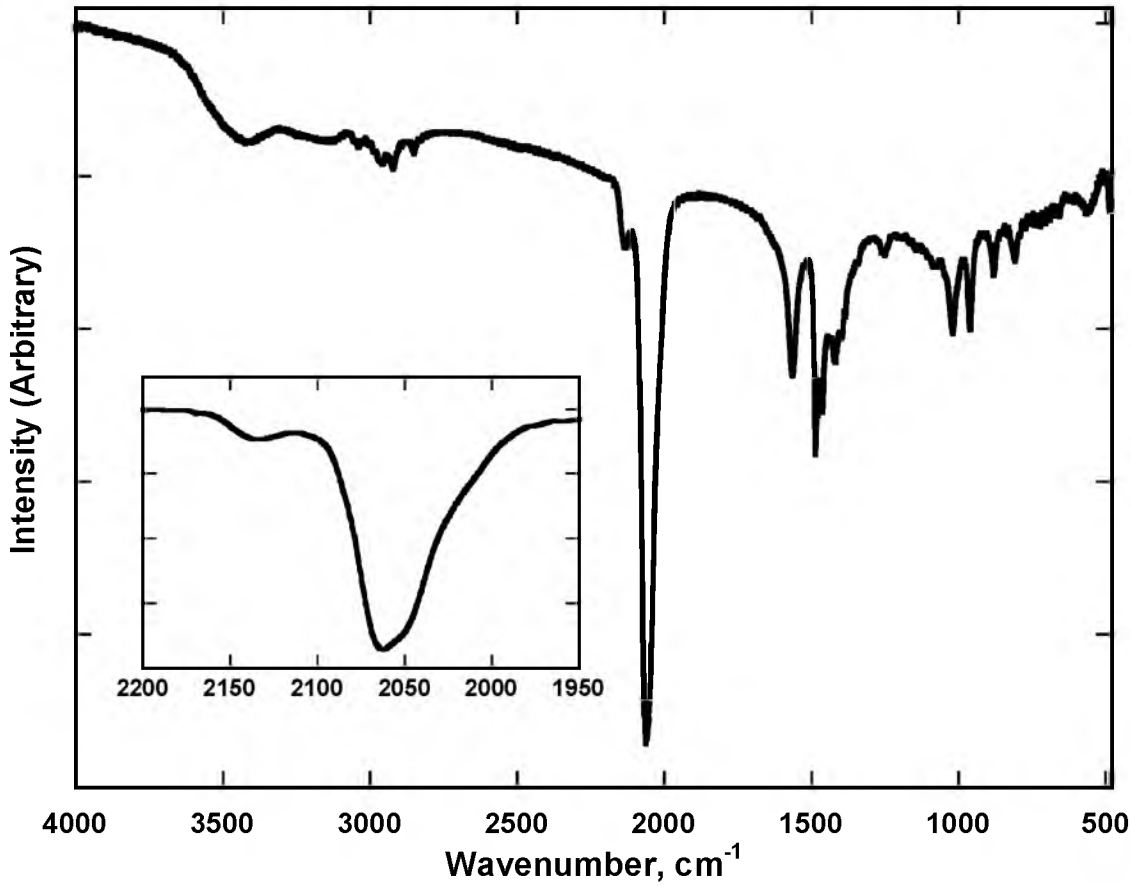

Figure 3.3 IR spectra of $[NMe_3Et]_2Mn_3(CN)_8 \cdot xMeOH$ (**3**) in KBr.

$Mn(CN)_2$. Using the mass percentage ratio, the lowest whole number ratio of $Mn(CN)_2$ to $[NR_LR'_{4-L}]CN$ can be determined. From this ratio, the molecular formula, including solvent, can be determined. The molecular formulas presented in this work that do not have an accompanying structure via PXRD analysis were determined by this TGA method.

Thermolysis of **1,** Figure 3.4, shows a 0.70% mass loss ending at ~140 ^oC. This loss was followed by a 38.37% mass loss. Best fit analysis indicates that this corresponds to the loss of 0.37 equivalents of H_2O followed by the loss of 3 equiv of $[NMe_3Et]CN$.

The analysis of **2,** Figure 3.5, shows a mass loss of 2.76% and 36.36% with onset temperatures of ~30 and ~190 ^oC, respectively. These losses correspond to an initial loss of 1.25 equiv of MeOH followed by a loss of 5 equiv of $[NMe_3Et]CN$. The analysis of **3**, Figure 3.6, shows a 3.13% loss followed by a 39.52% loss with onsets at ~55 K and ~200 K, respectively. These losses correspond to the desolvation of MeOH followed by the decomposition and loss of $[NMe_3Et]CN$.

Structure. Due to the formation of fine particulates during the synthesis of **1**, no single crystals suitable for crystal X-ray diffraction were obtained. The structure of **1** was solved by the refinement of synchrotron PXRD. At the time this chapter was written, refinements of the final structure were still ongoing. What will be described are the structural features that will not change through the final refinement process.

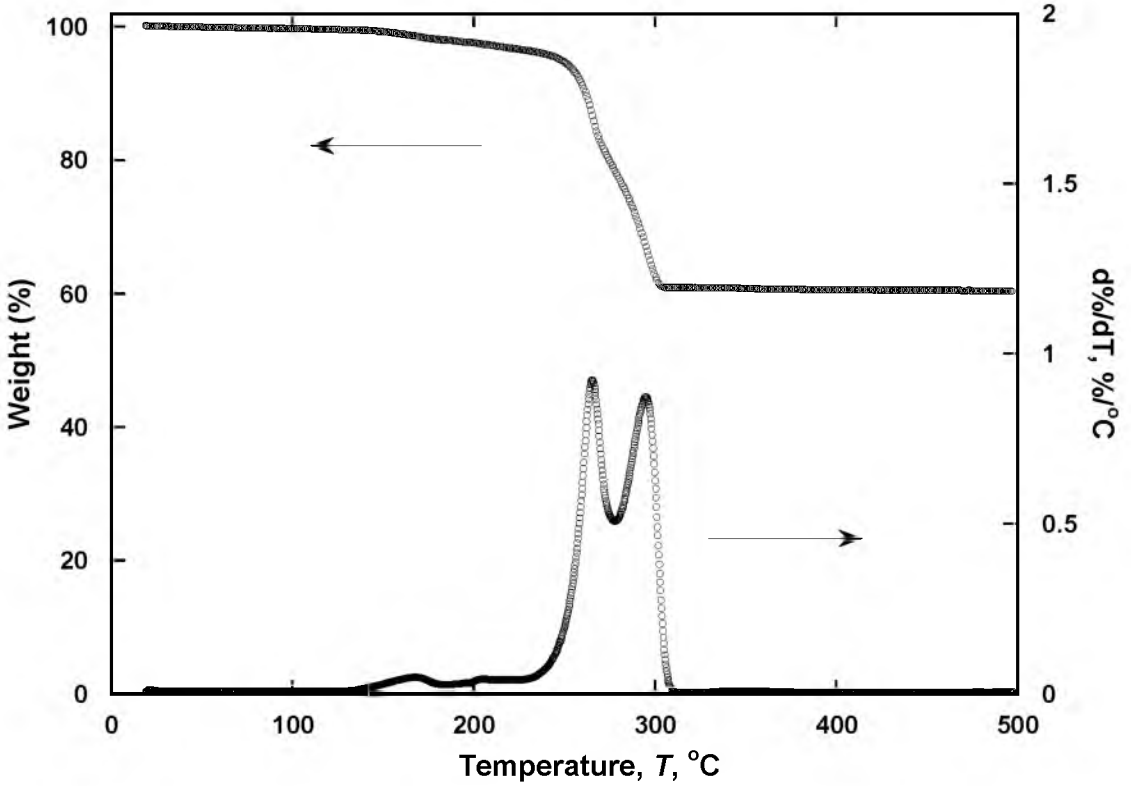

Figure 3.4 TGA trace of $[NMe_3Et]_3Mn_5(CN)_{13}•xH_2O$ (**1**) at a heating rate of 1 °C/min.

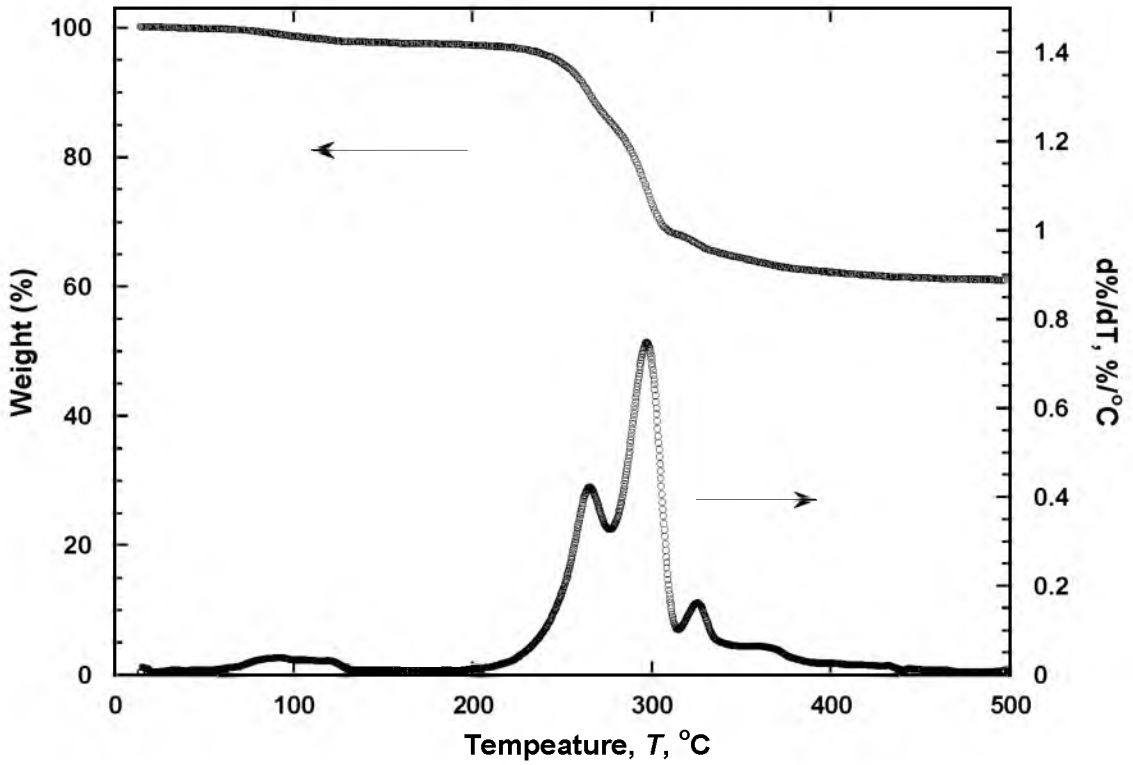

Figure 3.5 TGA trace of $[NMe_3Et]_5Mn_9(CN)_{23}$•xMeOH (**2**) at a heating rate of 1 °C/min.

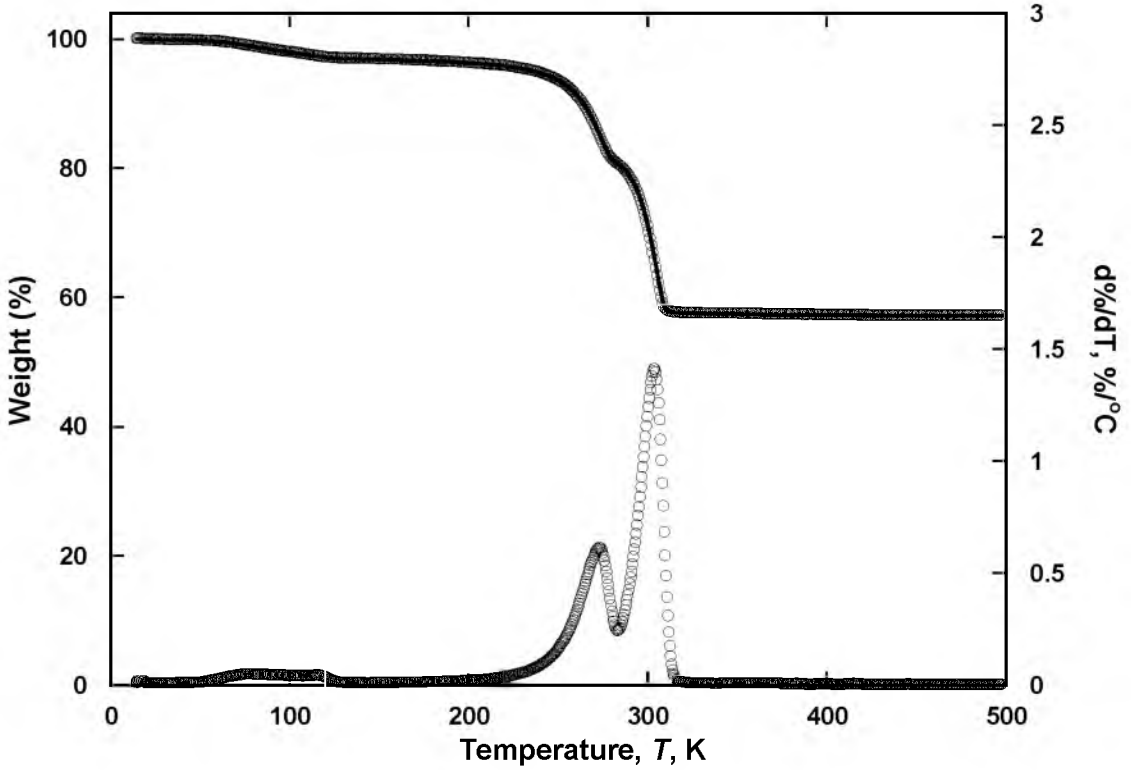

Figure 3.6 TGA trace of $[NMe_3Et]_2Mn_3(CN)_8 \cdot xMeOH$ (**3**) at a heating rate of 1 °C/min.

The structure of 1 is composed of three different Mn(II) sites, one being trigonal bipyramidal, another square pyramidal, and the final site being the expected octahedral geometry. The unit description can be described by taking six Mn(II) sites (Figure 3.7) bridged by cyanide ligands. Mn_1, Mn_3, Mn_4, and Mn are either of square pyramidal or octahedral geometry. Within a layer, the square pyramidal Mn(II) sites will alternate direction in a trigonal ring. The trigonal rings within the layer are composed of Mn_1, Mn_3, Mn_4, and Mn_6 sites. Mn_2 and Mn_5 are of trigonal pyramidal geometry. Mn_2 and Mn_5 sites are always located at the center of three pentagonal rings.

The structure of **1** is similar to a PBA synthesized via the same synthetic route but using $[NMe_4]^+$ instead of $[NMe_3Et]^+$.[2] Both structures have layers composed of three pentagonal rings and one trigonal ring interconnected at trigonal bipyramidal and octahedral/square pyramidal sites (Figure 3.7). Each layer is the same as the layer above and below. While the motif of three pentagonal rings and one trigonal ring is not common, it has been reported for β-U_3O_8.[5] The layers in **1** are interconnected by two bonding motifs (Figure 3.8): 1) the trigonal bipyramidal Mn(II) sites are bonded axially to a trigonal bipyramidal Mn(II) site in the layers above and below, creating extended bonding along the z-axis and 2) an octahedral Mn(II) site is capped by a square pyramidal Mn(II) site in the layers above and below. Between each of the 3-layer capped groups, there is a missing bond before the next 3-layer capped group. As a result of the these 3-layer capped groups forming the vertices of the triangular channels, the

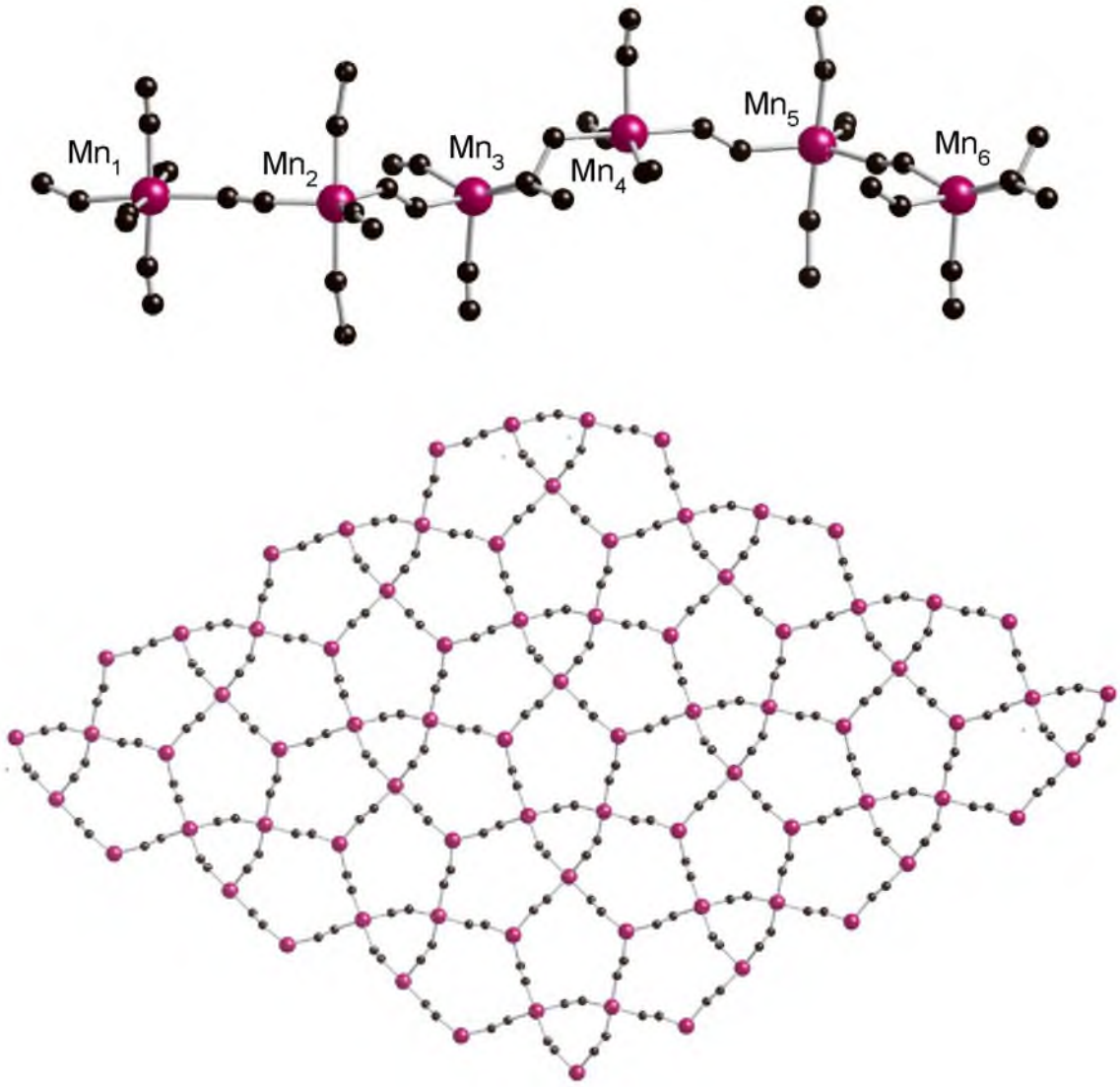

Figure 3.7 (Top) View looking at three Mn(II) sites that repeat through layer. (Bottom) View of a single layer looking down the z-axis. For clarity, the highly disordered $[NMe_3Et]^+$ cations that reside in the vacant sites have been omitted. [cite Peter Stephens]

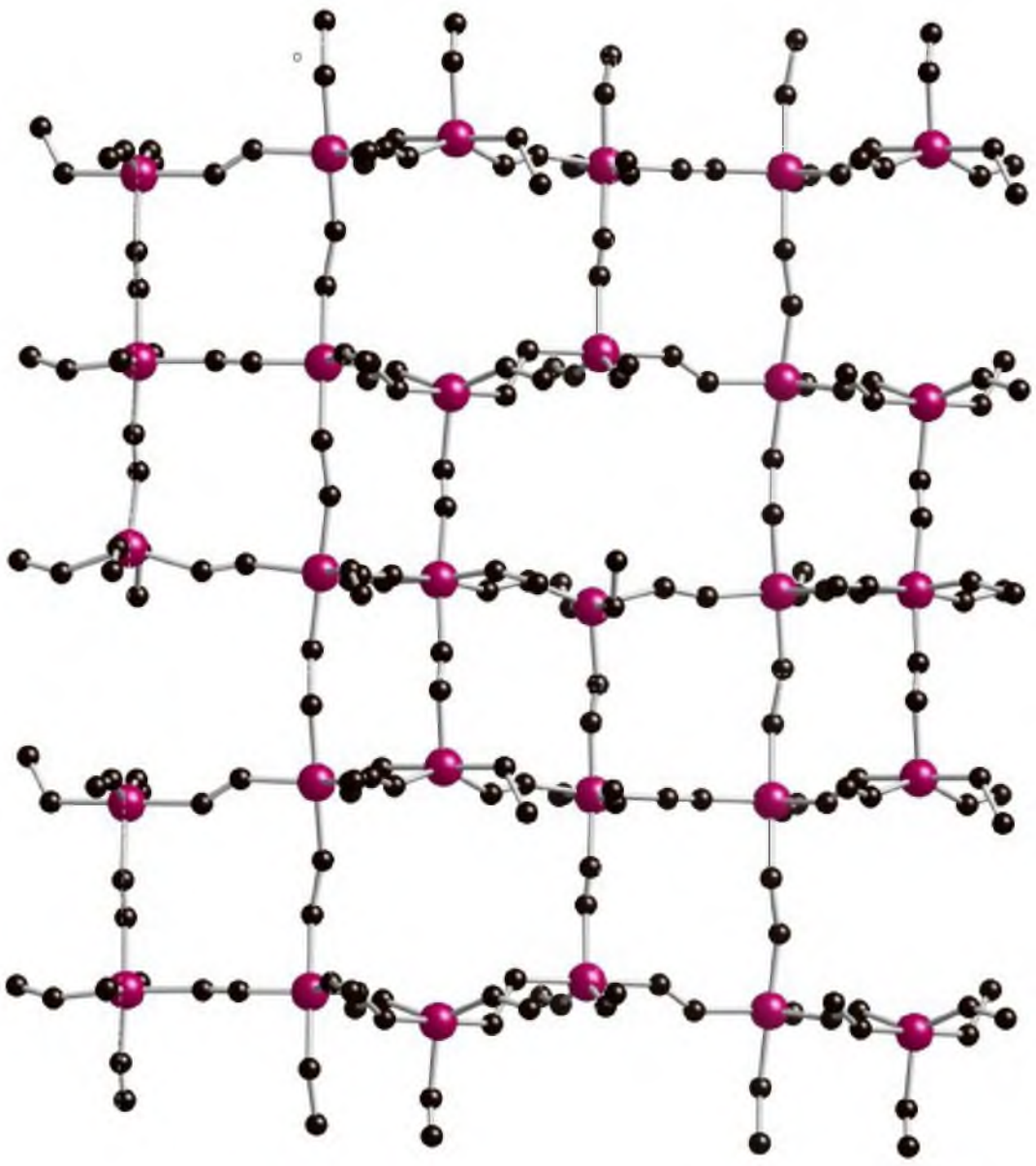

Figure 3.8 A view of 5 layers cut along the z-axis. Interconnectivity between layers is made through 2 connectivies: 1) the trigonal bypyramidal Mn(II) sites are connected axially along the z-axis and 2) the octahedral Mn(II) site is capped by a square pyramidal Mn(II) site in the layers above and below. For clarity, the highly disordered $[NMe_3Et]^+$ cations that reside in the vacant sites have been omitted.

missing bond is in a spiral formation as one goes from layer to layer down the triangular channels.

Magnetic Properties

$[NMe_3Et]_3Mn_5(CN)_{13}•xH_2O$ (1). **1** has a room temperature χT value of 17.96 emuK/mol (Figure 3.9). Tracing the χT(T) data from room temperature to lower temperatures shows a slightly decreasing χT until ~100 K. Below this point, the χT drops rapidly towards zero. The χ^{-1}(T) data for **1** are linear above 50 K. Using the Curie-Weiss expression, $\chi \propto (T - \theta)$-1, to fit the χ^{-1}(T) data above 50 K yielded a θ value of -43 K. The negative θ value is indicative of antiferromagnetic coupling within the bulk material. Using the determined θ value, the χT(T) data were fit over the range of 100 < T <300 K, the measured data can be fit with the Curie-Weiss multinuclear fit equation to yield a system with 0.45 low-spin Mn(II) (S = 1/2) and 4.55 high-spin Mn(II) (S = 5/2).

Analysis of the χ(T) data for **1** (Figure 3.10) as temperature increases shows an increasing susceptibility until it sharply peaks at 17 K and then decreases to a finite susceptibility at higher temperatures. The shape of χ(T), along with the magnitude, is indicative of a polycrystalline material that orders antiferromagnetically.[6]

The temperature at which the maxima in the χ(T) plot occurs has been used to indicate the ordering temperature for antiferromagnetic materials. The temperature is referred to as the Néel temperature, T_N.[6-9] However, Fisher reports that the temperature corresponding to the maxima in the χ(T) occurs above the actual T_c.[10,11] According to Fisher,[12,13] the T_c can reliably be

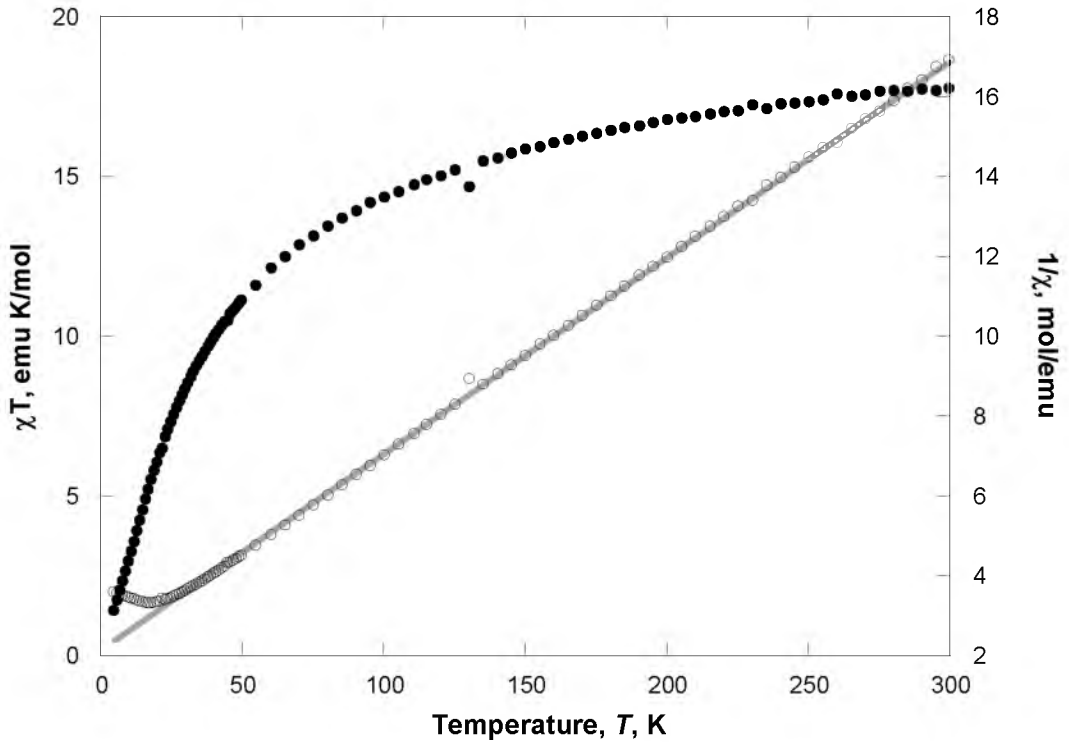

Figure 3.9 χT(T) (●) and 1/χ(T) (○) plots of $[NMe_3Et]_3Mn_5(CN)_{13}$•$0.37H_2O$ (**1**) in a 1000 Oe applied field. A fit to the 1/χ(T) plot using the Curie-Weiss equation is shown as a solid gray line.

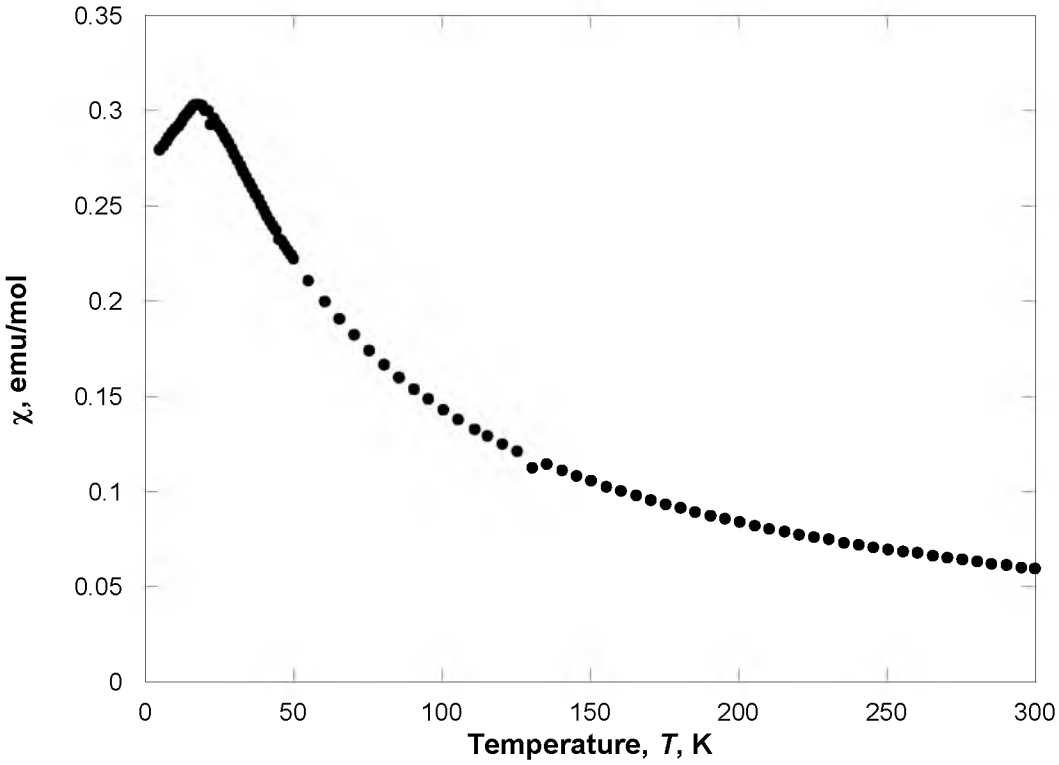

Figure 3.10 χ(T) (●) plot for $[NMe_3Et]_3Mn_5(CN)_{13}\bullet 0.37H_2O$ (**1**) in a 1000 Oe applied field.

method has been used to determine the T_c of antiferromagnetically ordering materials. The d(χT)/dT data for **1** (Figure 3.11) do not have a definite peak, but can be estimated at 14 K. The T_C from the d(χT)/dT data is significantly lower than the peak in the χ(T) data. Through the 5 Oe M_{ZFC}(T) and M_{FC}(T) magnetizations (Figure 3.12) of **1**, the bifurcation temperature, T_b, of 30 K was determined. Beyond the T_b, M_{ZFC}(T) and M_{FC}(T) magnetization measures yield little useful information about **1**. It is worth mentioning that each data set has an unexpected slope change at ~23 K. This behavior has been observed in a PBA synthesized through a similar route.[2]

The ac susceptibility for **1** (Figure 3.13) shows a peak in the χ'(T), but no peak in the χ''(T) data. The presence of the peak in the χ'(T) at 17 K coupled with no peak in the χ''(T) data is a good indicator that **1** has an antiferromagnetic ground state. The field-dependent magnetization, M(H), does not reach saturation below 9 T for **1** at 2 K (Figure 3.14). At 9 T, the magnetization for **1** is 28,730 emuOe/mol. The M(H) does not display any hysteretic behavior for **1**. Magnetic properties are summarized in Table 3.2.

$[NMe_3Et]_5Mn_9(CN)_{23}$•xMeOH (2). The room temperature χT value for **2** cannot be determined due to a jump in the data at ~225 K and an increasing χT(T) value at room temperature (Figure 3.15). The χT(T) from room temperature to cooler temperatures shows a slightly decreasing χT until ~220 K where a sudden drop in χT is observed. Below the 220 K point, the χT data

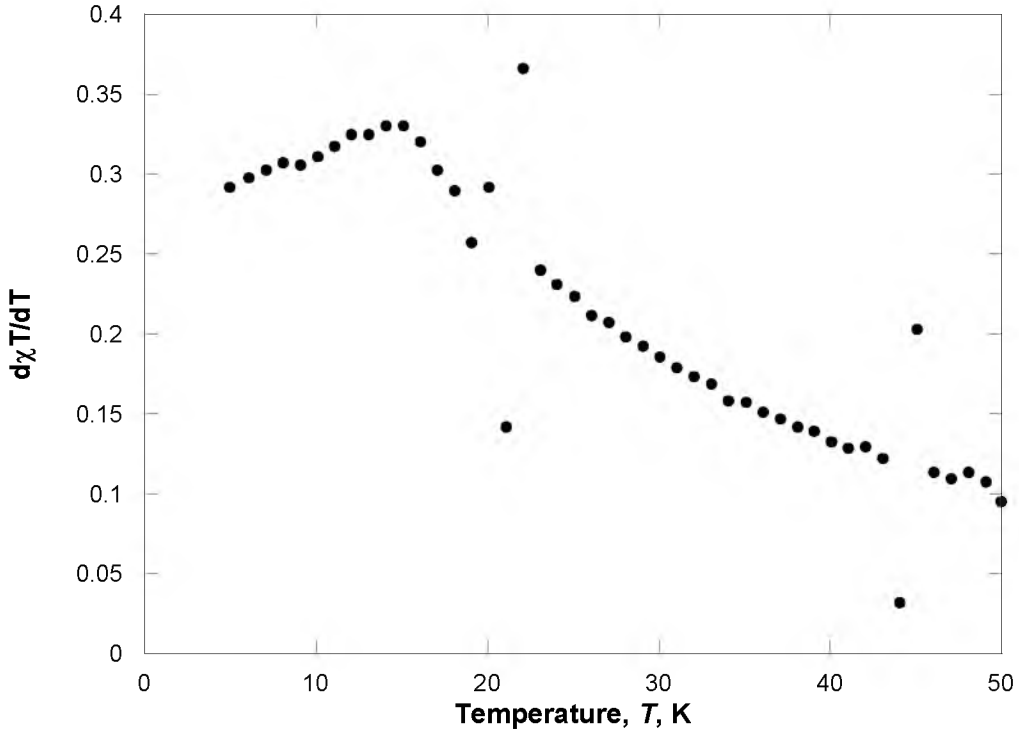

Figure 3.11 dχT/dT (●) plot for $[NMe_3Et]_3Mn_5(CN)_{13}$•$0.37H_2O$ (**1**) in a 1000 Oe applied field.

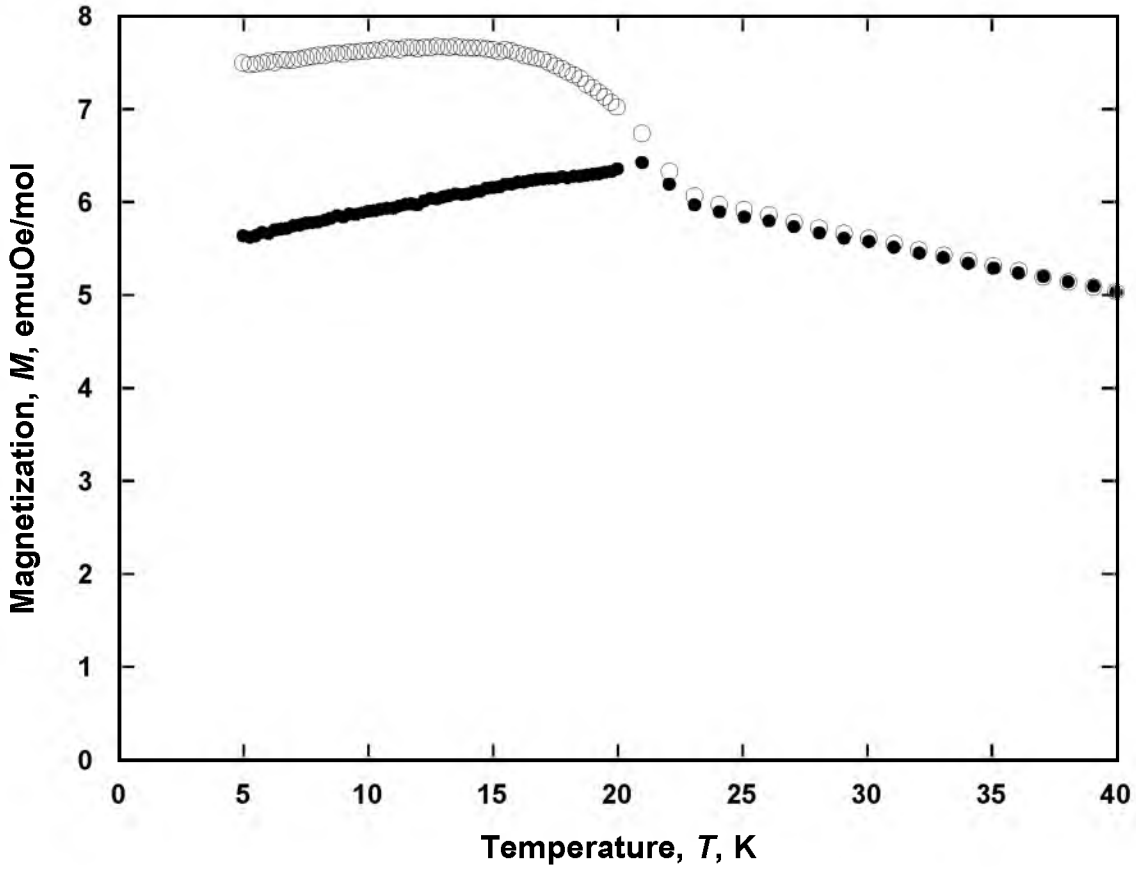

Figure 3.12 10 Oe $M_{FC}(T)$ (●) and $M_{ZFC}(T)$ (○) data for $[NMe_3Et]_3Mn_5(CN)_{13}•0.37H_2O$ (**1**).

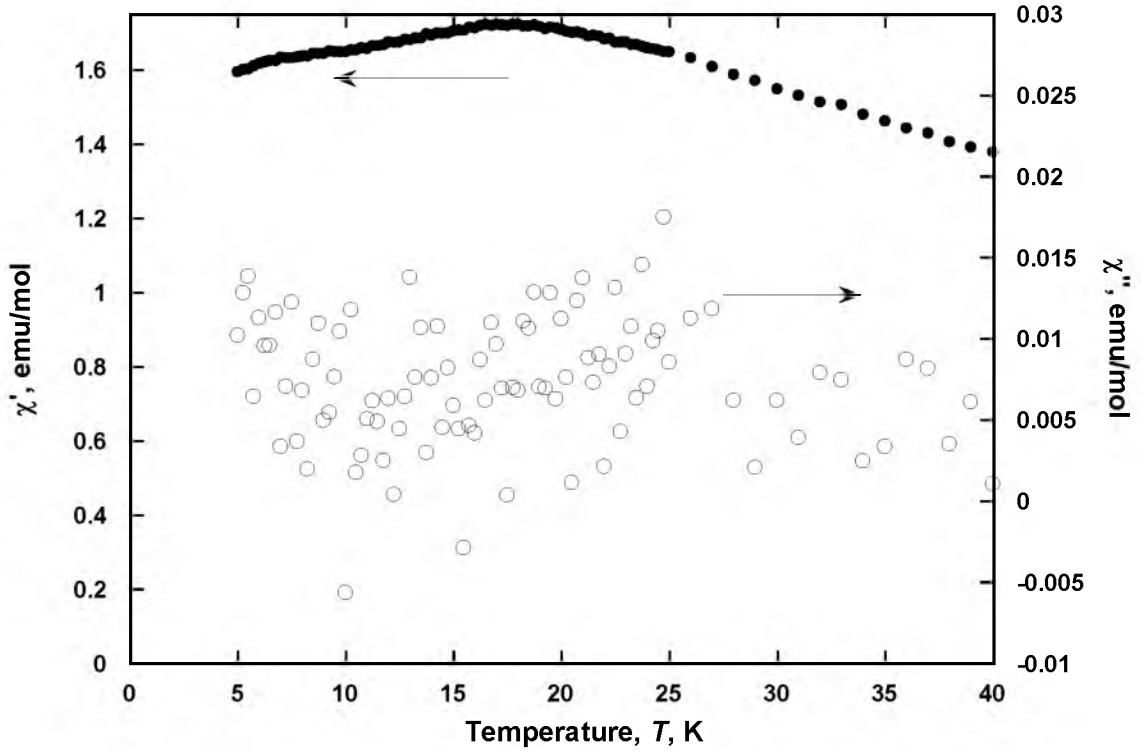

Figure 3.13 Observed in-phase, χ'(T) (●), and out-of-phase, χ''(T) (○), ac susceptibilities at 1000 Hz for $[NMe_3Et]_3Mn_5(CN)_{13}\bullet 0.37H_2O$ (**1**).

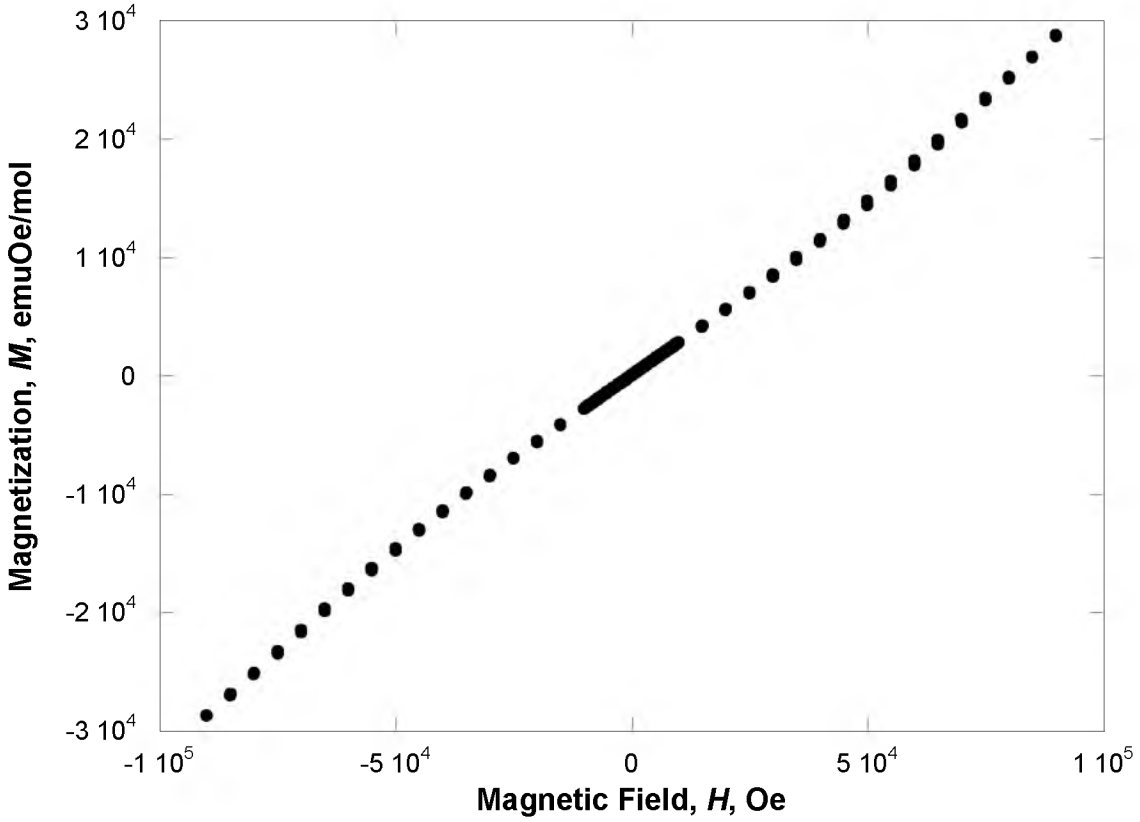

Figure 3.14 Magnetic hysteresis, M(H), of $[NMe_3Et]_3Mn_5(CN)_{13}\bullet 0.37H_2O$ (**1**) at 2 K.

Table 3.2 Summary of the magnetic properties of magnetically pure-phased compounds **1**- **3**.

	1	**2**	**3**
$\chi_{obs}T$, emuK/mol (300K)	17.56	33.9[a]	10.1
$\chi_{calc}T$, emuk/mol (spin-only)	21.875	39.380	9.125
θ, K [Curie-Weiss; $\chi \propto (T - \theta)^{-1}$]	-37.5	-60	-5
M, emuOe/mol (5K, 90 kOe)	28,730	46,598	23,137
Mr, emuOe/mol	—	—	3150
T_b, K (ZFC/FC)	30	25	18.2
H_{cr}, Oe (2K)	—	—	1300
T_c, K [$M_r(T) \rightarrow 0$]	—	—	17.5
T_c, K [$M_{ZFC}(T) \rightarrow 0$]	—	—	26.25
T_c, K [χ_{max}]	17	13	19.1
T_c, K [$d\chi T/dT]_{max}$	14	15	—
T_c, K [$\chi'(T)_{max}$] (1000 Hz)	17	12.8	—
Magnetic Ordering	AF	AF	Ferri

a) Due to jump in the data, this value may not reflect the true value for the bulk material.

resume a slight decreasing trend until ~100 K where the χT drops rapidly towards zero. The $\chi^{-1}(T)$ data for **2** are linear over the range of 50 < T < 220 K and again between 220 < T < 300 K. The Curie-Weiss expression was used to fit the $\chi^{-1}(T)$ data, yielding a θ value of -76 K for the 50 < T < 220 K range and a θ value of -125 K for the 220 < T < 300 K range. The negative θ value in both cases is indicative of mid to strong antiferromagnetic coupling within the bulk material. The $\chi T(T)$ data below 220 K can be fit using 9 hs Mn(II) (Figure 3.15). The data above 220 K cannot be fit due to all of the Mn(II) centers already being hs. The cause of the jump in data is still under investigation.

Analysis of the $\chi(T)$ data for **2** (Figure 3.16) as temperature increases shows an increasing susceptibility until it sharply peaks at 13 K and then decreases to a finite susceptibility at higher temperatures. Like **1,** The magnitude

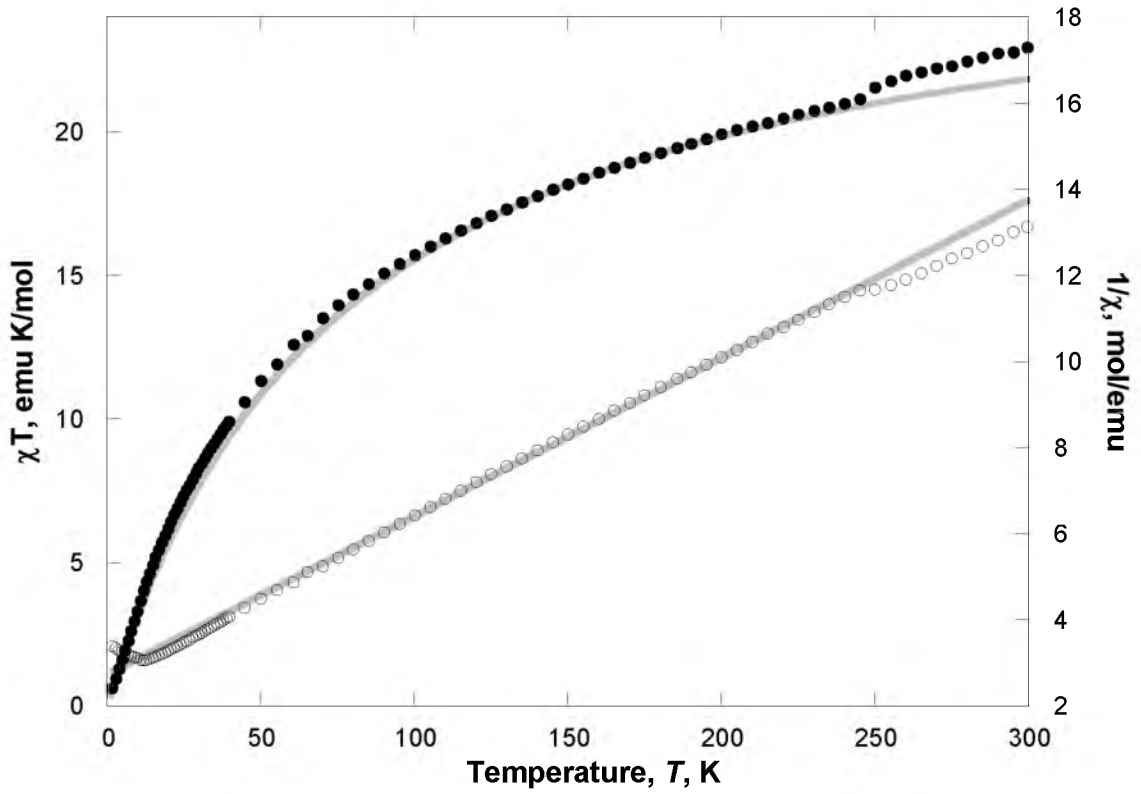

Figure 3.15 χT(T) (●) and 1/χ(T) (○) plots of $[NMe_3Et]_5Mn_9(CN)_{23}$•1.25MeOH (**2**) in a 1000 Oe applied field. A fit to the χT(T) and 1/χ(T) plot using the Curie-Weiss equation is shown as a solid gray line.

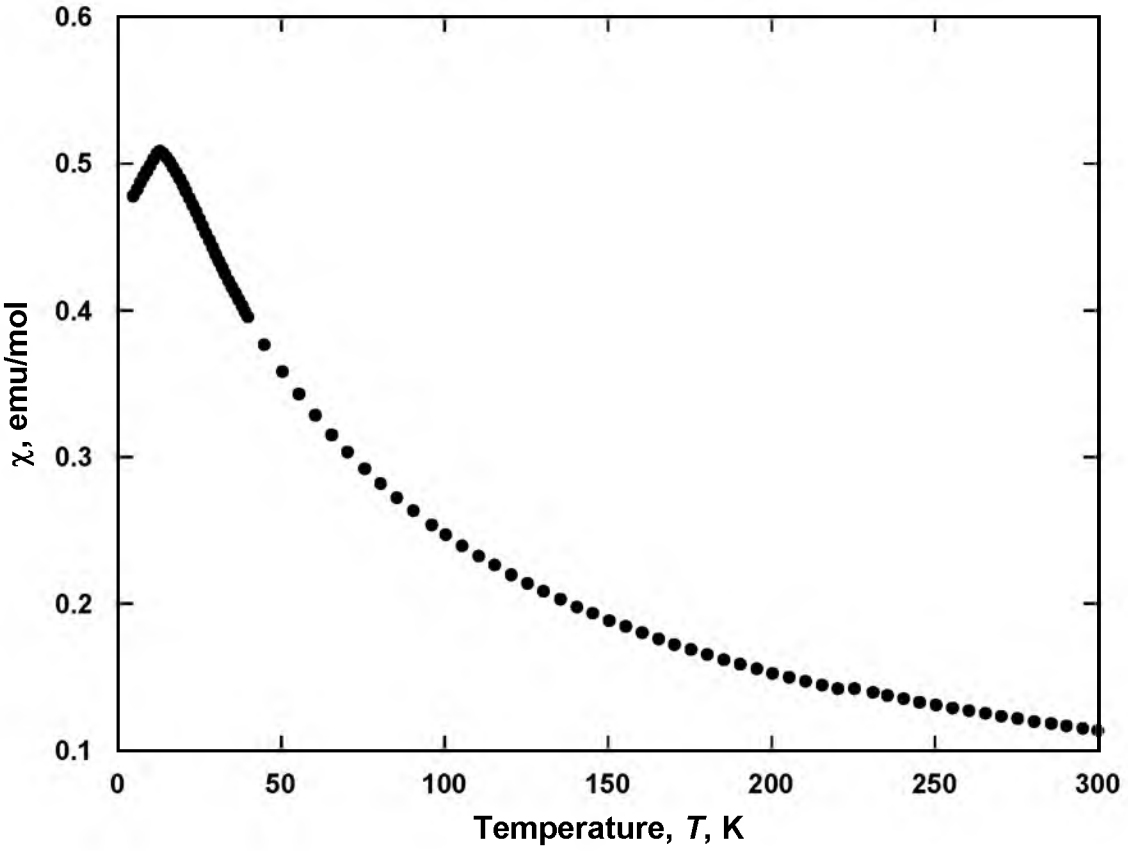

Figure 3.16 χ(T) (●) plot for $[NMe_3Et]_5Mn_9(CN)_{23}$•1.25MeOH (**2**) in a 1000 Oe applied field.

and shape of χ(T) is indicative of a polycrystalline material that orders antiferromagnetically.[6] Through the 5 Oe M_{ZFC}(T) and M_{FC}(T) magnetizations (Figure 3.17) of **2**, the bifurcation temperature, T_b, of 25 K was determined. Due to ordering as an antiferromagnet, beyond the T_b, no relevant information can be gleaned from the M_{ZFC}(T) and M_{FC}(T) magnetization measurements. Due to **2** displaying antiferromagnetic behavior, the Fisher method, defining the Tc as the temperature at which the dχT/dT reaches a maximum, was used. The d(χT)/dT data for **2** (Figure 3.18) do not have a definite peak, but can be estimated at 14K. The T_C from the d(χT)/dT data is significantly lower than the peak in the χ(T) data.

The ac susceptibility for **2** (Figure 3.19) shows a peak in the χ'(T), but no peak in the noisy χ''(T) data. The presence of the peak in the χ'(T) at 12.8 K coupled with no peak in the χ''(T) data indicates that **2** has an antiferromagnetic ground state. The field-dependent magnetization, M(H), does not reach saturation below 9 T for **2** at 5 K (Figure 3.20). At 9 T, the magnetization for **2** is 46,598 emuOe/mol. **2** does not display any magnetic hysteresis. Magnetic properties are summarized in Table 3.2.

$[NMe_3Et]_2Mn_3(CN)_8$•xMeOH (3). Compound **3** has a room temperature χT value of 10.1 emuK/mol 9 (Figure 3.21) that is higher than the spin-only room temperature χT of 9.125 emuK/mol for a two high-spin Mn(II) (S = 5/2) and one low-spin Mn(II) (S = 1/2) system. As the sample is cooled, the χT value has a slight downward trend until 50 K where the χT value sharply rises until reaching a maximum value of 55.1 emuK/mol at 19.1 K and then sharply dropping off toward

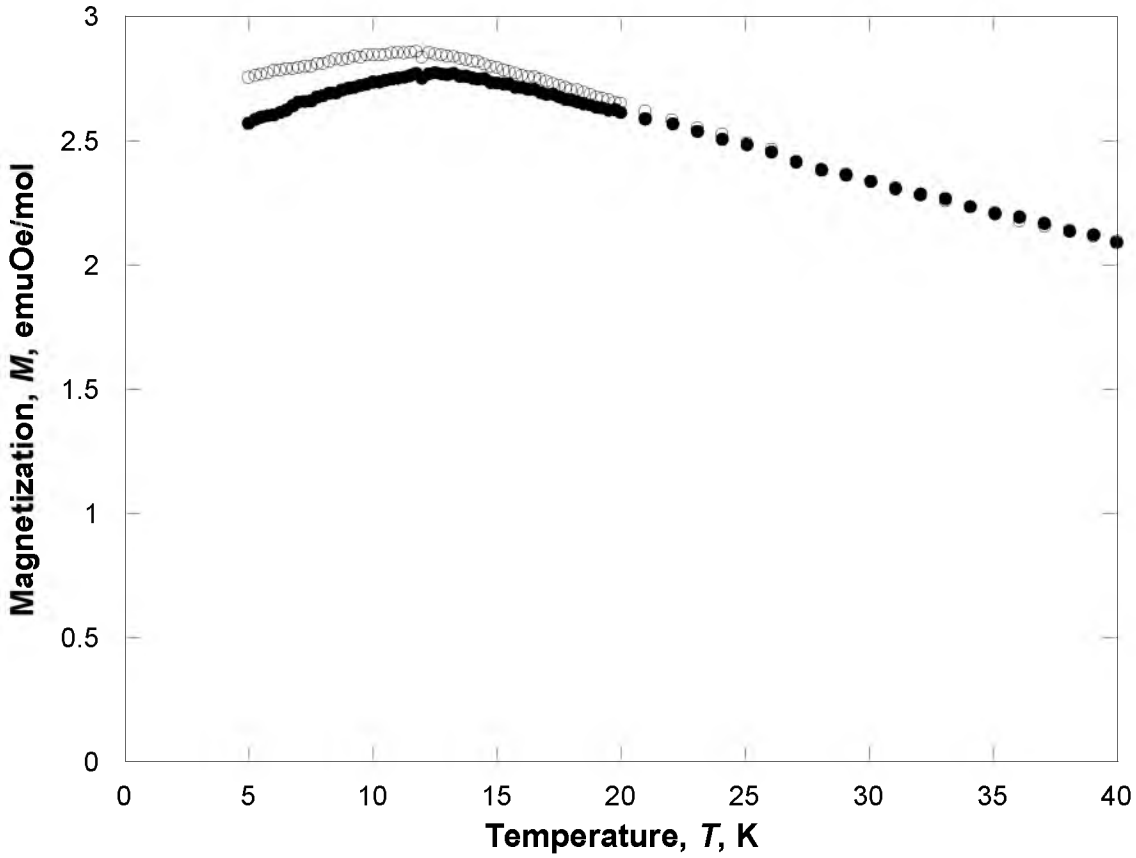

Figure 3.17 5 Oe $M_{FC}(T)$ (●) and $M_{ZFC}(T)$ (○) data for $[NMe_3Et]_5Mn_9(CN)_{23}$•1.25MeOH (**2**).

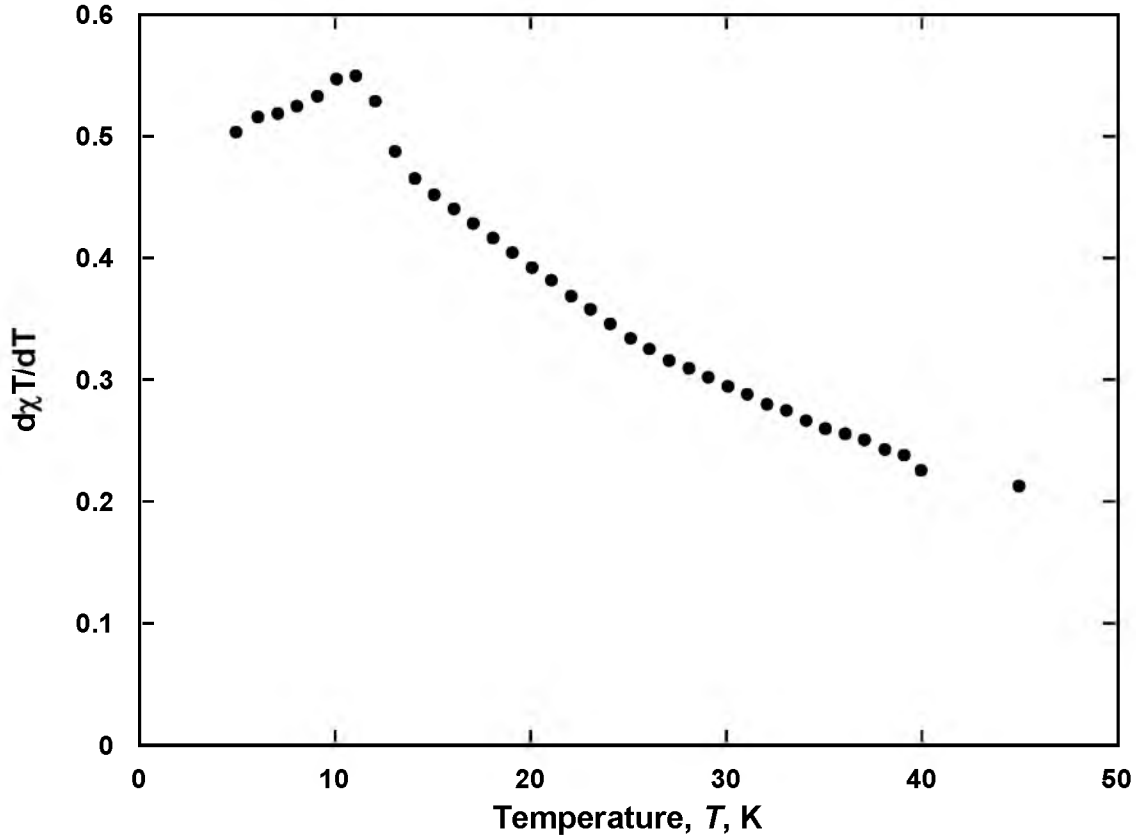

Figure 3.18 d(χT)/dT (●) plot for $[NMe_3Et]_5Mn_9(CN)_{23}$•1.25MeOH (**2**) in a 1000 Oe applied field.

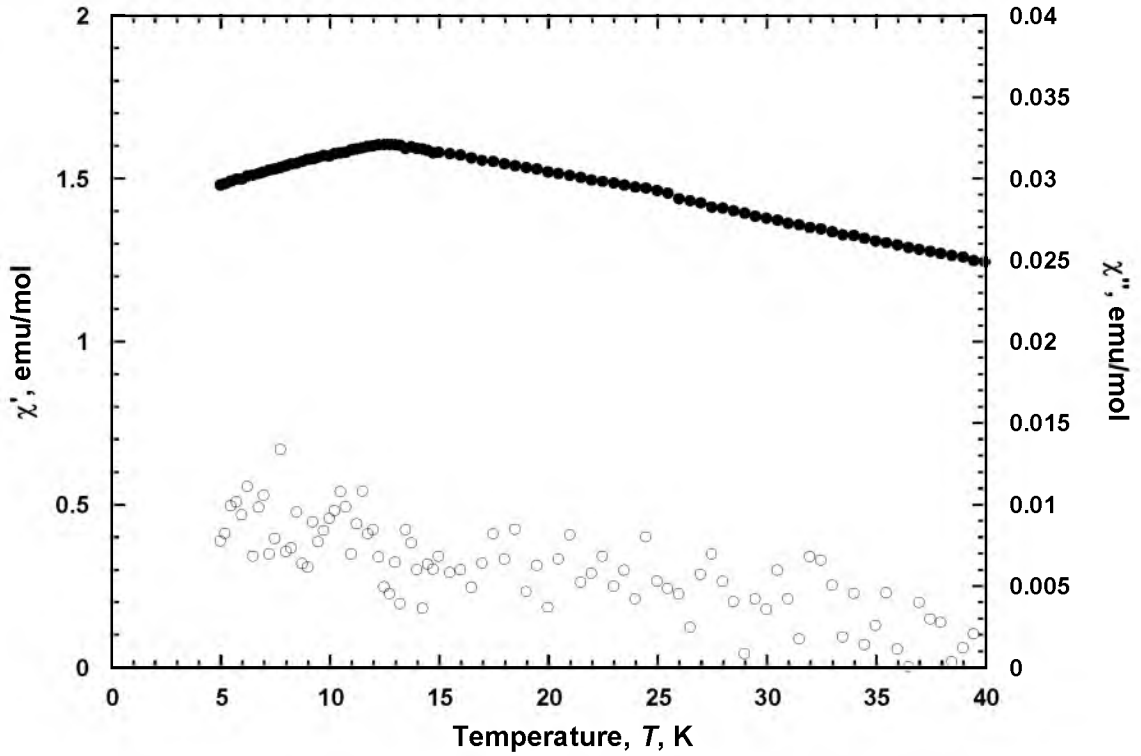

Figure 3.19 Observed in-phase, χ'(T) (●), and out-of-phase, χ''(T) (○), ac susceptibilities at 1000 Hz for $[NMe_3Et]_5Mn_9(CN)_{23}$•1.25MeOH (**2**).

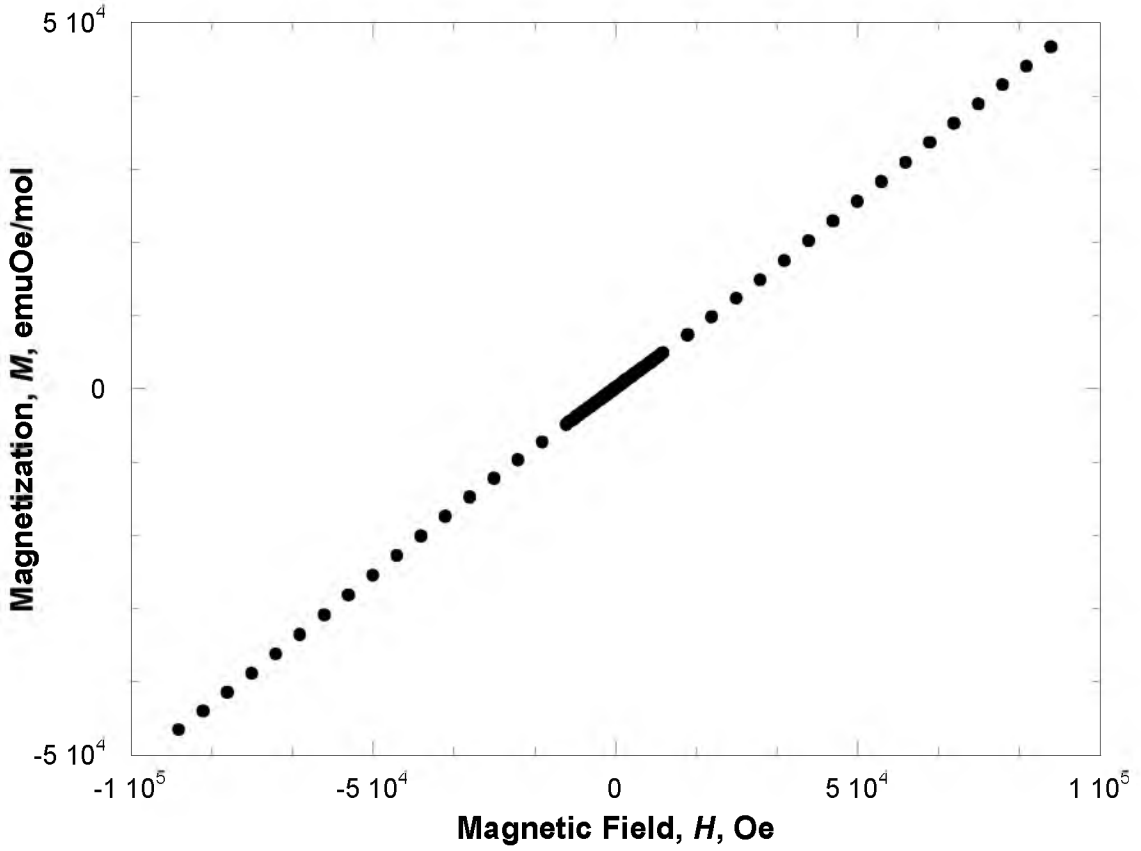

Figure 3.20 Magnetic hysteresis, M(H), of $[NMe_3Et]_5Mn_9(CN)_{23}$•1.25MeOH (**2**) at 5 K.

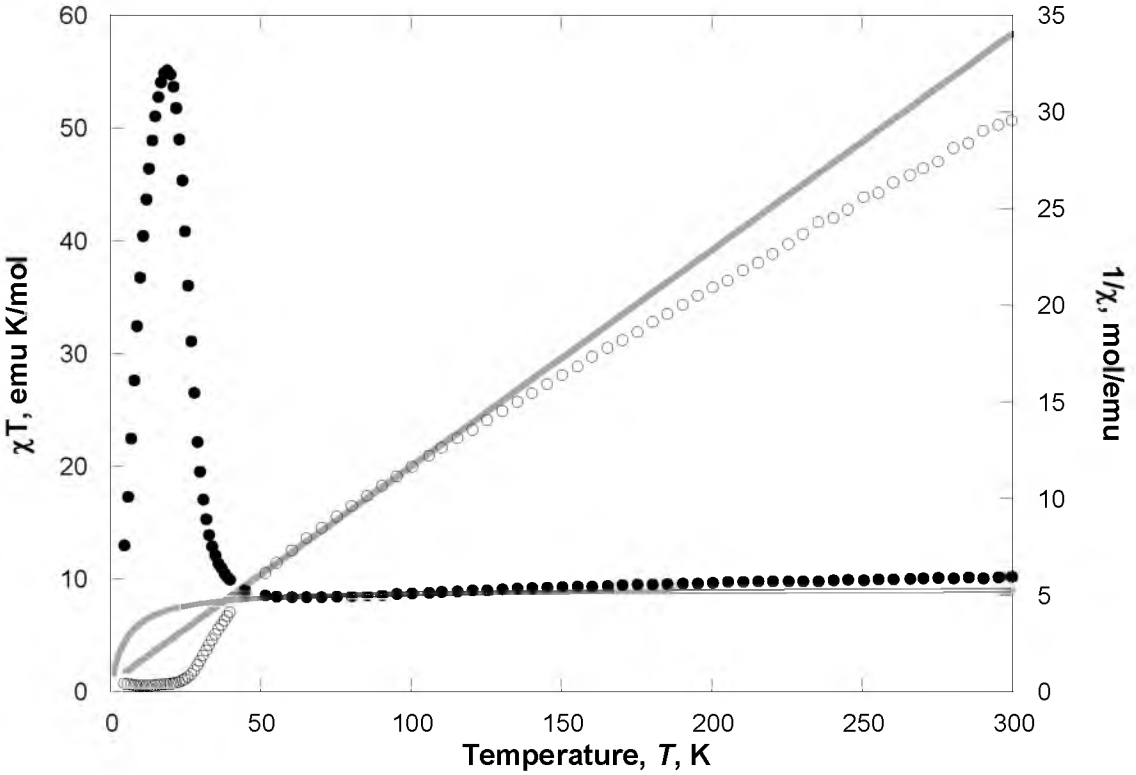

Figure 3.21 χT(T) (●) and 1/χ(T) (○) plots of $[NMe_3Et]_2Mn_3(CN)_8$•0.6MeOH (**3**) in a 1000 Oe applied field. A fit to the χT(T) and 1/χ(T) plot using the Curie-Weiss equation is shown as a solid gray line.

zero. The χ^{-1}(T) data for **3** (Figure 3.21) are linear over the range of 50 < T < 100 K. A θ value of -5 K was found by fitting the χ^{-1}(T) using the Curie-Weiss expression.

Analysis of the χ(T) data for **3** (Figure 3.22) as temperature increases shows an increasing susceptibility until it sharply peaks at 11 K and then rapidly decreases towards zero at higher temperatures. The peak in the χ(T) data is indicative of magnetic ordering. Analysis of the **3** Oe M_{ZFC}(T) and M_{FC}(T) magnetizations (Figure 3.23) of **3** yielded a bifurcation temperature, T_b, of 18.2 K. The M_{rem}(T) magnetization (Figure 3.23) yields a T_c of 17.5 K.

The ac susceptibility for **3** (Figure 3.24) shows a peak in the χ'(T) and in the χ''(T) data. This is indicative of ferri- or ferromagnetic ordering in the compound. Both χ'(T) and χ''(T) show a frequency dependence, ϕ = 0.027.[14] Frequency dependence is indicative of spin-glass behavior and/or disorder/frustration of the spin coupling.[15] As the frequency shifts higher, the peak in the χ'(T) and the onset in the χ''(T) shift to higher temperatures. Spin-glass behavior has been reported for other PBAs and indicates an amorphous and/or significantly disordered material.[16,17] Using the onset in the 1000 Hz χ''(T) data, **3** has a T_c of 22.0 K. This value is larger than the maxima in the 1000 Hz χ''(T) data, 19.2 K, which is in turn larger than the T_b. The field-dependent magnetization, M(H), does not reach saturation below 9T for **3** at 2 K (Figure 3.25). At 9T, the magnetization for **3** is 23,137 emuOe/mol. **3** displays magnetic hysteresis behavior with a coercive field, H_{cr}, of 1300 Oe and a

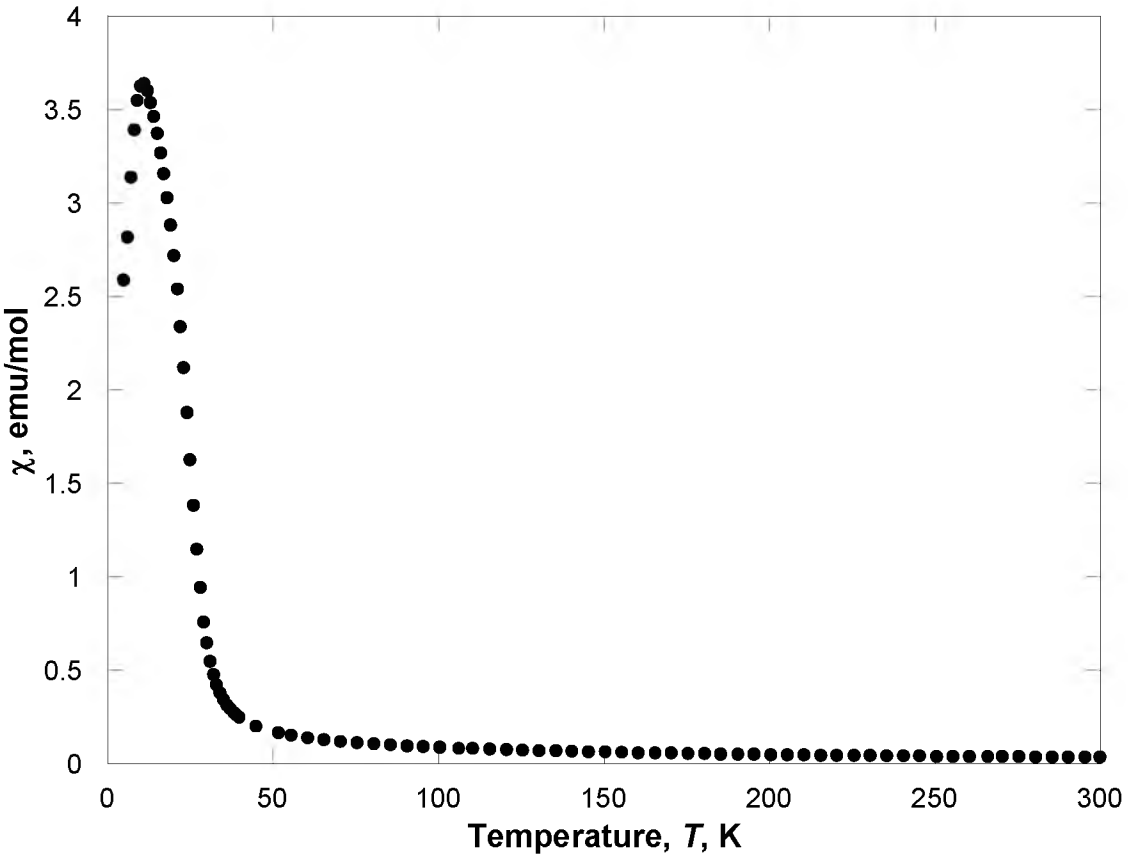

Figure 3.22 χ(T) (●) plot for $[NMe_3Et]_2Mn_3(CN)_8 \cdot 0.6MeOH$ for (**3**) in a 1000 Oe applied field.

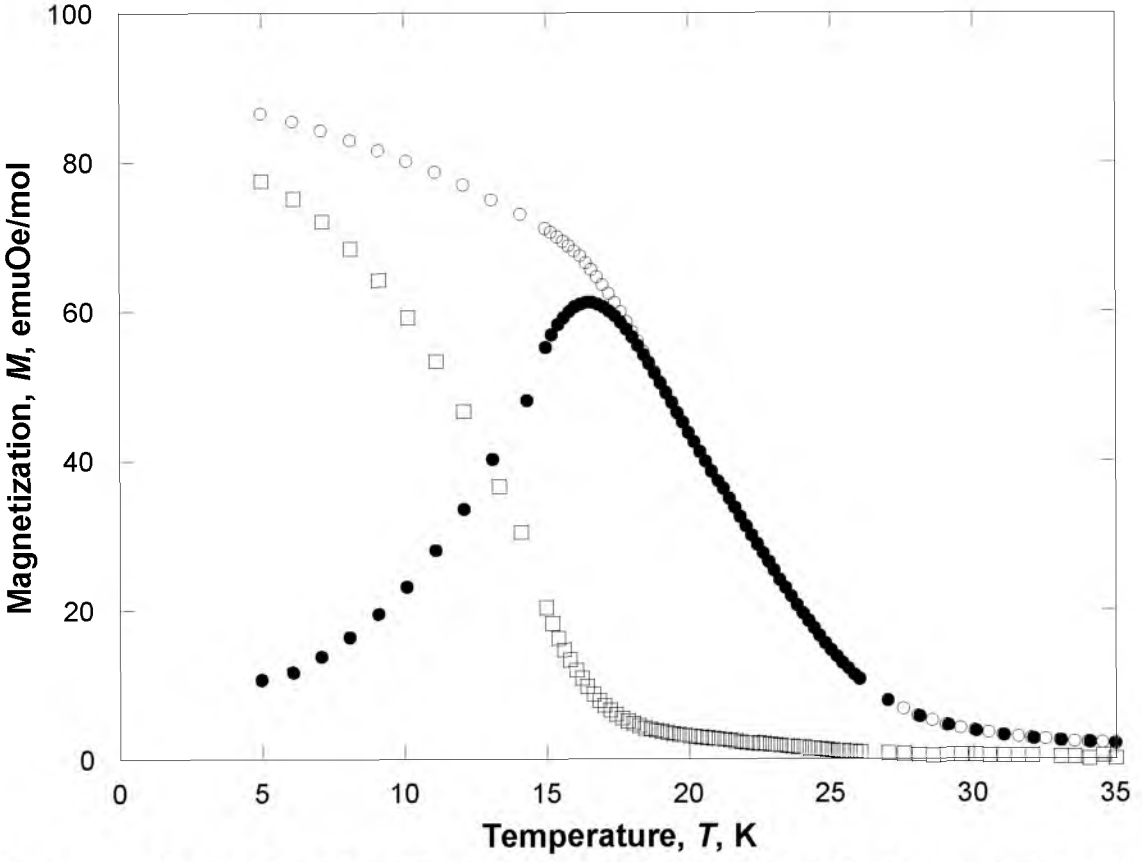

Figure 3.23 5 Oe $M_{ZFC}(T)$ (●), $M_{FC}(T)$ (○), and $M_{rem}(T)$ (□) data for $[NMe_3Et]_2Mn_3(CN)_8 \cdot 0.6MeOH$ for (**3**).

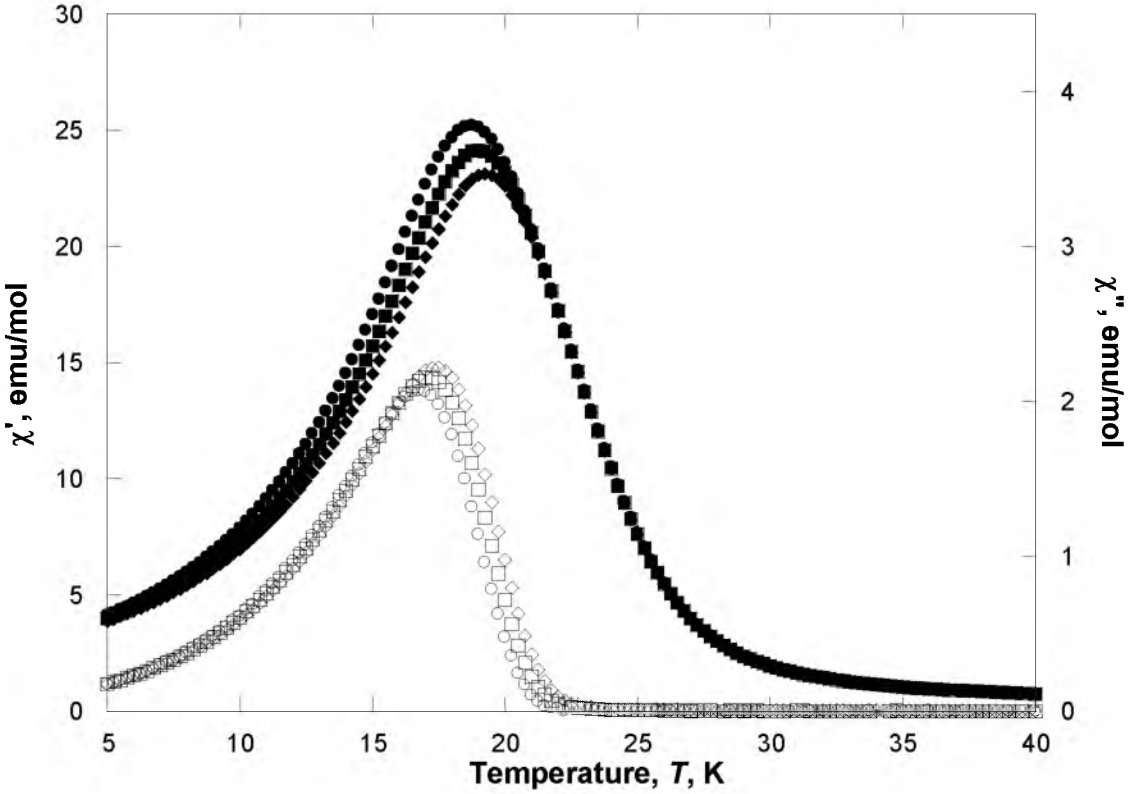

Figure 3.24 Observed in-phase, χ'(T) (filled), and out-of-phase, χ''(T) (open), ac susceptibilities at 100 (●,○), 333 (■,□), and 1000 (♦,◊) Hz for $[NMe_3Et]_2Mn_3(CN)_8 \cdot 0.6MeOH$ (**3**).

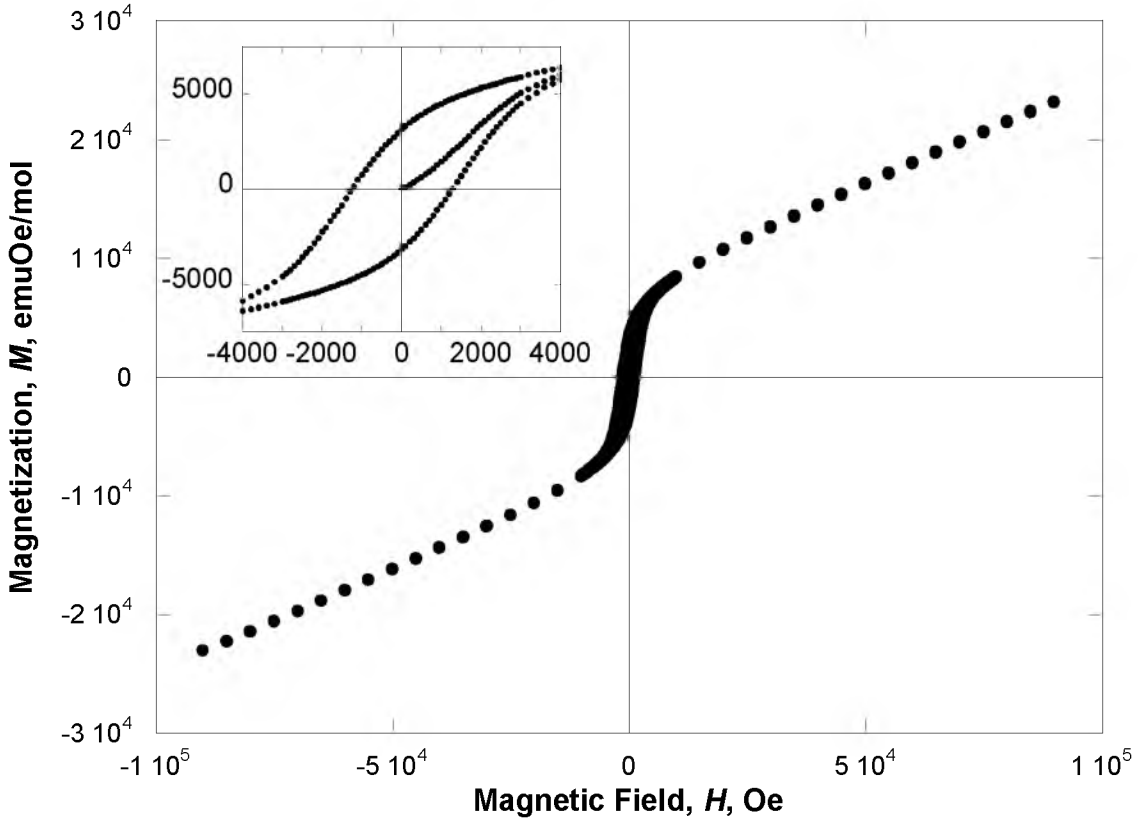

Figure 3.25 Magnetic hysteresis, M(H), of $[NMe_3Et]_2Mn_3(CN)_8 \cdot 0.6MeOH$ (**3**) at 2 K.

remnant magnetization, M_{RM}, of 3150 emuOe/mol. Magnetic properties are summarized in Table 3.2.

Through the course of these investigations, several compounds were isolated that had mixed magnetic phases. One of particular interest is **4**. This compound was the result of washing **1**, a compound synthesized in aqueous solvent, with H_2O. The result is a compound that has changed physical appearance, changed from lime-green to light blue, and magnetic properties. **4** no longer displays antiferromagnetic behavior in the ac measurements. Instead, there appears to be 2 peaks in the χ' and in the χ'' measurements, Figure 3.26, which is indicative of ferri- or ferromagnetic coupling. Due to the mixed nature of**4**, no other analysis can be performed at this time to elucidate structure or bonding motifs.

Compound 5 was an attempt to make a 2-D extended PBA. Instead of a pure compound, the ac measurements revealed 3 peaks at 14, 23, and 27 K that order as a ferrimagnet. It has been the author's intention to isolate a compound that has each of the reported Tc peaks in 5. While 1 has a Tc of 14 K, it orders as an antiferromagnet. The author has been unsuccessful in synthesizing compounds that order as a ferrimagnet and have a measured Tc of 23 or 27 K. It may be that 5 is a mixture of phases such that all 3 magnetic phases are present. Reaction conditions of compounds 1-6 are summarized in Table 3.3.

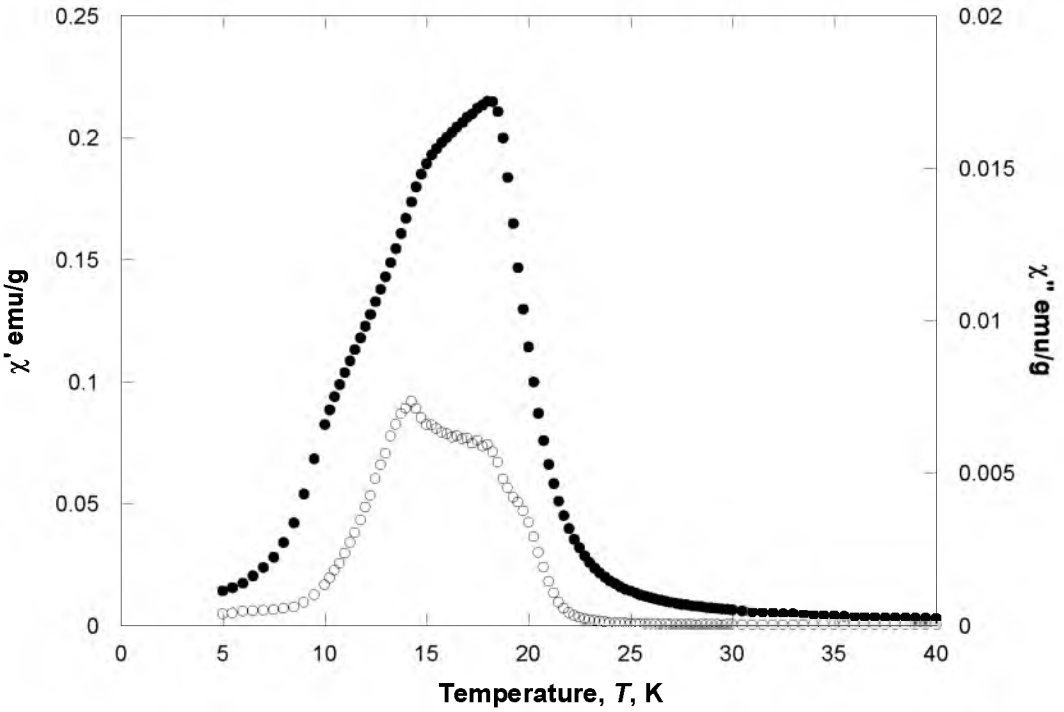

Figure 3.26 Observed in-phase, χ'(T) (●), and out-of-phase, χ''(T) (○), ac susceptibilities at 1000 Hz for **4**.

Table 3.3 Summary of reaction conditions for **1-5.**

	1	**2**	**3**	**4**	**5**
Solvent	H_2O	MeOH	MeOH	H_2O	H_2O
Ratio, CN:Mn	3:1	2:1	5:1	—	1.5:1
M of CN, mol/L	0.625	0.980	0.652	—	1.333
M of Mn, mol/L	0.315	0.131	0.131	—	0.887
Added reactant	Mn	CN	CN	—	CN
Reaction time, hr	24	24	24	18	24
Magnetic purity	Pure	Pure	Pure	Mixed	Mixed

$[NMe_2Et_2]^+$ Class

Synthesis $[NMe_2Et_2]_3Mn_8(CN)_{19}\bullet xH_2O$ (6). A 2 mL aqueous solution of $[NMe_2Et_2]CN$ (362.58 mg, 2.828 mmol) was added drop-wise to a stirring 2 mL aqueous solution of $Mn(O_2CCH_3)_2$ (306.55 mg, 1.772 mmol). A grey precipitate formed that turned yellow and then a dark teal color within minutes. The reaction mixture was stirred for 3 hr. The precipitate was isolated via filtration and washed with water (3 x 3 mL), methanol (3 x 3 mL), and ether (3 x 3 mL), and dried under vacuum at room temperature for 4 hr. (yield: 115.93 mg, 62%). IR (KBr) 3630 (w), 2924 (vw), 2854 (vw), 2072 (s), 2064 (s), 1455 (m), 1017 (w) cm^{-1}. Sample used for magnetic analysis contained 2.4 equivalents of H_2O. A core diamagnetic correction of -302.6×10^{-6} emuK/mol was used.

$[NMe_2Et_2]Mn_3(CN)_7\bullet xMeOH$ (7). A 5 mL methanol solution of $Mn(O_2CCH_3)_2$ (43.19 mg, 0.245 mmol) was added drop-wise to a stirring 3 mL methanol solution of $[NMe_2Et_2]CN$ (104.29 mg, 0.758 mmol). A grey precipitate formed that turned dark green within minutes. The reaction mixture was stirred for 3 hr. The dark green precipitate was isolated via filtration and washed with methanol (3 x 3 mL) and ether (3 x 3 mL), and dried under vacuum at room

temperature for 4 hr (yield: 17.83 mg, 43%). IR (KBr) 3435 (m), 2923 (w), 2852 (w), 2156 (w), 2121 (w), 2062 (s), 1448 (w), 1021 (w) cm^{-1}. Sample used for magnetic analysis contained 2 equiv of MeOH. A core diamagnetic correction of -264.8×10^{-6} emuK/mol was used.

(8). A 1.5 mL aqueous solution of $[NMe_2Et_2]CN$ (305.76 mg, 2.221 mmol) was added drop-wise to a stirring 1 mL aqueous solution of $Mn(O_2CCH_3)_2$ (117.71 mg, 0.680 mmol). A grey precipitate formed that turned bright gold and then a dark forest green color within a minute. The reaction mixture was stirred for 18 hr. The precipitate was isolated via filtration and washed with water (3 x 3 mL), methanol (3 x 3 mL), and ether (3 x 3 mL), and dried under vacuum over P_2O_5 at room temperature for 5 hr. (yield: 87.05 mg).

(9). A 1.5 mL aqueous solution of $[NMe_2Et_2]CN$ (321.13 mg, 2.505 mmol) was added drop-wise to a stirring 1 mL aqueous solution of $Mn(O_2CCH_3)_2$ (55.21 mg, 0.319 mmol). A grey precipitate formed that turned bright gold and then a dark forest green color within minutes. The reaction mixture was stirred for 3 hr. The precipitate was isolated via filtration and washed with water (2 x 3 mL), methanol (2 x 3 mL), and ether (2 x 3 mL), and dried under vacuum at room temperature. IR (KBr)

Results and Discussion

Infrared spectroscopy. The ν_{CN} and ν_{OH}, absorptions of compounds **6** and **7** are summarized in Table 3.4. The IR spectra of **6**, Figure 3.27, shows 2 sharp, intense stretches in the CN region at 2064 and 2072 cm^{-1}. This is

Table 3.4 IR, ν_{CN} and ν_{OH}, absorptions and colors of $[NMe_2Et_2]_3Mn_8(CN)_{19}\bullet xH_2O$ (6) and $[NMe_2Et_2]Mn_3(CN)_7\bullet xMeOH$ (**7**).

	6	**7**
Color	Dark Teal	Gold
ν_{CN} (cm^{-1})[a]	2064(s), 2072(s)	2062(s), 2122(w, br), 2155(w, br)
ν_{OH} (cm^{-1})[a]	3630(s)	3430(br)

a) Sample was analyzed as a pressed KBr pellet. Relative intensities are included as (s) strong, (m) medium, (w) weak, and (sh) shoulder.

representative of 2 different CN environments within the compound. A sharp absorption is observed at 3630 cm^{-1}. This is a characteristic stretch indicating solvation within the compound. Compound **7**, Figure 3.28, has a sharp single CN peak at 2062 cm^{-1} with 2 broad, less intense peaks at 2122 and 2155 cm^{-1}. CN stretches above 2100 cm^{-1} generally indicate an extended 3-D network structure. The broad peak at 3430 cm^{-1} is a result of solvent in the lattice.

Thermogravimetric Analysis

The thermogravimetric analysis of **6**, Figure 3.29, shows a little to no mass loss up to 140 °C. A loss of 3.37% is observed over the range of 140-215 °C. A second loss of 30.00% is observed as the temperature is raised from 215 °C to 400 °C. Above 400 °C, the thermally stable $Mn(CN)_2$ compounds remain. The initial loss is due to desolvation of 2.4 equivalents of H_2O. The second mass loss corresponds to decomposition and loss of 3 equivalents of $[NMe_2Et_2]^+$ and CN^-. The exact mechanism of this loss has yet to be determined. It is obvious that these ions do not leave as a salt. However, the thermally stable $Mn(CN)_2$

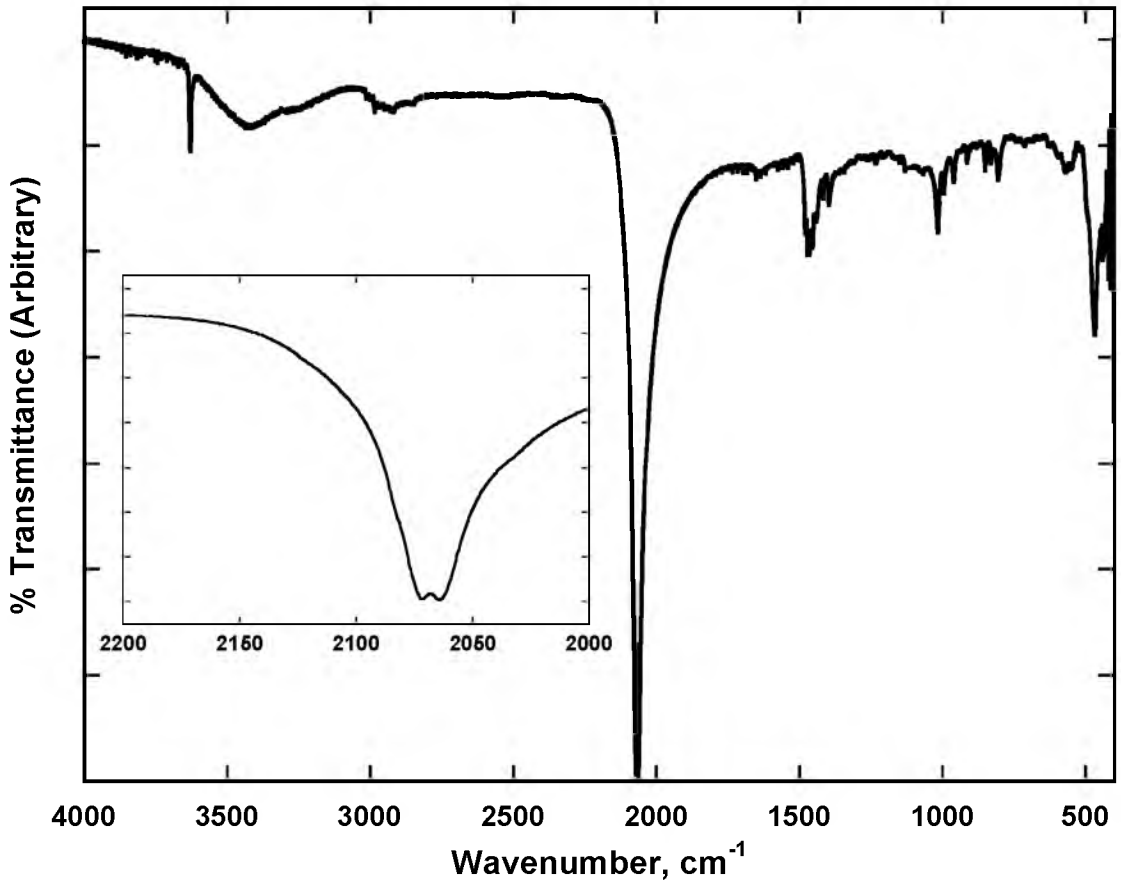

Figure 3.27 IR spectra of $[NMe_2Et_2]_3Mn_8(CN)_{19}\bullet 2.4H_2O$ (**6**) in KBr.

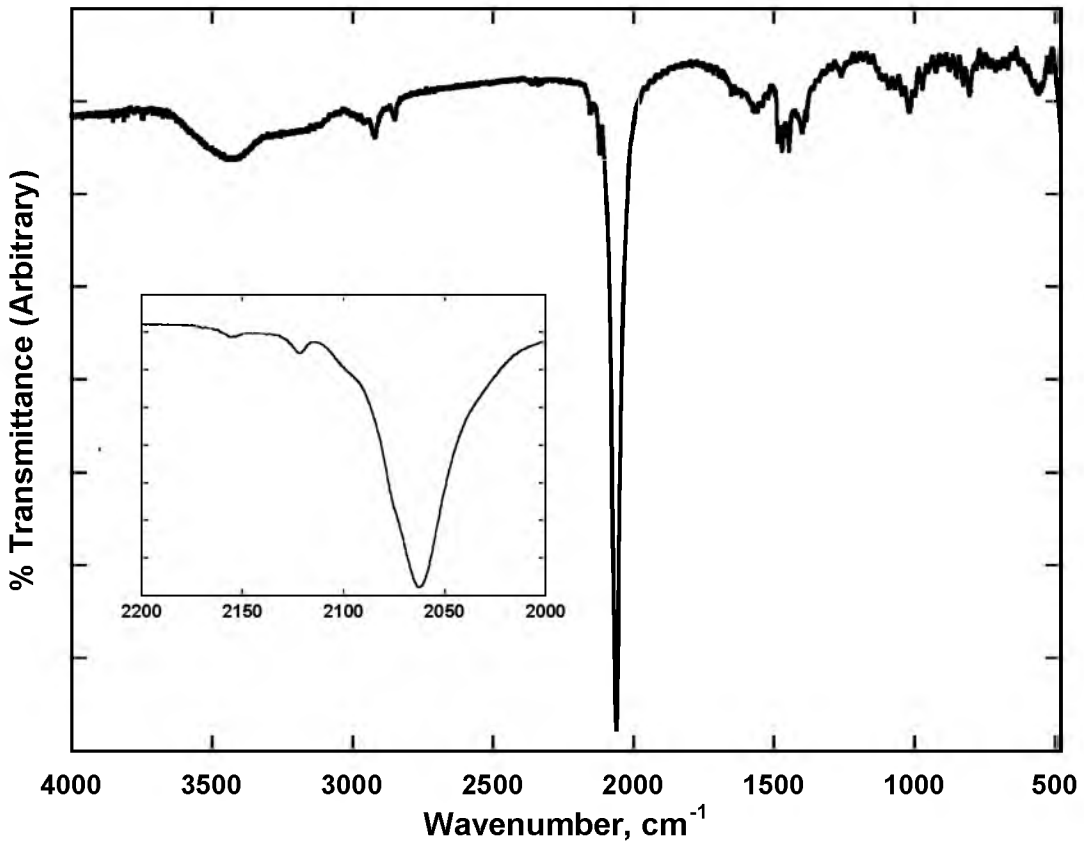

Figure 3.28 IR spectra of $[NMe_2Et_2]Mn_3(CN)_7$•2MeOH (**7**) in KBr.

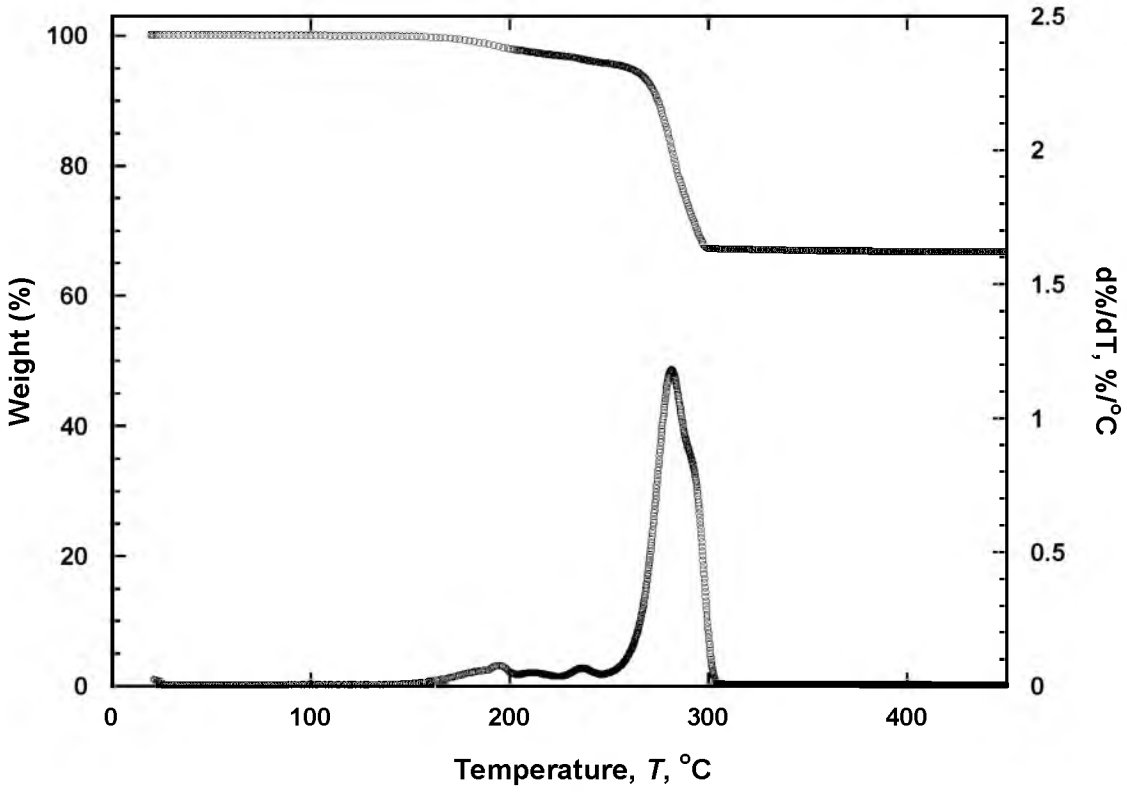

Figure 3.29 TGA trace of $[NMe_2Et_2]_3Mn_8(CN)_{19}\bullet 2.4H_2O$ for (**6**) at a heating rate of 1 °C/min.

compound being formed as a result of this thermolysis indicates that equal amounts of each ion has been lost.

Compound **7**, Figure 3.30, begins to lose MeOH almost immediately and continues solvent loss up to ~200 °C. At 230 °C, a second loss begins and continues to 435 °C. The first loss, loss of solvent, and second loss, loss of equivalent $[NMe_2Et_2]^+$ and CN^-, amount to 7.85% and 52.86% mass loss, respectively.

Magnetic Properties

$[NMe_2Et_2]_3Mn_8(CN)_{19}$•2.4$H_2O$ (6). The χT data for **6**, Figure 3.31, show that this compound has a room temperature χT of 26.9 emuK/mol. This value is in good agreement with the spin-only value of 27.375 emuK/mol for six high-spin, S = 5/2, and two low-spin, S =1/2, Mn(II) atoms. The χT(T) does not change as the temperature is cooled until 155 K, at which point the data rapidly increase until reaching a peak of 505.9 emuK/mol at 13 K. Below 13 K, the χT value rapidly decreases towards zero. The χ^{-1} data, Figure 3.31, have 2 linear portions, 45-115 K and 200-300 K. Using the Curie-Weiss expression, $\chi \propto (T - \theta)^{-1}$, to fit the χ^{-1} data yields a θ value of 28.6 K over 45-115 K and a θ value of -10.6 K over 200-300 K. At lower temperatures, **6** exhibits ferrimagnetic behavior and ordering. As the temperature increases, antiferromagnetic behavior begins to dominate, as shown by the negative θ value at the higher temperatures.

The χ(T) data, Figure 3.32, for **6** show the χ(T) value at 5 K to be 51.7 emuK/mol. The value of χ(T) rapidly decreases towards zero between 5 K and 100 K. At temperatures above 100 K, the value of χ(T) remains zero. Through

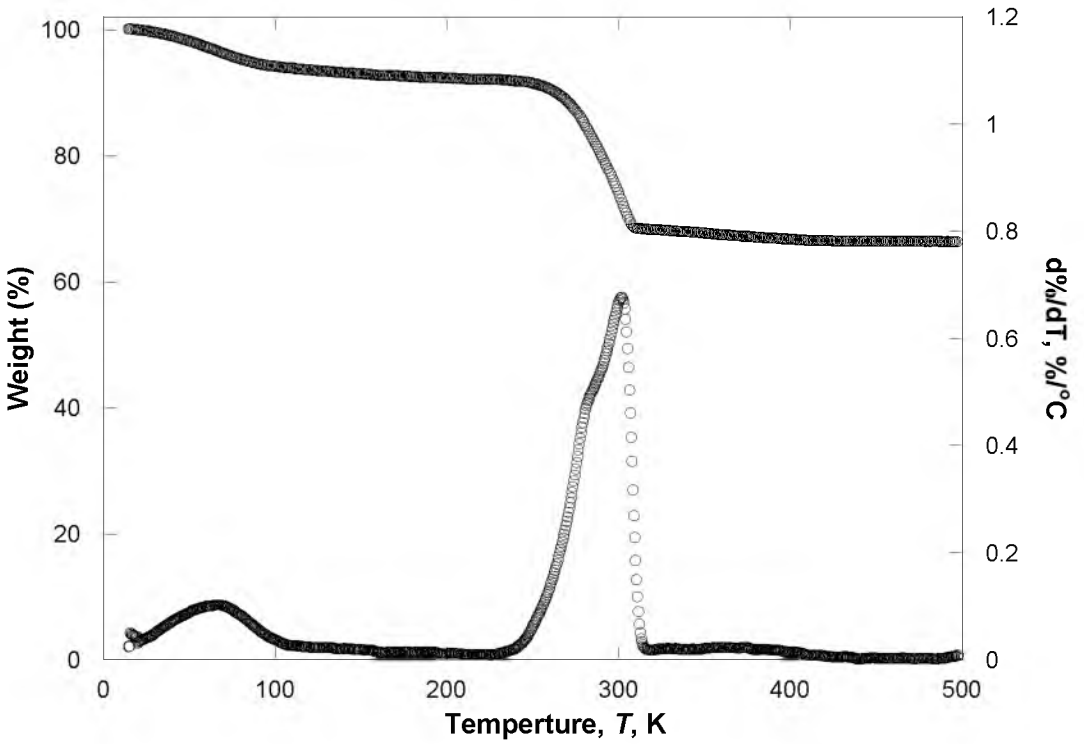

Figure 3.30 TGA trace of $[NMe_2Et_2]Mn_3(CN)_7$•2MeOH for (**7**) at a heating rate of 1 °C/min.

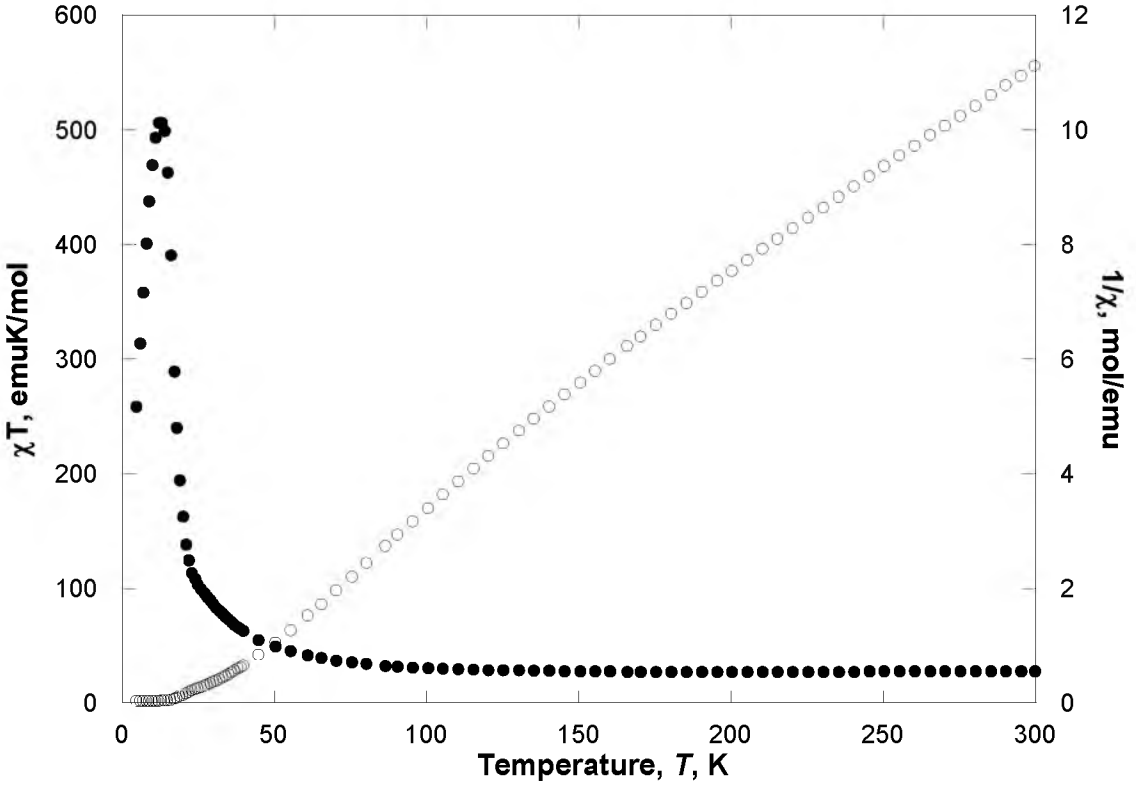

Figure 3.31 χT(T) (●) and 1/χ(T) (○) plots of $[NMe_2Et_2]_3Mn_8(CN)_{19}$•2.4$H_2O$ for (**6**) in a 1000 Oe applied field.

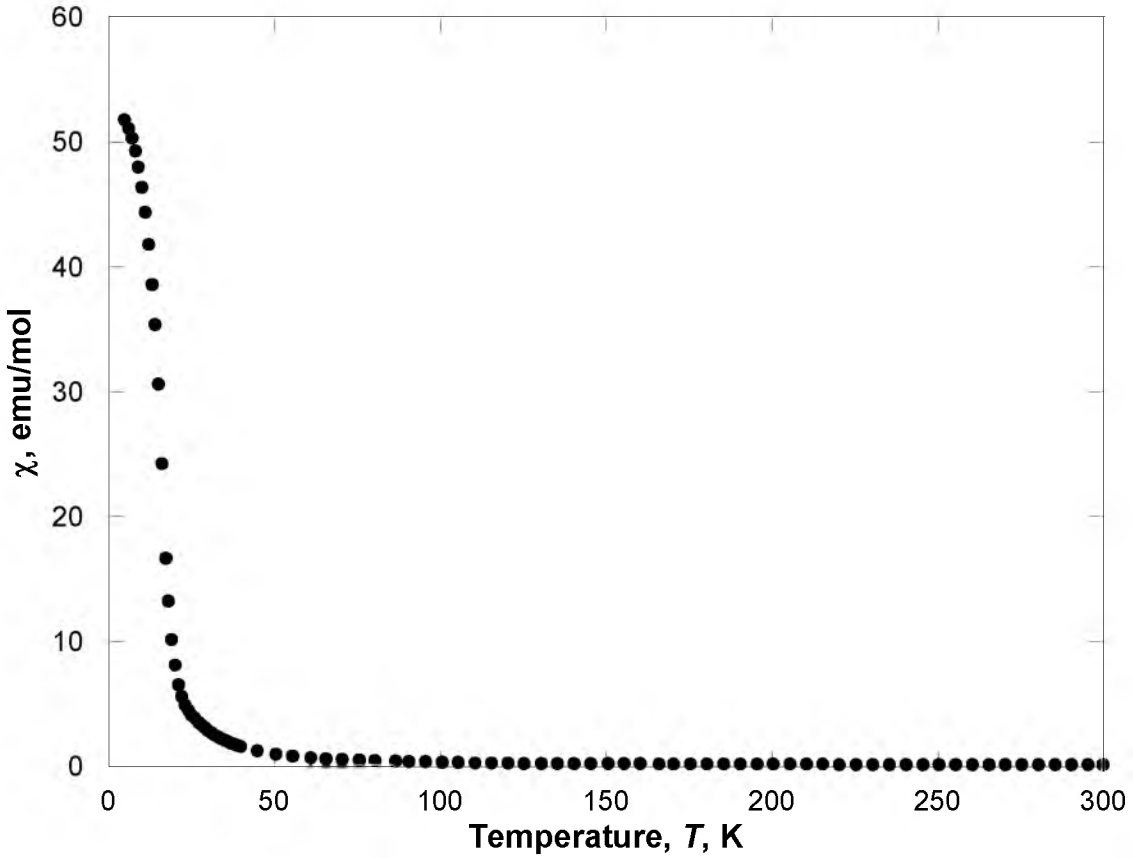

Figure 3.32 χ(T) (●) plot for $[NMe_2Et_2]_3Mn_8(CN)_{19}\bullet 2.4H_2O$ (**6**) in a 1000 Oe applied field.

the 5 Oe $M_{ZFC}(T)$ and $M_{FC}(T)$ magnetization data for **6**, Figure 3.33, the bifurcation temperature, the temperature at which the $M_{ZFC}(T)$ and $M_{FC}(T)$ data are no longer coincident, of 12.75 K was determined. Taking the linear portion of the $M_{ZFC}(T)$ and $M_{FC}(T)$ data, a T_c of 13.8 K was extrapolated. The linear portion of the $M_{REM}(T)$ data, Figure 3.33, was extrapolated to give a T_c of 13.1 K. The ac susceptibility measurement, Figure 3.34, shows a peak in the in-phase component, χ', with a maxima at 12.75 K. A peak is also observed in the out-of-phase component, χ'', with an onset of 13.5 K. The presence of peaks in both in-phase and out-of-phase components indicates that **6** orders as a ferrimagnet. The M(H) data, Figure 3.35, show that **6** nears saturation at 9 T. The magnetization of **6** at 9 T is 89,161 emuOe/mol. The proposed molecular formula for **6** has been derived from TGA analysis with no current X-ray diffraction data to support or detract from the proposed formula. The saturation magnetization, M_s, can be used as a tool to give insight into the number of total spins contributing to the magnetization. By dividing the measured M_s by 5585 emuOe/mol, the M_s value for a single spin, it is determined that there are 16 spins for **6**. Having five hs Mn(II) in the up orientation and one hs with two ls Mn(II) in the down orientation, a net of 18 spins results. It is possible that there is disorder in the crystal structure and in some unit cells, there are four hs Mn(II) in the up orientation and two hs with two ls Mn(II) in the down orientation. If these two cases existed in a ratio of 2:1, the resulting average spin would be 16. While this analysis does not definitively support or refute the current molecular formula,

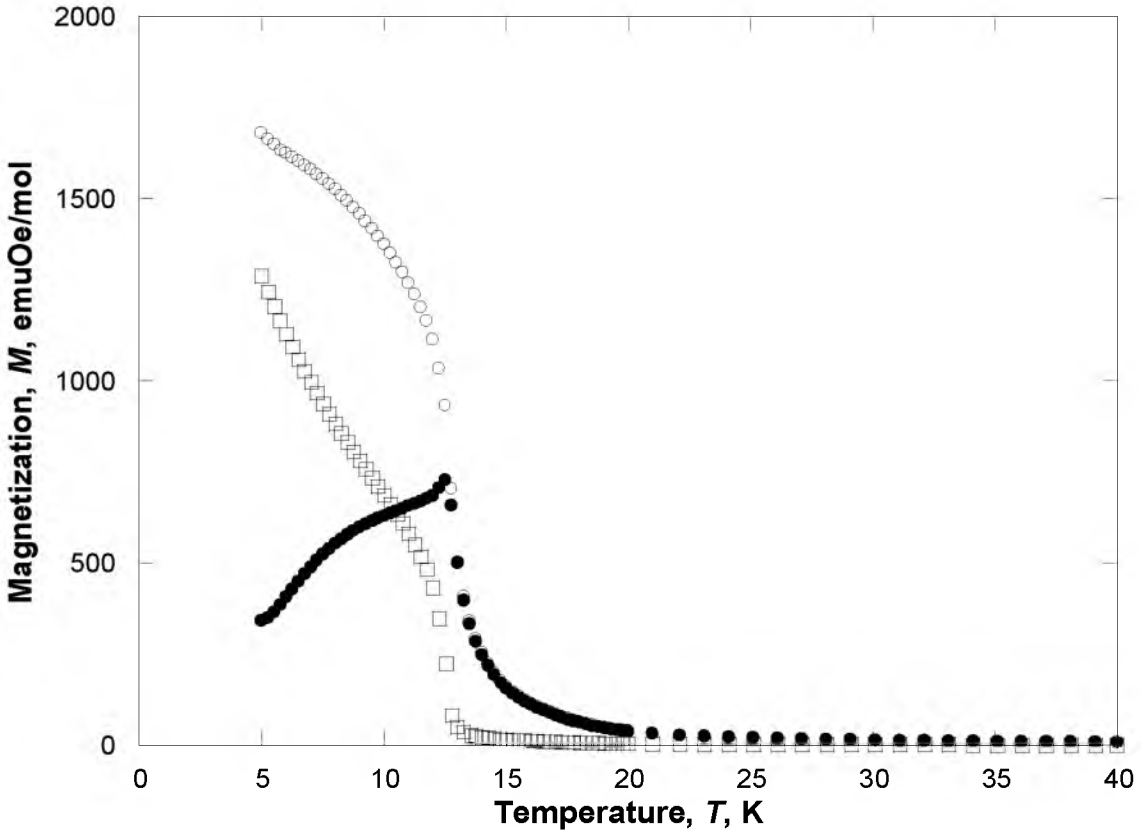

Figure 3.33 5 Oe $M_{ZFC}(T)$ (●), $M_{FC}(T)$ (○), and $M_{rem}(T)$ (□) data for $[NMe_2Et_2]_3Mn_8(CN)_{19}•2.4H_2O$ (**6**).

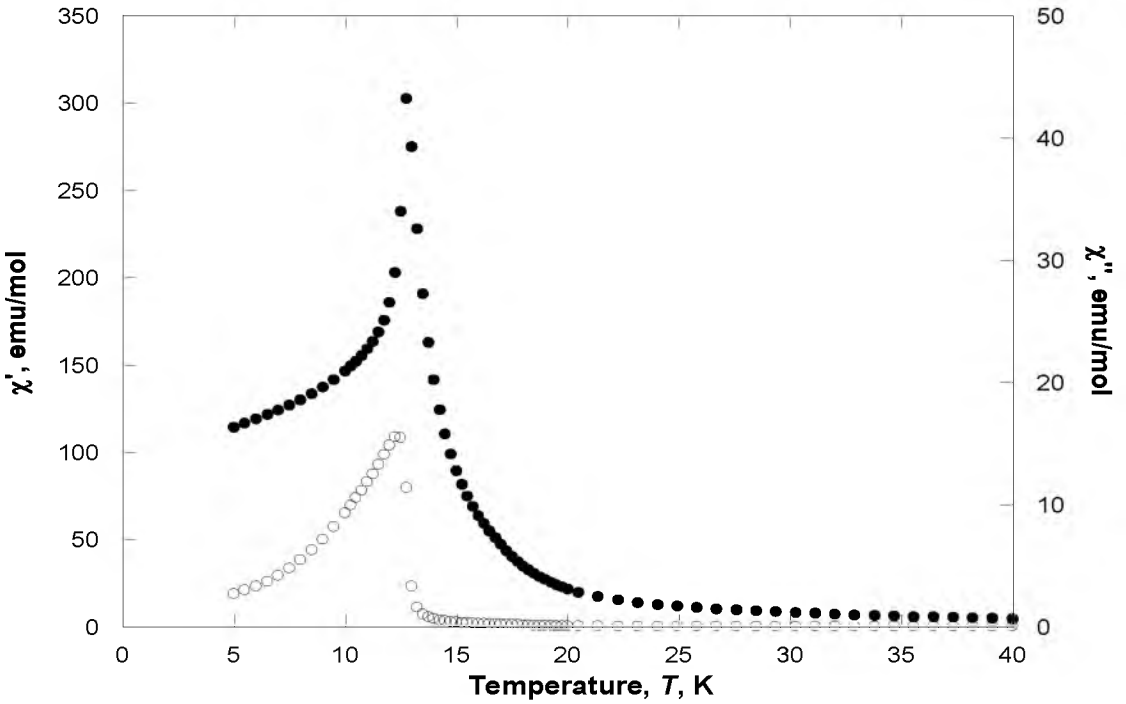

Figure 3.34 Observed in-phase, χ'(T) (●), and out-of-phase, χ''(T) (○), ac susceptibilities at 1000 Hz for $[NMe_2Et_2]_3Mn_8(CN)_{19}\bullet 2.4H_2O$ (**6**).

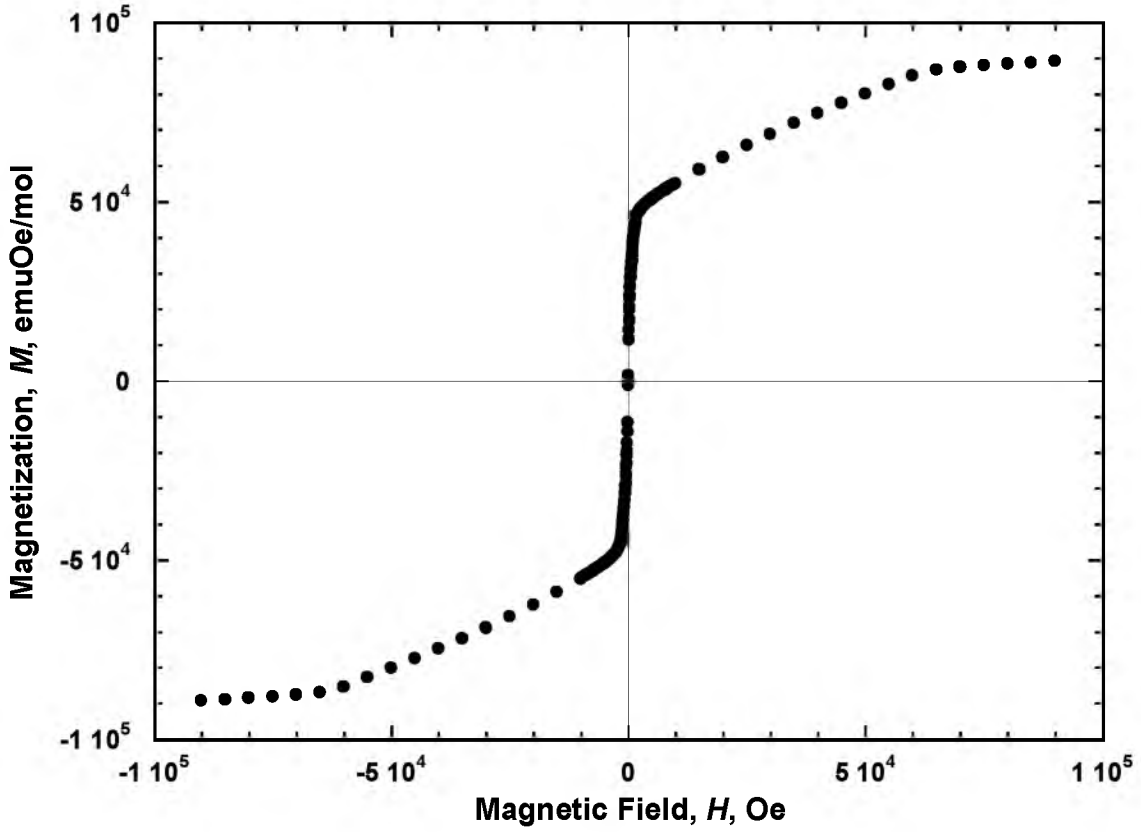

Figure 3.35 Magnetic hysteresis, M(H), of $[NMe_2Et_2]_3Mn_8(CN)_{19}\bullet 2.4H_2O$ (**6**) at 5 K.

it may offer some insight into the compound itself. The magnetic properties are summarized in Table 3.5.

$[NMe_2Et_2]Mn_3(CN)_7$•2 MeOH (7). The room temperature χT of 10.6 emuK/mol was determined through analysis of the χT data, Figure 3.36, of **7** The room temperature χT value is in acceptable agreement with the spin-only value of 13.125 emuK/mol for three high-spin Mn(II) centers. As the temperature decreases, the value of χT slowly decreases until 35 K when the value of χT rapidly increases until it peaks at 35.5 emuK/mol. As temperature further decreases, the value of χT rapidly approaches zero. The $\chi^{-1}(T)$ data, Figure 3.37, for **7** is linear above 200 K. Using the Curie-Weiss expression, $\chi^{-} \propto (T - \theta)^{-1}$, to fit the $\chi^{-1}(T)$ data above 200 K yielded a θ value of -40.5 K. While the

Table 3.5 Summary of the magnetic properties of magnetically pure-phased compounds **6-7.**

	6	**7**
$X_{obs}T$, emuK/mol (300K)	26.9	10.6
$X_{calc}T$, emuk/mol (spin-only)	23.000	13.125
θ, K [Curie-Weiss; $\chi \propto (T - \theta)^{-1}$]	28.6[a], -10.6[b]	-40.5[b]
M, emuOe/mol (90 kOe)	29,531	16,590[c]
Mr, emuOe/mol	—	1981[d]
T_b, K (ZFC/FC)	12.75	25.5
H_{cr}, Oe	—	600[d]
T_c, K [$M_r(T) \rightarrow 0$]	13.1	25.4
T_c, K [$M_{ZFC}(T) \rightarrow 0$]	13.8	26.1
T_c, K [$\chi'(T)_{max}$] (1000 Hz)	12.75	25
T_c, K [$\chi''(T)_{onset}$] (1000 Hz)	13.5	26
Magnetic Ordering	Ferri	Ferri

a) Fit over 45 < T < 115 K. b) Fit over 200 < T < 300 K. c) M(H) run at 5K. d) M(H) run at 2K.

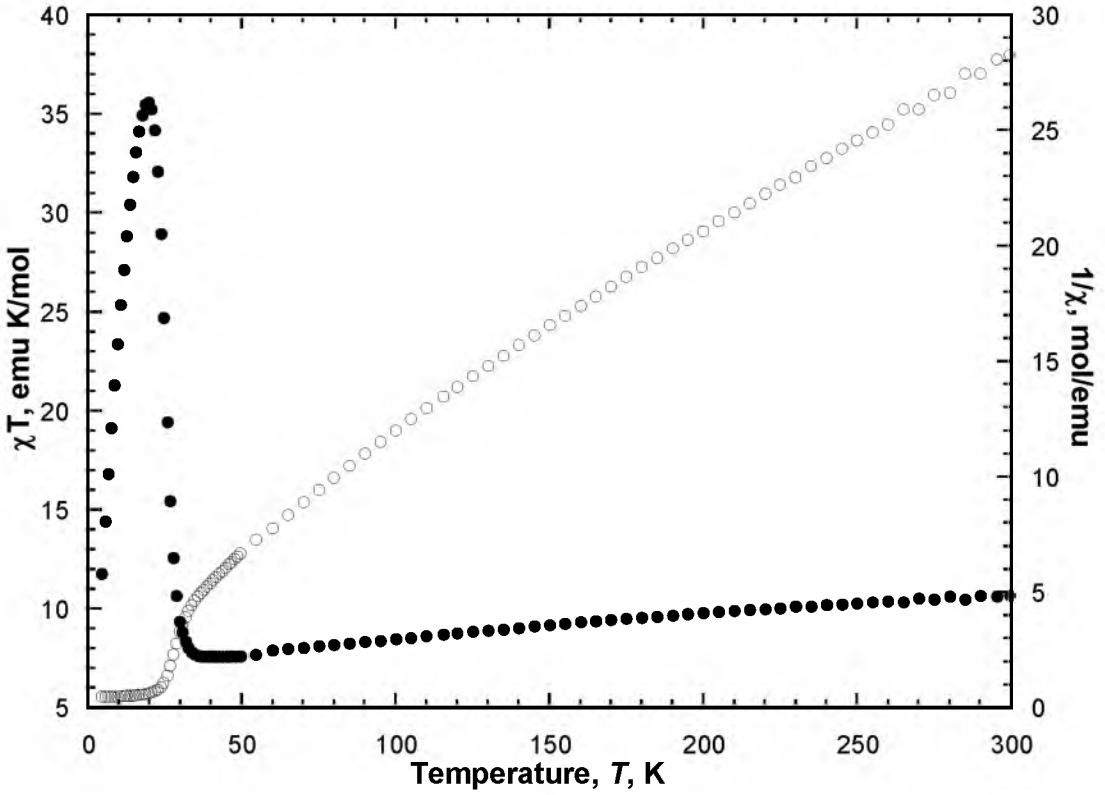

Figure 3.36 χT(T) (●) and 1/χ(T) (○) plots of $[NMe_2Et_2]Mn_3(CN)_7$•2MeOH (**7**) in a 1000 Oe applied field.

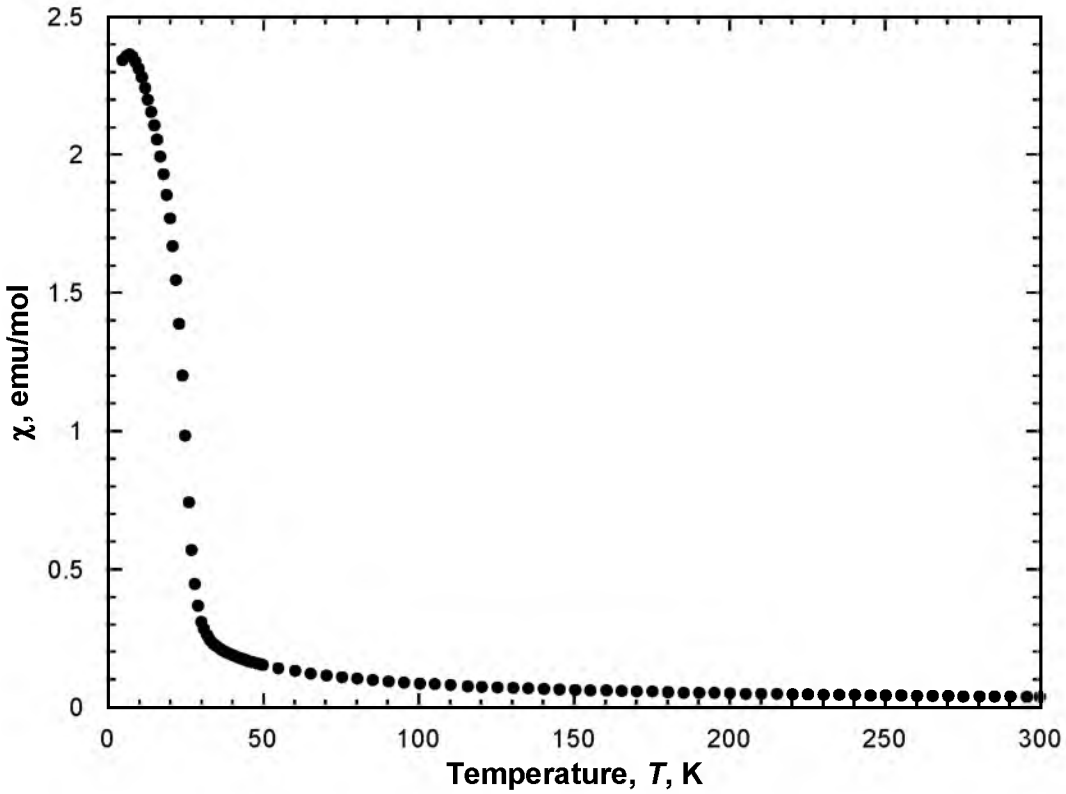

Figure 3.37 χ(T) (●) plot for $[NMe_2Et_2]Mn_3(CN)_7$•2MeOH (**7**) in a 1000 Oe applied field.

magnet orders as a ferrimagnet, significant ferromagnetic coupling is prevalent at higher temperatures.

Analysis of the χ(T) data for **7**, Figure 3.38, illustrates that as temperature increases, susceptibility also increases until it peaks at 7 K and then decreases to a finite susceptibility at higher temperatures. The overlay of the 5 Oe M_{ZFC}(T) and M_{FC}(T) data, Figure 3.39, show a bifurcation temperature, T_b, of 25.5 K for **7**. Extrapolation of the linear portion of the M_{ZFC}(T) and M_{FC}(T) data results in a T_c of 26.1 K. The M_{REM}(T) magnetization, Figure 3.38, was extrapolated over the most linear portion, giving a T_c of 25.4 K.

The ac susceptibility measurement, Figure 3.39, shows a peak in the χ' with a maximum at 25 K and a peak in the χ'' with an onset of 26 K. The presence of peaks in both in-phase and out-of-phase components indicates that **7** orders as a ferrimagnet. The M(H) data, Figure 3.40, shows that **7** has magnetic hysteresis. **7** has a coercive field, H_{cr}, of 600 Oe. Magnetic properties are summarized in Table 3.5.

While several magnetically pure compounds have been synthesized and isolated using the $[NMe_2Et_2]^+$ cation, several mixed-phase compounds were also synthesized. Compound **8** was a mixture with 3 different ordering temperatures. Using the maximum in the χ' as the T_c value, **8** had phases with a T_c at 13 K, 18 K, and 27 K. All 3 phases had an associated χ'' component. Therefore, all 3 phases order as ferrimagnets.

Compound **9** also was composed of 3 phases. Using the maximum in the χ' as the T_c value, **9** had phases with a T_c at 15.5 K, 18.5 K, and 27 K. Like **8**,

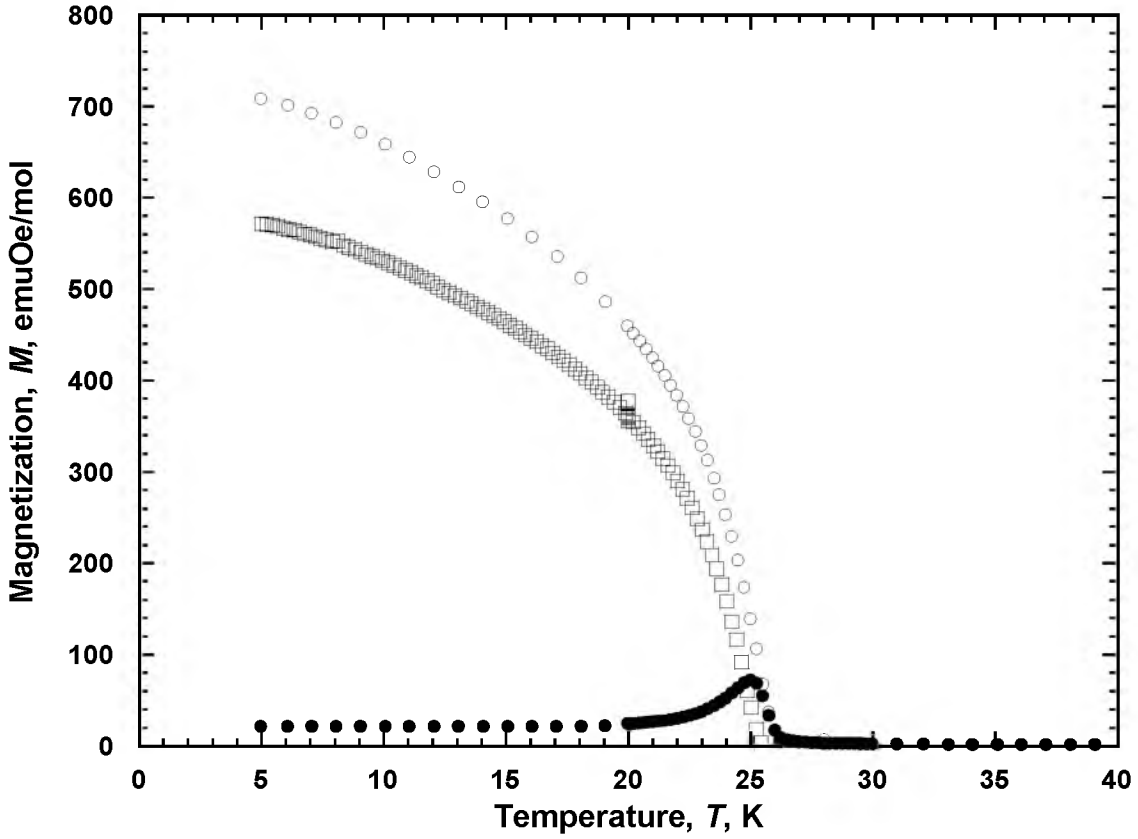

Figure 3.38 5 Oe $M_{ZFC}(T)$ (●), $M_{FC}(T)$ (○), and $M_{rem}(T)$ (□) data for $[NMe_2Et_2]Mn_3(CN)_7$•2MeOH (**7**).

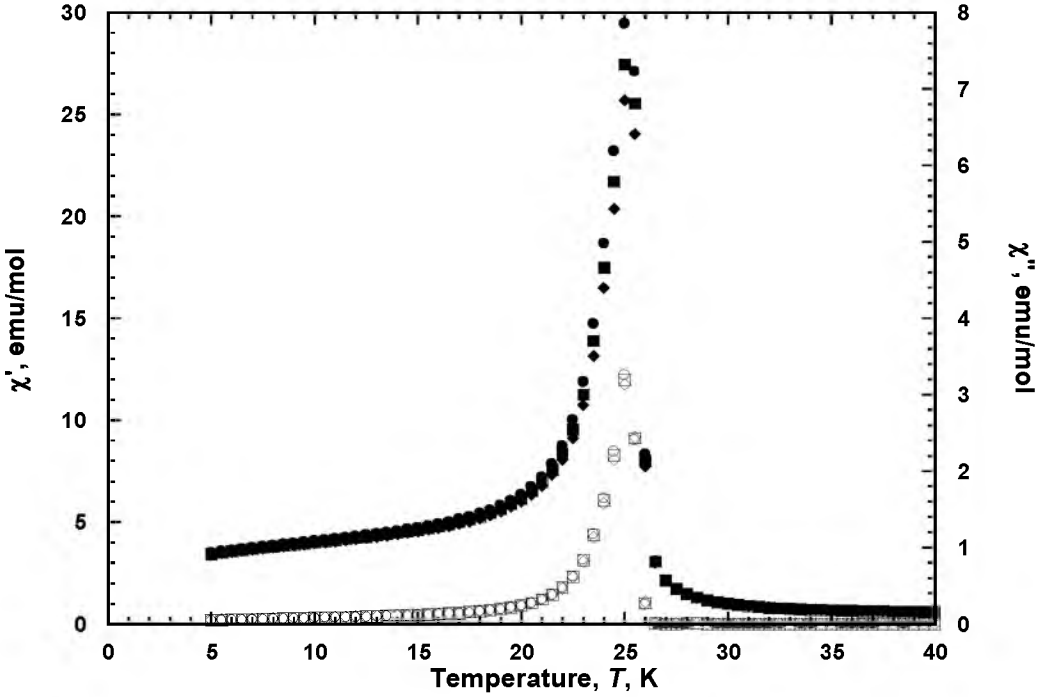

Figure 3.39 Observed in-phase, χ'(T) (filled), and out-of-phase, χ"(T) (open), ac susceptibilities at 100 (●,○), 333 (■,□), and 1000 (♦,◊) Hz for $[NMe_2Et_2]Mn_3(CN)_7$•2MeOH (**7**).

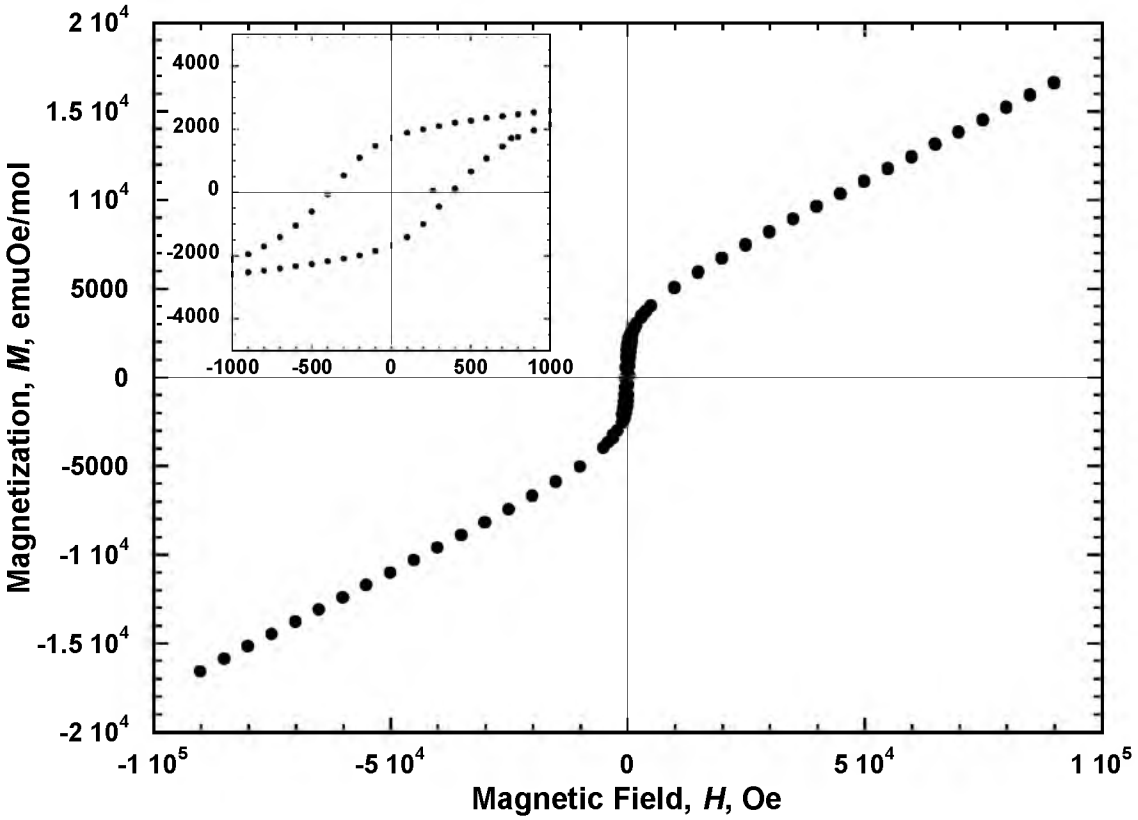

Figure 3.40 Magnetic hysteresis, M(H), of $[NMe_2Et_2]Mn_3(CN)_7$•2MeOH (**7**) at 5 K.

there is a peak in the χ" associated with each peak in the χ'. While it is possible that **8** and **9** are composed of the same phases, the ratios vary between the 2 compounds. Reaction conditions of **8** and **9** are summarized in Table 3.6. Compound **6** has a T_c derived from the ac susceptibility measurements of 12.75 K. Compound **7** has a T_c derived from the ac susceptibility measurements of 26 K. It is possible that **8** and **9** are a mixture of **6** and **7**. The phase responsible for the peak at 18.5 K in **8** and **9** has yet to be isolated.

$[NMeEt_3]^+$ Class

$[NMeEt_3]_2Mn_2(CN)_6$•xMeOH (10). A 4 mL methanol solution of $Mn(O_2CCH_3)_2$ (80.49 mg, 0.465 mmol) was added drop-wise to a stirring 2 mL methanol solution of $[NMeEt_3]CN$ (99.42 mg, 0.699 mmol). A grey precipitate formed that turned yellow and then green within minutes. The reaction mixture was allowed to stir overnight. The green precipitate was isolated via filtration and washed with methanol (3 x 3 mL) and ether (3 x 3 mL). Isolated precipitate was dried under vacuum at room temperature for 5 hr (yield: 41.63 mg, 35%). IR (KBr) 3585 (w), 3427 (w), 2920 (w), 2850 (w), 2062 (s), 1576 (w), 1457 (w), 1022

Table 3.6 Summary of reaction conditions for **6-9.**

	6	**7**	**8**	**9**
Solvent	H_2O	MeOH	H_2O	H_2O
Ratio, CN:Mn	1.5:1	3:1	3:1	7:1
M of CN, Mol/L	1.414	0.253	1.481	1.670
M of Mn, Mol/L	0.886	0.049	0.680	0.319
Added reactant	CN	Mn	CN	CN
Reaction time, hr	3	3	18	3
Magnetic purity	Pure	Pure	Mixed	Mixed

(w) cm^{-1}. Sample used for magnetic analysis was analyzed via TGA and was determined to contain 0.22 equivalents of MeOH. A core diamagnetic correction of -303.0 x 10^{-6} emu/mol was used.

$[NMeEt_3]_3Mn_8(CN)_{19}•xH_2O$ (11). A 3 mL aqueous solution of $[NMeEt_3]CN$ (191.07 mg, 1.343 mmol) was added drop-wise to a stirring 3 mL aqueous solution of $Mn(O_2CCH_3)_2$ (155.15 mg, 0.897 mmol). A grey precipitate formed that turned yellow and then dark green within minutes. The reaction mixture was allowed to stir for 3 hr. The dark green precipitate was isolated via filtration and washed with water (3 x 3 mL), methanol (3 x 3 mL), and ether (3 x 3 mL), and dried under vacuum at room temperature for 3 hr. (yield: 38.63 mg, 42%). IR (KBr) 3630 (m), 2927 (w), 2853 (w), 2060 (s), 1454 (w), 1133 (w), 1013 (w) cm^{-1}. Sample used for magnetic analysis was analyzed via TGA and was determined to contain 0.95 equivalents of H_2O. A core diamagnetic correction of -581.3 x 10^{-6} emu/mol was used.

Results and Discussion

Infrared spectroscopy. Table 3.7 summarizes the ν_{CN} and ν_{OH}, absorptions of compounds **10-11**. The IR spectra of **10**, Figure 3.41, shows a sharp, intense stretch in the CN region at 2061 cm^{-1} with a shoulder at 2081 cm^{-1}.

This is representative of 2 different CN environments within the compound. A sharp absorption is observed at 3582 cm^{-1}. This is a characteristic stretch indicating solvation within the compound. Compound **11** (Figure 3.42) has a double CN peak at 2061 and 2068 cm^{-1}. The shape and location of these CN

Table 3.7 IR, ν_{CN} and ν_{OH}, absorptions and colors of $[NMeEt_3]_2Mn_2(CN)_6$•xMeOH (**10**) and $[NMeEt_3]_3Mn_8(CN)_{19}$•xH_2O (**11**).

	10	**11**
Color	Light Green	Dark Teal
ν_{CN} (cm^{-1})[a]	2061(s), 2081(sh), 2117(w)	2061(s), 2068(s)
ν_{OH} (cm^{-1})[a]	3582(s)	3629(s), 3430(br)

a) Sample was analyzied as a pressed KBr pellet. Relative intensities are included as (s) strong, (m) medium, (w) weak, (br) broad, and (sh) shoulder.

peaks are similar to **6**. The similarities in IR spectra are an indication that **6** and **11** may have the same structure. The sharp peak at 3629 cm^{-1} and broad peak at 3430 cm^{-1} is a result of solvent in the lattice.

Thermogravimetric analysis. The thermogravimetric analysis of **10** (Figure 3.43) shows a loss of solvent from the onset to ~75 °C. At this point, the weight change levels off until ~100 °C when decomposition of the sample slowly begins. The decomposition increases rapidly at ~250 °C and continues until ~320 °C. The thermally stable $Mn(CN)_2$ has formed and remains for the duration of the analysis run. The solvent loss and decomposition resulted in a percent mass loss of 1.39% and 41.9%, respectively. The back calculations to obtain a molecular formula yielded $[NMeEt_3]_2Mn_2(CN)_6$•xMeOH. For this sample, x was 0.22 equiv of MeOH. Analysis of **11** (Figure 3.44) shows a loss of solvent up to 100 °C. At this point, the sample begins to decompose. The decomposition begins with two small steps over the range of 100-200 °C and 200-250 °C. A large step between 250-325 °C completes the decomposition of **11** and leaves the thermally stable $Mn(CN)_2$ product. The loss of solvent and decomposition resulted in a mass loss of 1.32% and 33.0%, respectively. The back calculations

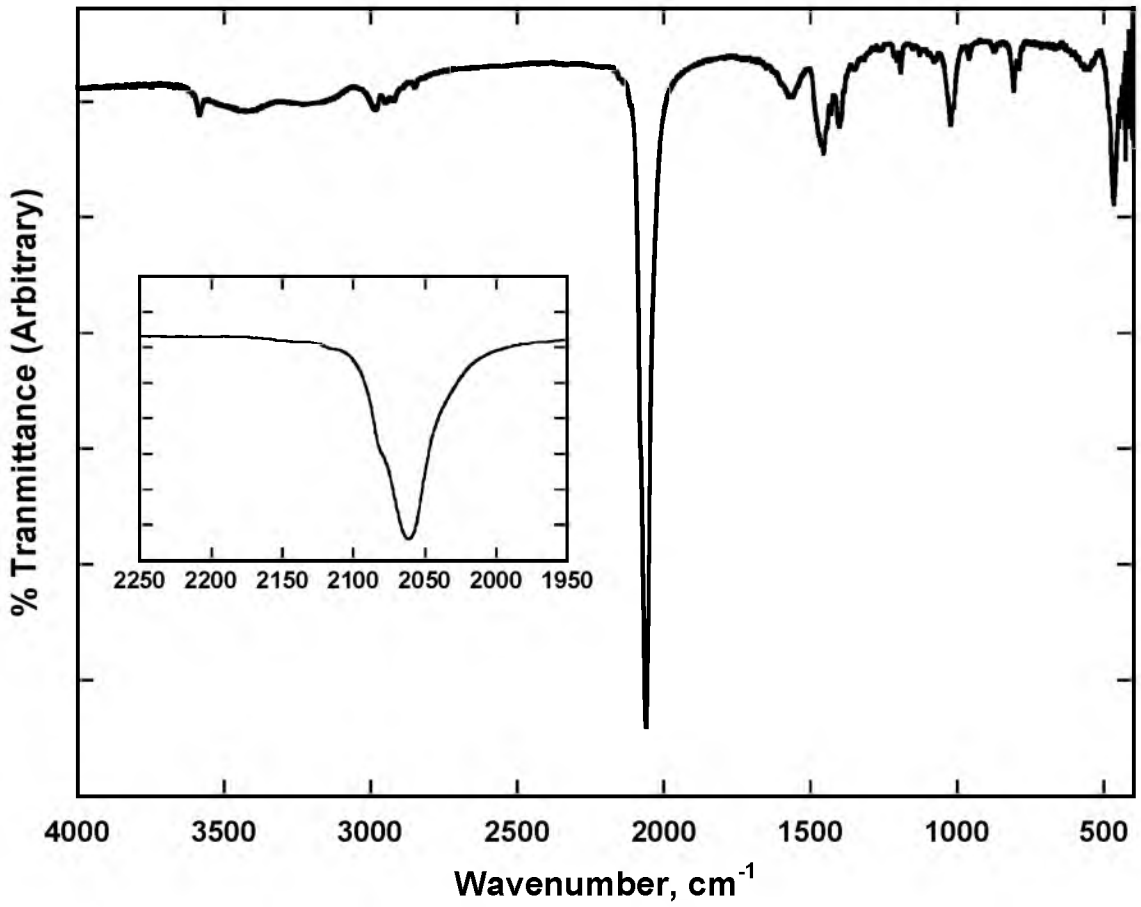

Figure 3.41 IR spectra of $[NMeEt_3]_2Mn_2(CN)_6 \bullet xMeOH$ (**10**) in KBr.

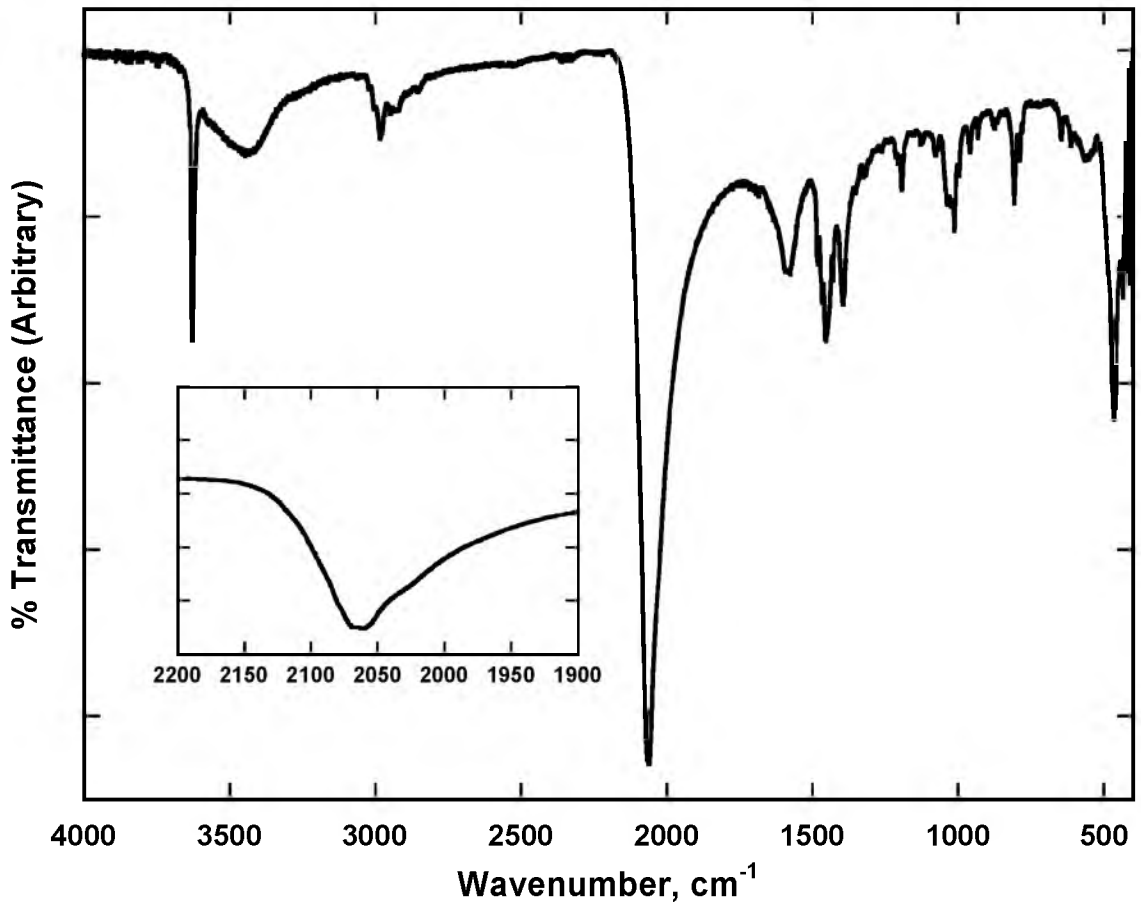

Figure 3.42 IR of $[NMeEt_3]_3Mn_8(CN)_{19}•xH_2O$ (**11**) KBr.

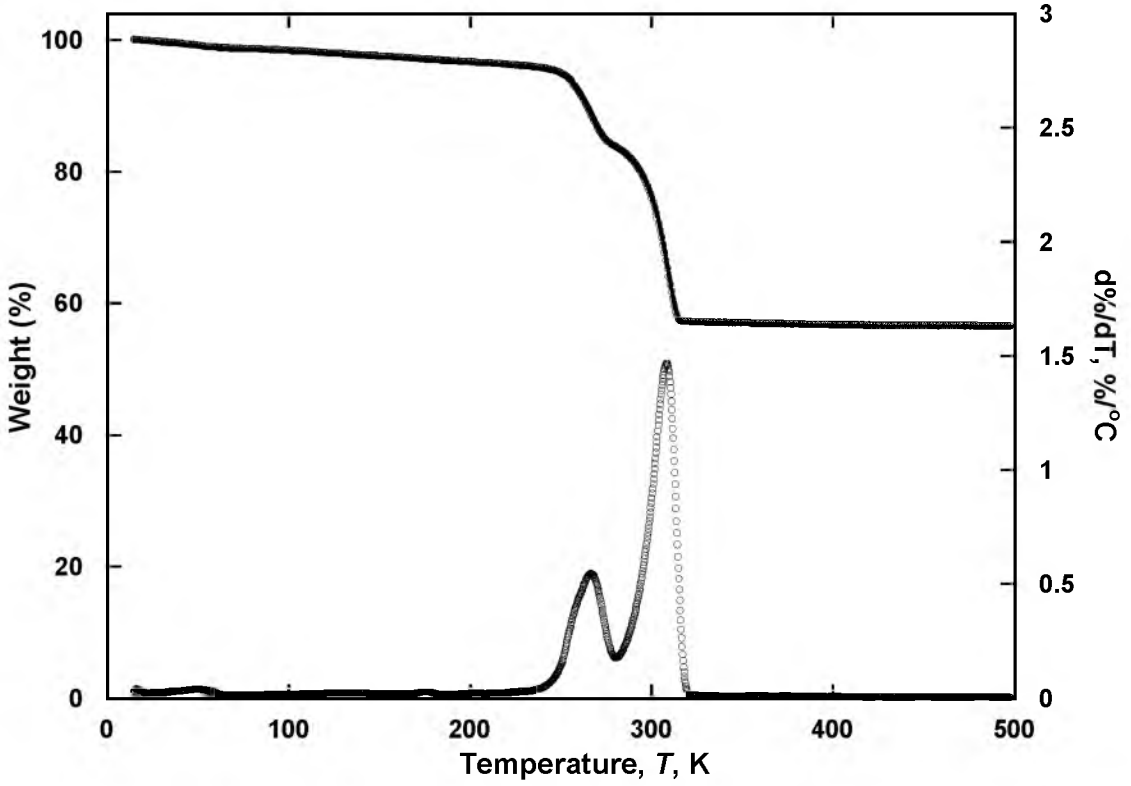

Figure 3.43 TGA trace of $[NMeEt_3]_2Mn_2(CN)_6 \cdot xMeOH$ (**10**) at a heating rate of 1 °C/min.

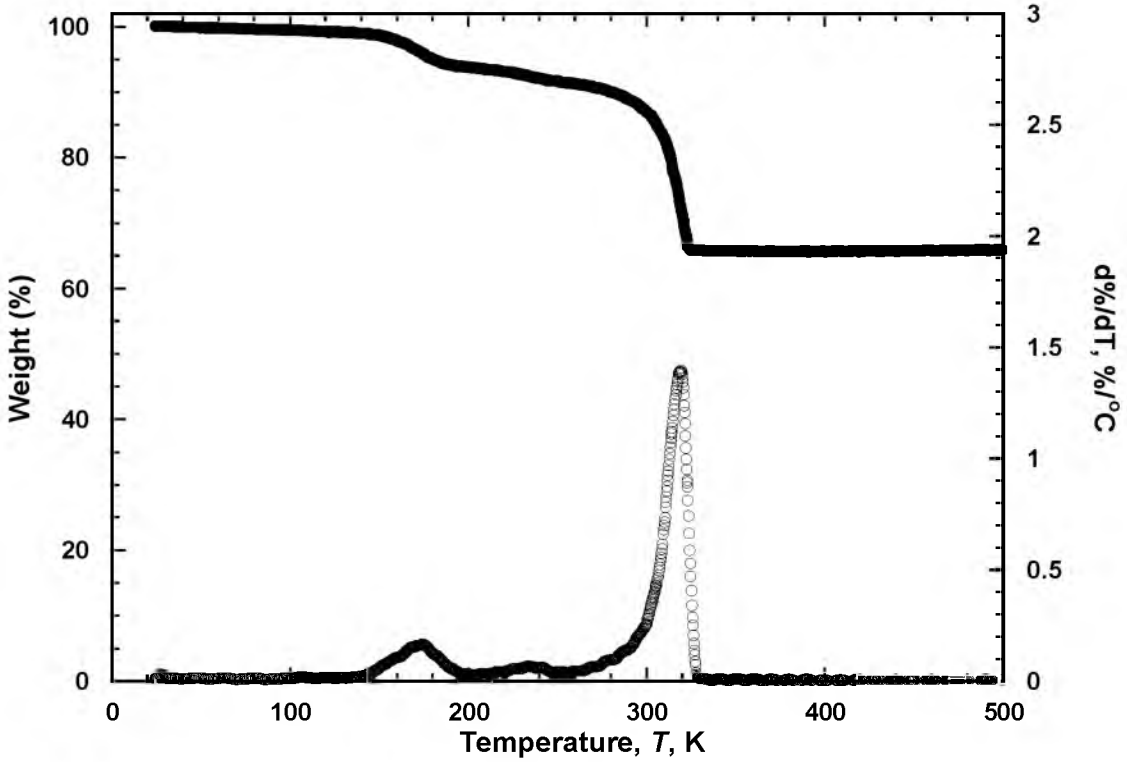

Figure 3.44 TGA trace of $[NMeEt_3]_3Mn_8(CN)_{19}\bullet xH_2O$ (**11**) at a heating rate of 1 °C/min.

to obtain a molecular formula yielded $[NMeEt_3]_3Mn_8(CN)_{19}•xH_2O$. For this sample, x was 0.95 equiv of H_2O. This is the same formula calculated for **6**, except for the different quaternary ammonium ion. When compared, the TGA traces for **6** and **11** both have a three-step decomposition. It should be noted that the onset and subsequent end point for the decomposition of **6** and **11** differ. While it is not certain what factors are in play to affect the thermal stability of the two compounds, it is the author's opinion that both compounds are nearly isostructural.

Magnetic Properties

$[NMeEt_3]_2Mn_2(CN)_6$•xMeOH (**10**). **10** has a measured room temperature χT of 8.19 emuK/mol (Figure 3.45) that is in fair agreement with the spin-only room temperature χT of 8.75 emuK/mol for a two high-spin Mn(II) (S=5/2) system. Following the χT value as the temperature is decreased shows a relatively stable value until 50 K where the χT value sharply rises until reaching a maximum value of 158.3 emuK/mol at 21.1 K and then sharply dropping off toward zero. The χ^{-1}(T) data for **10** (Figure 3.45) are linear over the range of 200 < T < 300 K. A θ value of -28 K was found by fitting the χ^{-1}(T) using the Curie-Weiss expression.

Analysis of the χ(T) data for **10** (Figure 3.46) as temperature increases shows an increasing susceptibility until it sharply peaks at 10 K with a value of 9.84 emu/mol and then rapidly decreases towards zero at higher temperatures. The peak in the χ(T) data is indicative of magnetic ordering. Analysis of the **10**

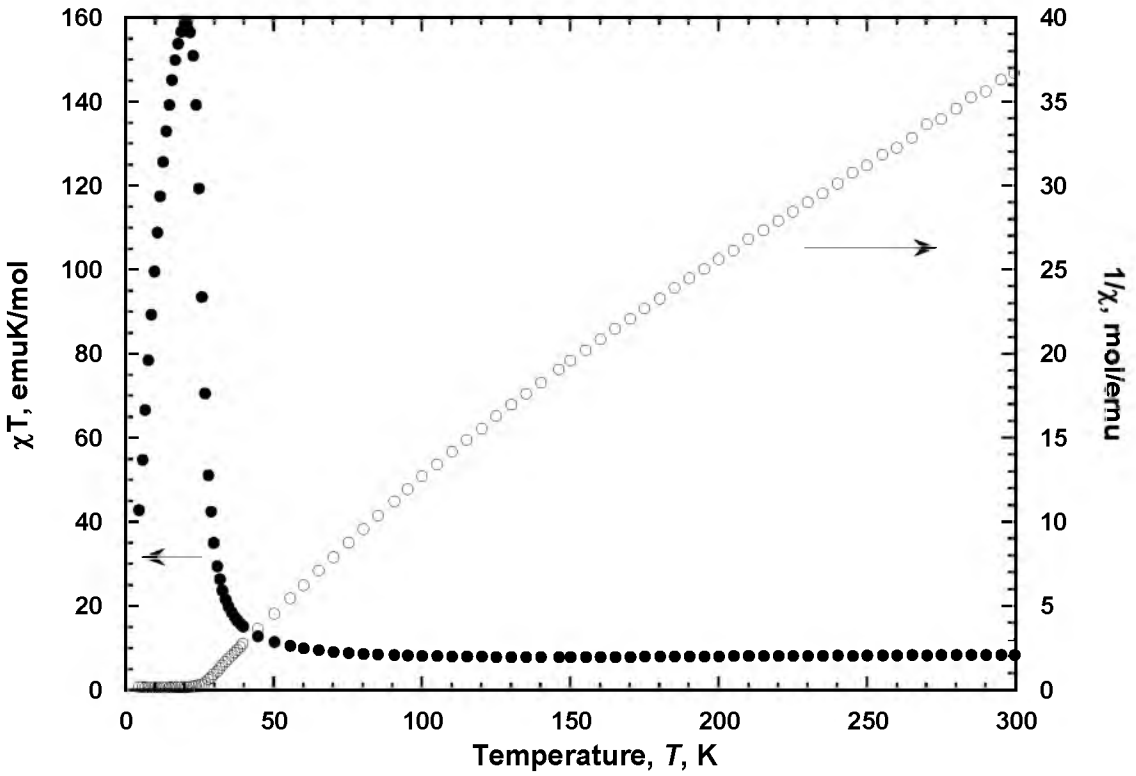

Figure 3.45 χT(T) (●) and 1/χ(T) (○) plots of $[NMeEt_3]_2Mn_2(CN)_6$•0.22MeOH (**10**) in a 1000 Oe applied field.

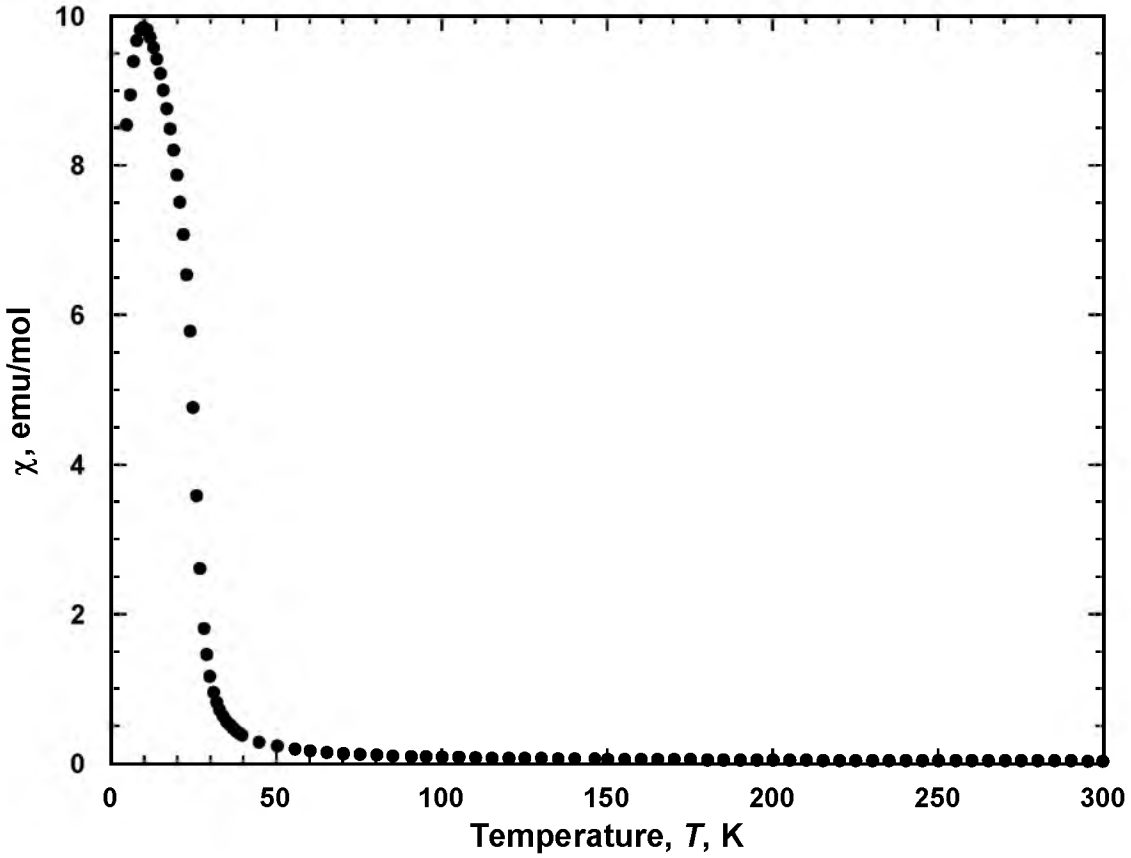

Figure 3.46 χ(T) (●) plot for $[NMeEt_3]_2Mn_2(CN)_6 \cdot 0.22MeOH$ (**10**) in a 1000 Oe applied field.

Oe $M_{ZFC}(T)$ and $M_{FC}(T)$ magnetizations (Figure 3.47) of **3** yielded a bifurcation temperature, T_b, of 30.0 K. The $M_{rem}(T)$ magnetization (Figure 3.47) yields a T_c of 25.4 K.

The ac susceptibility for **10** (Figure 3.48) shows a single peak in the $\chi'(T)$ and two peaks in the $\chi''(T)$ data. The peaks in the $\chi''(T)$ data are indicative of ferri- or ferromagnetic ordering in the compound. Also, multiple peaks in the $\chi''(T)$ data are an indication that the sample is not magnetically pure. However, when a sample contains multiple magnetic phases, there is more than one peak in the $\chi T(T)$ data. As the $\chi T(T)$ plot only shows a single peak, the second peak in the $\chi''(T)$ data can be attributed to a small impurity. The M(H) data of **10** (Figure 3.49), taken at 5 K, does not reach saturation below 9 T. At 9 T, **10** has a measured magnetization of 34,680 emuOe/mol. Magnetic hysteresis behavior is observed for **10**. A coercive field, H_c, of 650 Oe and a remnant magnetization, M_r, of 9,969 emuOe/mol is seen in the M(H) data. Magnetic properties are summarized in Table 3.8.

$[NMeEt_3]_3Mn_8(CN)_{19}\bullet xH_2O$ CGH (**11**). The χT data for **11** (Figure 3.50) show that this compound has a room temperature χT of 25.36 emuK/mol. This value is appreciably lower than the spin-only value of 27.375 emuK/mol for a six high-spin Mn(II) (S = 5/2) and two low-spin Mn(II) (S=1/2) system. The $\chi T(T)$ does not change as the temperature is cooled until 100 K at which point the data increases until reaching a peak of 37.96 emuK/mol at 29 K. Below 29 K, the χT value dips before increasing to a value of 50.1 emuK/mol at 10 K. After peaking at 10 K, the data drop towards zero at lower temperatures. The χ^{-1} data

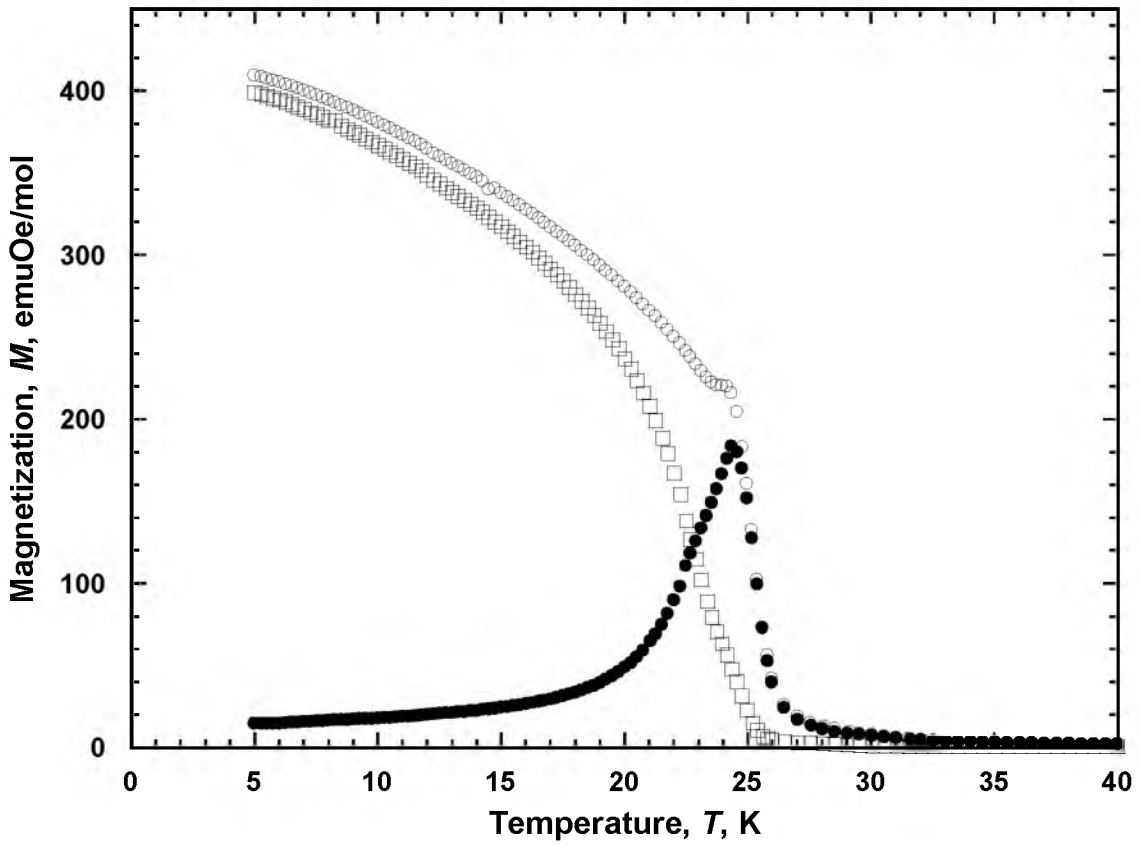

Figure 3.47 5 Oe $M_{ZFC}(T)$ (●), $M_{FC}(T)$ (○), and $M_{rem}(T)$ (□) data for $[NMeEt_3]_2Mn_2(CN)_6$•0.22MeOH (**10**).

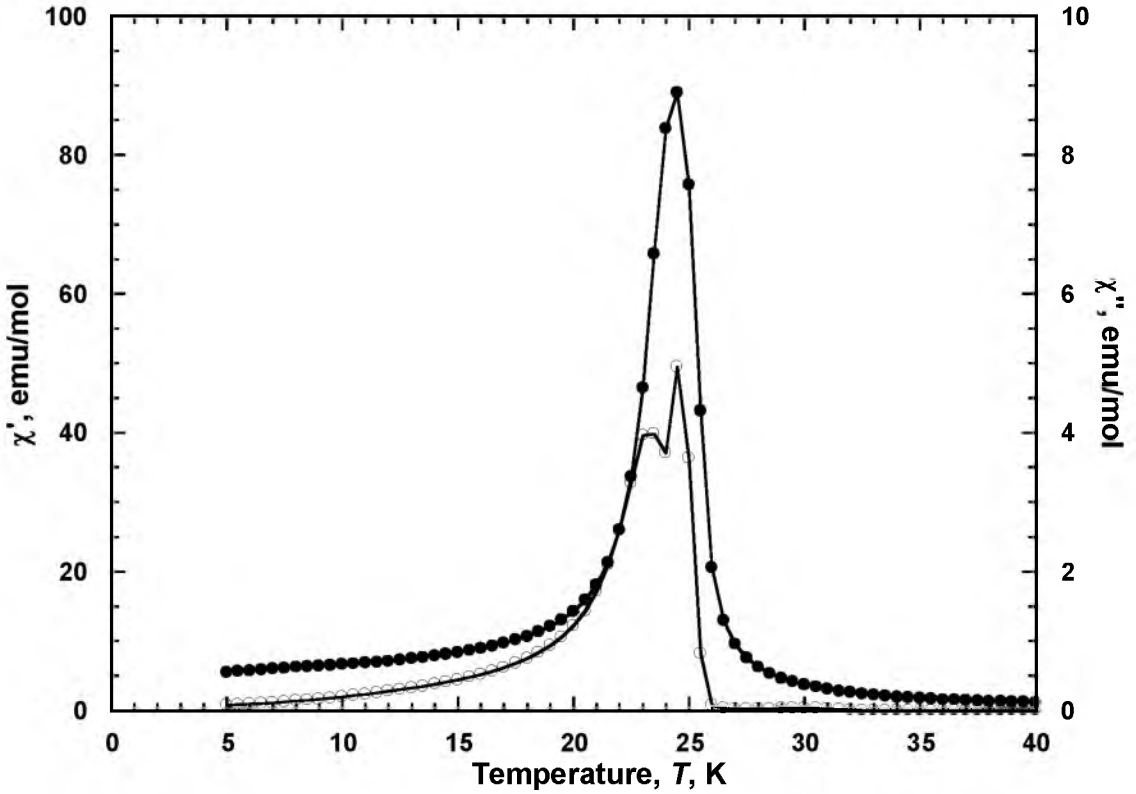

Figure 3.48 Observed in-phase, χ'(T) (●), and out-of-phase, χ''(T) (○), ac susceptibilities at 1000 Hz for $[NMeEt_3]_2Mn_2(CN)_6$•0.22MeOH (**10**). Lines are added to guide the eye.

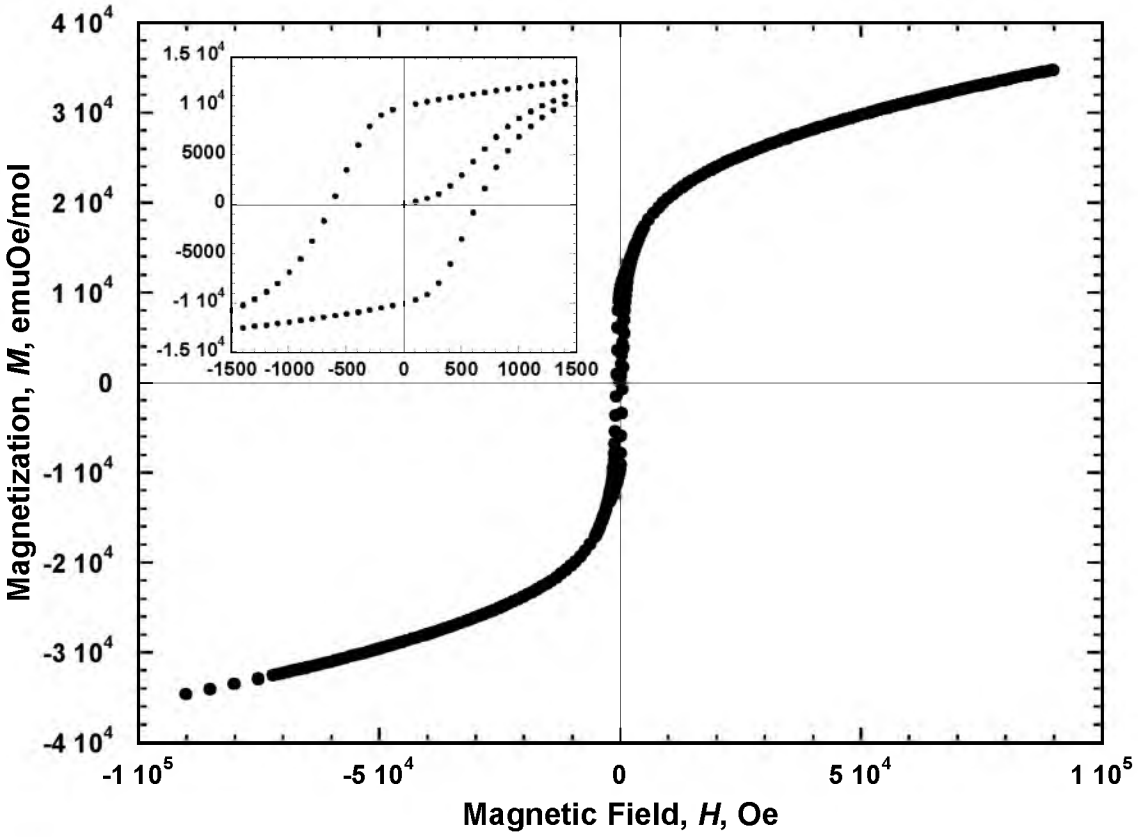

Figure 3.49 M(H) plot for $[NMeEt_3]_2Mn_2(CN)_6 \cdot 0.22MeOH$ (**10**) at 5 K.

Table 3.8 Summary of the magnetic properties of magnetically pure-phased compounds **10-11.**

	10	**11**
$X_{obs}T$, emuK/mol (300K)	8.19	25.36
$X_{calc}T$, emuk/mol (spin-only)	8.75	27.375
θ, K [Curie-Weiss; $\chi \propto (T - \theta)^{-1}$]	-28	-17.5
M, emuOe/mol (5K, 90 kOe)	34,680	99,117
Mr, emuOe/mol	9,969	1,145
T_b, K (ZFC/FC)	30	14.25
H_{cr}, Oe (5K)	650	170
T_c, K [$M_r(T) \rightarrow 0$]	25.4	13.8
T_c, K [$M_{ZFC}(T) \rightarrow 0$]	26.3	18.4
T_c, K [$\chi'(T)_{max}$] (1000 Hz)	24.4	8.5
T_c, K [$\chi''(T)_{onset}$] (1000 Hz)	25.6	10.5
Magnetic Ordering	Ferri	Ferri

b) Fit over 45 < T < 115 K. b) Fit over 200 < T < 300 K. c) Obtained from M(H).

(Figure 3.50) are linear over the range of 150 < T < 300 K. A θ value of -17.5 K was found by fitting the $\chi^{-1}(T)$ using the Curie-Weiss expression.

The $\chi(T)$ data (Figure 3.51) for **11** show the $\chi(T)$ value rise to 5.67 emuK/mol at 8 K before rapidly decreasing towards zero at higher temperatures. Through the 5 Oe $M_{ZFC}(T)$ and $M_{FC}(T)$ magnetization data for **11**, Figure 3.52, the bifurcation temperature, the temperature at which the $M_{ZFC}(T)$ and $M_{FC}(T)$ data are no longer coincident, of 14.25 K was determined. The most steeply rising portion of the $M_{REM}(T)$ data (Figure 3.52) was extrapolated to give a T_c of 13.8 K. The ac susceptibility measurement (Figure 3.53) shows a peak in the in-phase component, χ', with a maximum at 8.5 K. A peak is also observed in the out-of-phase component, χ'', with an onset of 10.5 K. The presence of peaks in both in- phase and out-of-phase components indicates that **11** orders as a

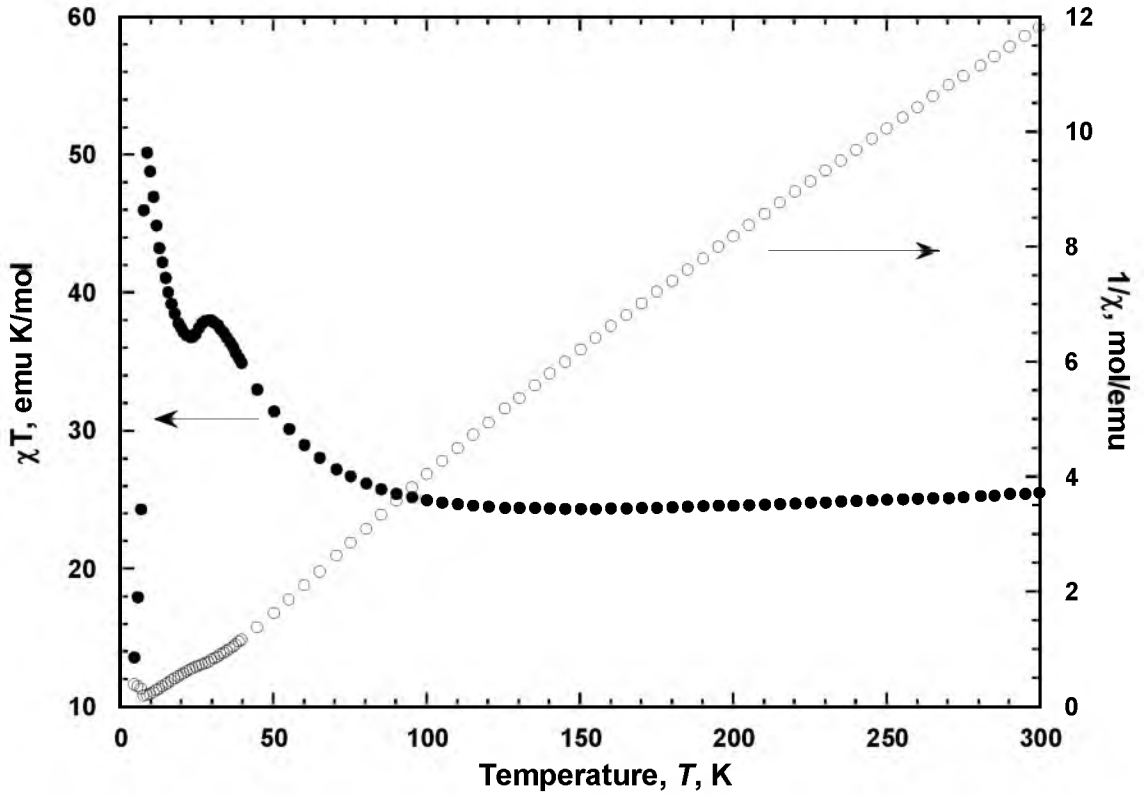

Figure 3.50 χT(T) (●) and 1/χ(T) (○) plots of $[NMeEt_3]_3Mn_8(CN)_{19}\bullet 0.95H_2O$ (**11**) in a 1000 Oe applied field.

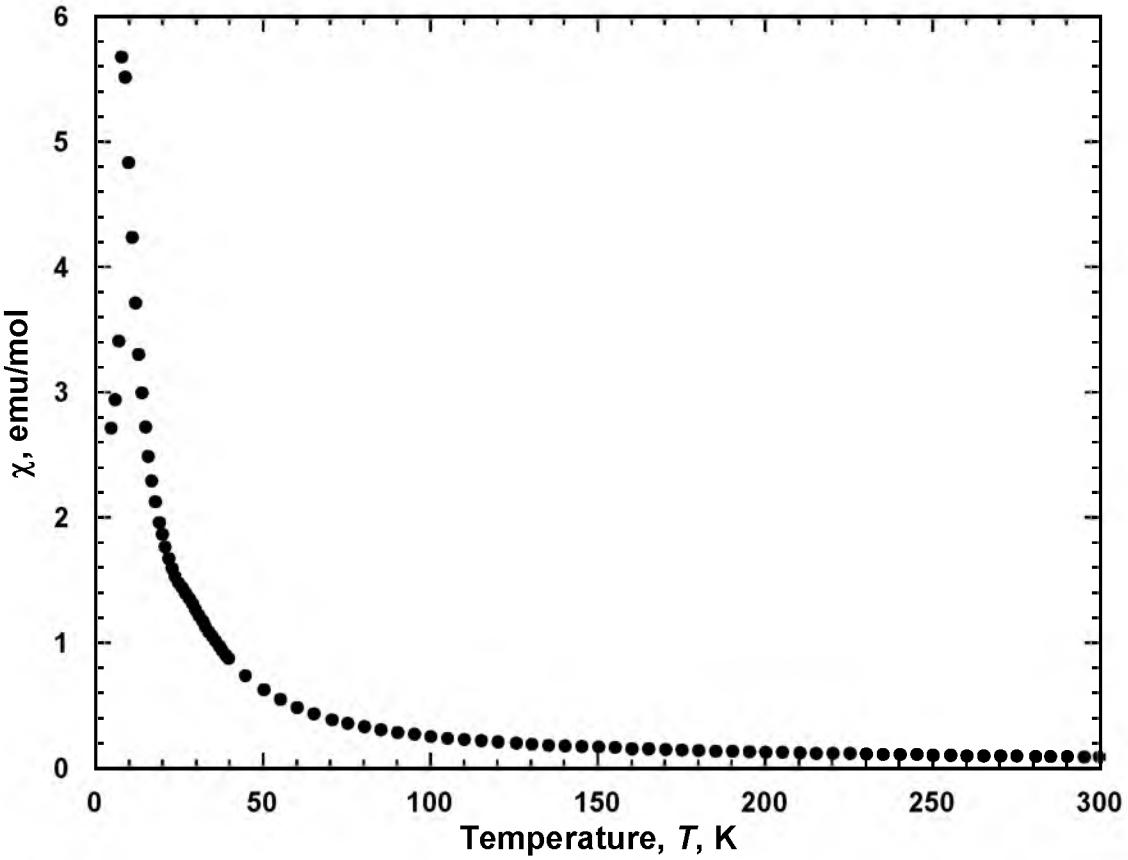

Figure 3.51 χ(T) (●) plot for $[NMeEt_3]_3Mn_8(CN)_{19}\cdot 0.95H_2O$ (**11**) in a 1000 Oe applied field.

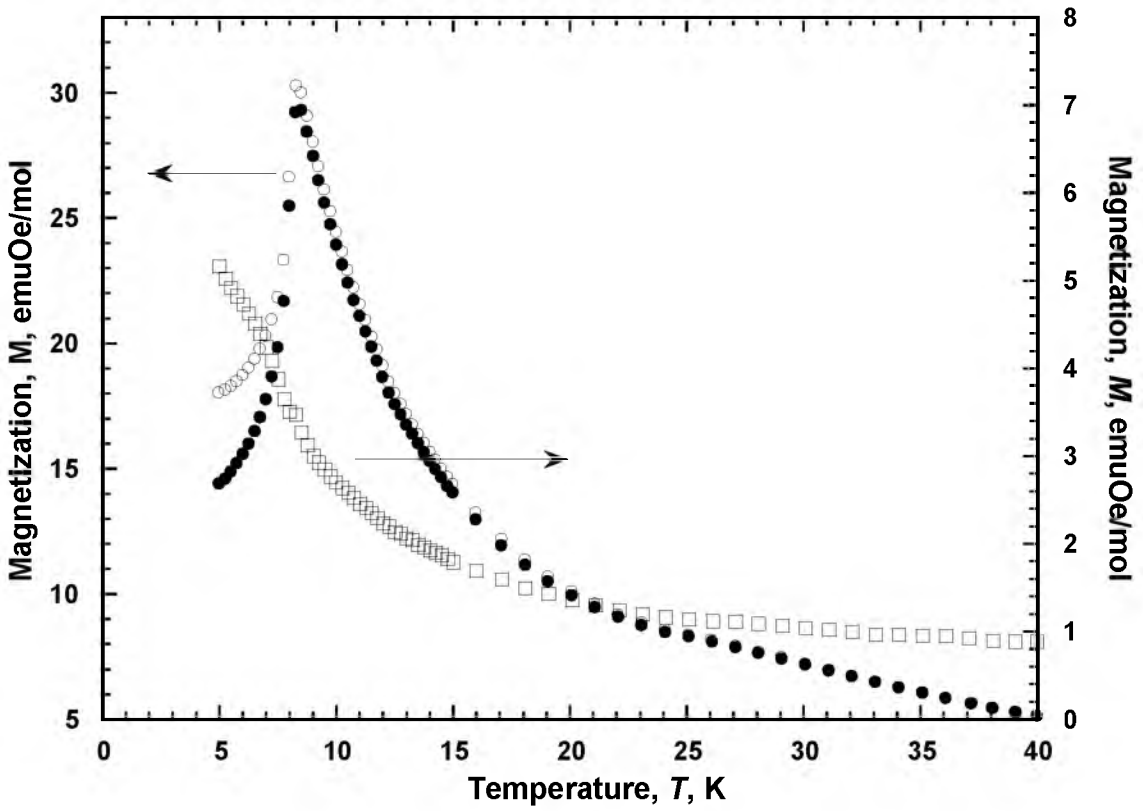

Figure 3.52 5 Oe $M_{ZFC}(T)$ (●), $M_{FC}(T)$ (○), and $M_{rem}(T)$ (□) data for $[NMeEt_3]_3Mn_8(CN)_{19}•0.95H_2O$ (**11**).

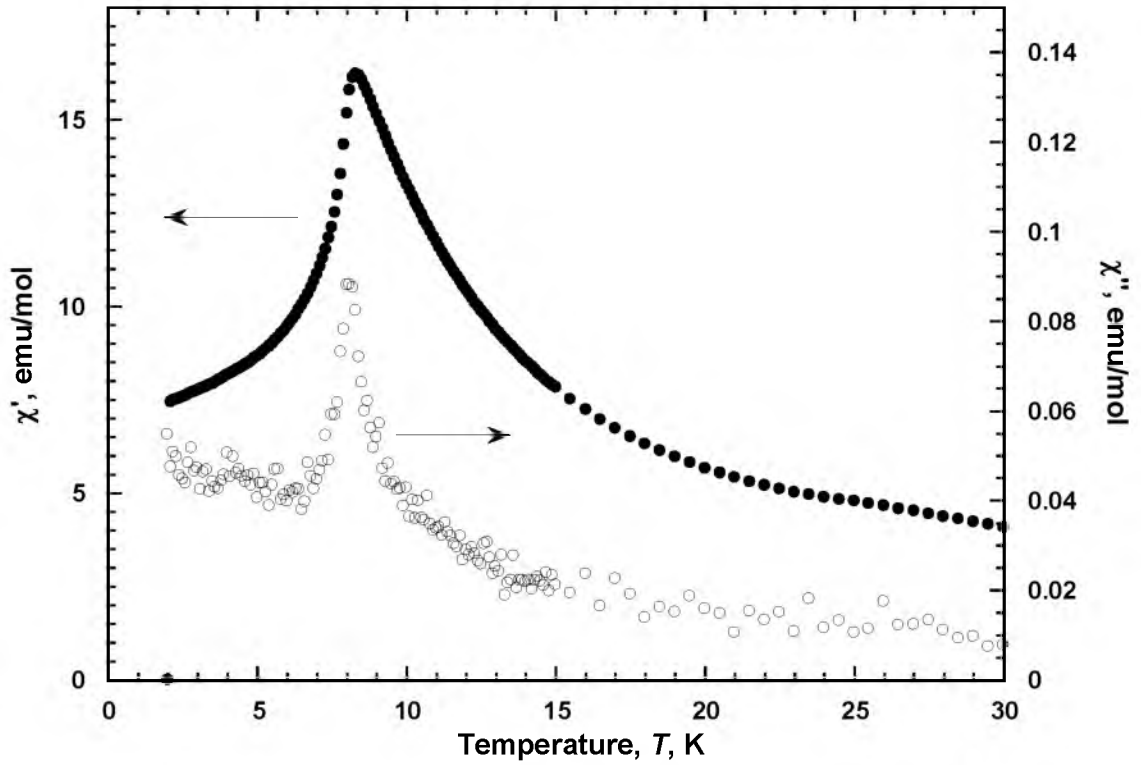

Figure 3.53 Observed in-phase, χ'(T) (●), and out-of-phase, χ''(T) (○), ac susceptibilities at 1000 Hz for $[NMeEt_3]_3Mn_8(CN)_{19}\bullet 0.95H_2O$ (**11**).

ferrimagnet. Analysis of the M(H) data (Figure 3.54) collected at 5 K shows that **11** does not reach saturation below 9 T. At 9 T, the compound reaches a magnetization of 99,117 emuOe/mol. Magnetic hysteresis behavior is observed for **11**. A coercive field, H_c, of 170 Oe and a remnant magnetization, M_r, of 1,145 emuOe/mol were measured. A summary of magnetic properties for **11** is found in Table 3.8. Reaction conditions for compounds 10-11 are listed in Table 3.9.

Conclusion

The initial work of synthesizing PBAs via the reaction of tetraalkylammonium cyanide with manganese salts used spherical tetraalkylammonium cations and resulted in $[NEt_4]_2Mn_3(CN)_8$, $[NEt_4]Mn_3(CN)_7$, and $[NMe_4]_3Mn_5(CN)_{13}$. These three structures all possess a unit cell different from the classical PB face-centered cubic unit cell. $[NEt_4]Mn_3(CN)_7$ is the first PBA reported to possess an antiferromagnetic ground state.[3] $[NMe_4]_3Mn_5(CN)_{13}$ is the first PBA to have layers that are composed of pentagonal and triangular rings. Also, $[NMe_4]_3Mn_5(CN)_{13}$ is the first PBA reported to have a pentacyanomanganate ion.[2] The pentacyanomanganate ion was found to exist in both the square pyramidal and trigonal bipyramidal orientations.

This chapter presented the continuation of previous work describing the synthesis and characterization of seven novel PBAs synthesized with non-spherical tetraalkylammonium cations, e.g. $[NMe_3Et]^+$, $[NMe_2Et_2]^+$, and $[NMeEt_3]^+$. Reaction of $[NMe_3Et]CN$ with Mn^{II} acetate resulted in solvated $[NMe_3Et]_3Mn_5(CN)_{13}$ (**1**), $[NMe_3Et]_5Mn_9(CN)_{23}$ (**2**), and $[NMe_3Et]_2Mn_3(CN)_8$ (**3**)

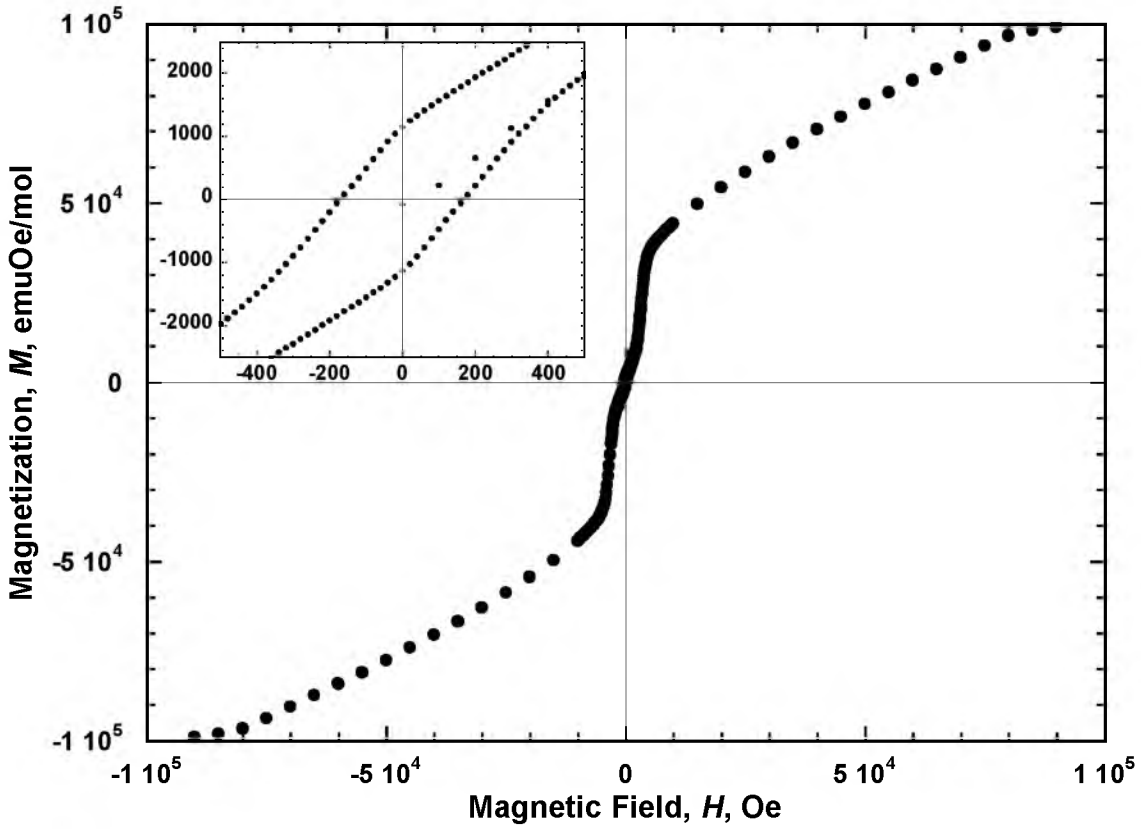

Figure 3.54 M(H) plot for $[NMeEt_3]_3Mn_8(CN)_{19}\bullet 0.95H_2O$ (**11**) at 5 K.

Table 3.9 Summary of reaction conditions for **10-11**.

	10	**11**
Solvent	H_2O	MeOH
Ratio, CN:Mn	1.5:1	1.5:1
M of CN, mol/L	0.350	0.448
M of Mn, mol/L	0.116	0.300
Added reactant	Mn	CN
Reaction time, hr	18	3
Magnetic purity	Pure	Pure

1 has the same layered structure as the previously reported $[NMe_4]_3Mn_5(CN)_{13}$compound. However, **1**, unlike the previously reported compound, is ordered along the z-axis. The ordered bonding between layers leads to an antiferromagnetic ground state. **2** is the first reported gold-colored PBA synthesized via this route. **2** orders as an antiferromagnet, making **2** the second reported uniquely structured PBA with an antiferromagnetic ground state. **3**, while having a ferromagnetic ground state, displays spin-glass or spin-frustratedbehavior.

Reaction of $[NMe_2Et_2]CN$ with Mn^{II} acetate resulted in solvated $[NMe_2Et_2]_3Mn_8(CN)_{19}$ (**6**) and $[NMe_2Et_2]Mn_3(CN)_7$ (**7**). Due to the ongoing structural analysis of **6** and **7**, limited structural information can be reported at the time of this writing. However, **6** has a molecular formula not previously reported for a PBA synthesized via the reported synthetic route. **7** has the same molecular formula as a previously reported compound, $[NEt_4]Mn_3(CN)_7$. However, the magnetic data indicate that there is a structural/connectivity difference. The previously reported compound has one low-spin (S=1/2) octahedral Mn^{II} site and two high-spin (S=5/2) Mn^{II} sites. The magnetic data for **7** indicates that all three Mn^{II} sites are high-spin (S=5/2) sites.

Reaction of $[NMe_2Et_2]CN$ with Mn^{II} acetate resulted in solvated $[NMeEt_3]_2Mn_2(CN)_6$ (**10**) and $[NMeEt_3]_3Mn_8(CN)_{19}$ (**11**). While **10** has the classic PB molecular formula, magnetic data indicate that both Mn^{II} sites are high-spin (S=5/2). This differs from the classic one high-spin (S=5/2) and one low-spin (S=1/2) system that is characteristic of the classic PB. Greater insight into the coordination environments will be obtained when the structure of **10** is resolved. **11** has the same molecular formula as **6** and initial work on the structures of **6** and **11** indicate that they are isostructural and have a cubic unit cell.

References

(1) (a) Verdaguer, M.; Girolami, G. S. In *Magnetism - Molecules to Materials*; Miller, J. S., Drillon, M., Eds.; Wiley-VCH: Weinheim, 2005, Vol. 5, p 283.

(b) Hashimoto, K.; Ohkoshi, S. Phil. *Trans. R. Soc.* Lond. A 1999, 357, 2977. (c) Verdaguer, M.; Bleuzen, A.; Marvaud, V.; Vaissermann, J.; Seuleiman, M.; Desplanches, C.; Scuiller, A.; Train, C.; Garde, R.; Gelly, G.; Lomenech, C.; Rosenman, I.; Veillet, P.; Cartier, C.; Villain, F. Coord. *Chem. Rev.* 1999, 190-192, 1023. (d) Ferlay, S.; Mallah, T.; Ouahes, R.; Veillet, P.; Verdaguer, M. *Nature* 1995, 378, 701. (e) Dujardin, E.; Ferlay, S.; Phan, X.; Desplanches, C.; Moulin, C. C. D.; Sainctavit, P.; Baudelet, F.; Dartyge, E.; Veillet, P.; Verdaguer, M. *J. Am. Chem. Soc.* 1998, 120, 11347. (f) Ferlay, S.; Mallah, T.; Ouahes, R.; Veillet, P.; Verdaguer, M. *Inorg. Chem.* 1999, 38, 229. (g) Verdaguer, M.; Bleuzen, A.; Train, C.; Garde, R.; Fabrizi de Biani, F.; Desplanches, C. Phil. *Trans. R. Soc. Lond. A* 1999, 357, 2959.

(2) Kareis, C. M. (2013). Magnetically Ordered Non-Prussian Blue Structured Manganese(II) Prussian Blue Analogues. Ph. D. Thesis. University of Utah: USA.

(3) (a) Kareis, C. M.; Her, J. H.; Stephens, P. W.; Moore, J. G.; Miller, J. S. . *Chem. Eur. J.*, **2012**, 18, 9281–9288. (b) Her, J.-H., Stephens, P. W., Kareis, C. M., Moore, J. G. and Miller, J. S. *Angew. Chem. Int. Ed.* **2010**, 49: 7773–7775.

(4) Nakamoto, K. *Infrared and Raman Spectra of Inorganic and Coordination Compounds,* 5th ed.; John Wiley and Sons: New York, 1997; Part B, pp. 57-66.

(5) Loopstra, B. O. *Acta. Cryst. B.* **1970**, *656*, B26.

(6) Carlin, R. L. *Magnetochemistry*; Springer-Verlag, 1986. pp 121.

(7) Kittel, C. *Introduction to Solid State Physics*; 5th Ed.; John Wiley and Sons, 1976; pp 479.

(8) Morrish, A. H. *The Principles of Magnetism*, Krieger Publishing Co. 1980, p. 447.

(9) Blundell, S. *Magnetism in Condensed Matter*, Oxford University Press, 2001, p. 92.

(10) Fisher, M. E. *Philos. Mag.* **1962**, *7*, 1731.

(11) Ashcroft, N. W.; Mermin, N. D. *Solid State Physics*, W. B. Saunders and Co., 1976, p. 701.

(12) Aharen, T.; Greedan, J. E.; Ning, F.; Imai, T.; Michaelis, V.; S.; Zhou, H.; Wiebe, C. R.; Cranswick, L. M. D. *Phys. Rev. B.* **2009**, 80, 134423.

(13) Cage, B.; Nguyen, B.; Dalal, N. *Sol. State Commun*, **2001**, 119, 597.

(14) (a) Mydosh, J. A. in *Spin Glasses: An Experimental Introduction*, Taylor and Francis: London, 1993, pg 67. (b) ϕ is a parameter indicative of the amount of spin disorder in a material is known as spin-glass behavior: $\phi = \Delta T_{max}/[T_{max}(\Delta \log \omega)]$, where ΔT_{max} = difference between peak maximum of the temperatures at the high and low frequencies, T_{max} = peak maximum of the temperature at low frequency, $\Delta \log \omega$ = difference in the logarithms of the high and low frequencies(ω).

(15) Brandon et al. *Inorg. Chem.* 37, 13, 3384.

(16) Nelson, K. J.; Giles, I. D.; Troff, S. A.; Arif, A. M.; Miller, J. S. *Inorg. Chem.* **2006**, 45, 8922.

(17) (a) Buschmann, W. E.; Ensling, J.; Gutlich, P.; Miller, J. S.; *Chem. Eur. J.* **1999**, 5, 3019. (b) Sendek, M.; Csach, K.; Kavecansky, V.; Lukacova, M; Marysko, M.; Mitroova, Z.; Zentko, A. *Phys. Stat. Sol. A* **2003**, 196, 225.

CHAPTER 4

CONCLUSIONS AND PROPOSED FUTURE WORK

Since the initial study of Prussian blue (PB) by Keggin and Miles to the present day, many new Prussian blue analogues (PBAs) have been formulated.[1-8] With each new compound, greater understandings and insights into magnetism is gained. As knowledge of the interaction between structure and magnetic properties increases, the ability to reliably and predictably tailor the properties of a compound to a specific set of parameters comes closer to being reality. This thesis presents the synthesis of PBAs under a new set of parameters.

This thesis presents the beginning steps of looking at the effect that nonspherical cations can have on the structure of PBAs. The nonspherical cations used in this project are large enough that the resulting products will all be non-Prussian blue structured PBAs. The reaction of a nonspherical tetraalkylammonium cyanide with $Mn^{II}(OAc)_2$ in water or methanol has resulted in the isolation of seven magnetically pure compounds. The structure of one compound has been determined; the others are still being structurally investigated. When the structures are solved, conclusions will be able to be

drawn more concretely in regards to the effects that nonspherical cations have on the connectivity of the PBAs.

While structural trends cannot be discussed, there are some magnetic trends that are observed in the data presented in this thesis. Two of the three compounds synthesized from the reaction of $[NMe_3Et]CN$ with $Mn^{II}(OAc)_2$ resulted in structures that have antiferromagnetic ground states. The first PBA reported to have an antiferromagnetic ground state was synthesized in a similar manner with $[NMe_4]CN$ and $Mn^{II}(OAc)_2$.[9] One compound synthesized from the $[NMe_3Et]CN$ salt and all of the compounds synthesized from the $[NMe_2Et_2]CN$ and $[NMeEt_3]CN$ salts order as ferrimagnets. It appears that the size of the cation has an effect on the bulk ordering of the compound.

The solvent employed in the reaction appears to have an effect on the ordering temperature, T_c, of the resulting compound. The compound with the highest T_c from each class, $[NMe_3Et]_2Mn_3(CN)_8$ with a T_c of 19.1 K, $[NMe_2Et_2]Mn_3(CN)_7$ with a T_c of 26.1 K, and $[NMeEt_3]_2Mn_2(CN)_6$ with a T_c of 26.3 K, were synthesized in methanol. One notable outlier is the antiferromagnetically ordered compound $[NMe_3Et]_5Mn_9(CN)_{23}$. While this compound was synthesized in methanol, it has the lowest T_c, 13 K, of the compounds synthesized using the $[NMe_3Et]^+$ cation. The compounds synthesized in water had a T_c between 13.8-17 K. It may be the case that synthesis from MeOH allows for more exchange pathways.

The goal of this research was to determine if there was an effect on the structure and as a result, an effect on the magnetic properties of a compound

when synthesized from a nonspherical cation. The structure of $[NMe_3Et]_3Mn_5(CN)_{13}$, as discussed in Chapter 3, is similar to the previously reported $[NMe_4]_3Mn_5(CN)_{13}$.[9] The use of the nonspherical $[NMe_3Et]^+$ cation resulted in a compound that is ordered in three dimensions. In contrast, the $[NMe_4]_3Mn_5(CN)_{13}$ compound lacks order along the z-axis. The nonspherical $[NMe_3Et]^+$ cation resulted in an improved structure. An analysis of the magnetic data shows the following increases of $[NMe_3Et]_3Mn_5(CN)_{13}$ over $[NMe_4]_3Mn_5(CN)_{13}$: 1) a 1.4 emuK/mol increase in the room temperature χT value, 2) a 4.4 K increase in the T_c, and 3) an increase of 1,715 emuOe/mol in the magnetization of the sample at 9 T while being held at 5 K. There is a marked improvement in the structure and magnetic properties when the non-spherical $[NMe_3Et]^+$ cation is used. This is only a singular data point. It has not been determined if the other compounds will be similar to previously reported compounds.[10] When the structures of the other synthesized compounds have been solved, a clearer picture of how nonspherical tetraalkylammonium cations affect the structure and magnetic properties can be established.

Through the course of this research, the ratio of cyanide salt to manganese salt was used as an experimental variable. The effects of solvent and duration of reaction were never fully investigated. It is possible that a study of how concentration and duration affect products could lead to more novel and interesting PBAs. The groundwork for sulfur-based cations was reported in Chapter 2 and the realization and use of the proposed sulfur-based cations could also lead to interesting PBAs. Sulfur-based cations could be made to take up

more total volume without extending the alkyl chains. The use of cations with increased size could yield additional insight into the property tuning process of PBAs.

References

(1) (a) Holmes, S. M.; Girolami, G. S. *J. Am. Chem. Soc.* **1999**, *121*, 5593. (b) Holmes, S. M. Ph.D. Thesis, University of Illinois at Urbana-Champaign, **2000**.

(2) Marvaud, V.; Decroix, C.; Scuiller, A.; Guyard-Duhayon, C.; Vaissermann, J.; Gonnet, F.; Verdaguer, M. *Chem., Eur. J.* **2003**, *9*, 1677.

(3) Juszczyk, S.; Johansson, C.; Hanson, M.; Ratuszna, A.; Malecki, G. *J. Phys.: Condens. Matter* **1994**, *6*, 5697.

(4) Babel, D.; Kurtz, W. in *Solid State Chemistry 1982*, Metselaar, R., Heijligers, H. J. M., Schoonman, J., Eds.; Elsevier, Amsterdam, 1983, p. 593.

(5) Entley, W. R.; Treadway, C. R.; Girolami, G. S. *Mol. Cryst. Liq. Cryst.* **1995**, *273*, 153.

(6) Ferlay, S.; Mallah, T.; Ouahès, R.; Veillet, P.; Verdaguer M. *Nature (London)* **1995**, *378*, 701.

(7) (a) Buschmann, W. E.; Paulson, S. C.; Wynn, C. M.; Girtu, M.; Epstein, A. J.; White, H. S.; Miller, J. S. *Adv. Mater.* **1997**, *9*, 645. (*b)* Buschmann, W. E.; Paulson, S. C.; Wynn, C. M.; Girtu, M.; Epstein, A. J.; White, H. S.; Miller, J. S. *Chem. Mater.* **1998**, *10*, 1386.

(8) Entley, W. R.; Girolami, G. S. *Inorg. Chem.* **1994**, *33*, 5165.

(9) Kareis, C. M. (2013). Magnetically Ordered Non-Prussian Blue Structured Manganese(II) Prussian Blue Analogues. Ph. D. Thesis. University of Utah: USA.

(10) (a) Kareis, C. M.; Her, J. H.; Stephens, P. W.; Moore, J. G.; Miller, J. S. . *Chem. Eur. J.*, **2012**, 18, 9281–9288. (b) Her, J.-H., Stephens, P. W., Kareis, C. M., Moore, J. G. and Miller, J. S. *Angew. Chem. Int. Ed.* **2010**, 49: 7773–7775.